Simulations of Indentation at Continuum and Atomic Levels

Wen Jiang

Dissertation submitted to the faculty of the
Virginia Polytechnic Institute and State University
in partial fulfillment of the requirements for the degree of

Doctor of Philosophy
in
Engineering Mechanics

Prof. Romesh C. Batra, Chair
Prof. Scott W. Case
Prof. Diana Farkas
Prof. Michael W. Hyer
Prof. Liviu Librescu (deceased)
Prof. Tao Lin

January 29, 2008
Blacksburg, VA

Keywords: Cylindrical contact; Nanoindentation; Analytical solution; FCC; Load-displacement relation; Atomic simulation; Continuum equivalence.

Simulations of Indentation at Continuum and Atomic Levels

Wen Jiang

ABSTRACT

The main goal of this work is to determine values of elastic constants of orthotropic, transversely isotropic and cubic materials through indentation tests on thin layers bonded to rigid substrates. Accordingly, we first use the Stroh formalism to provide an analytical solution for generalized plane strain deformations of a linear elastic anisotropic layer bonded to a rigid substrate, and indented by a rigid cylindrical indenter. The mixed boundary-value problem is challenging since the deformed indented surface of the layer contacting the rigid cylinder is unknown a priori, and is to be determined as a part of the solution of the problem. For a rigid parabolic prismatic indenter contacting either an isotropic layer or an orthotropic layer, the computed solution is found to compare well with solutions available in the literature. Parametric studies have been conducted to delimit the length and the thickness of the layer for which the derived relation between the axial load and the indentation depth is valid.

We then derive an expression relating the axial load, the indentation depth, and the elastic constants of an orthotropic material. This relation is specialized to a cubic material (e.g., an FCC single crystal). By using results of three virtual (i.e., numerical) indentation tests on the same specimen oriented differently, we compute values of the elastic moduli, and show that they agree well with their expected values. The technique can be extended to other anisotropic materials.

We review the literature on relations between deformations at the atomic level and stresses and strains defined at the continuum level. These are then used to compare stress and strain distributions in mechanical tests performed on atomic systems and their equivalent continuum structures. Whereas averaged stresses and strains defined in terms of the overall deformations of the atomic system match well with those derived from the continuum description of the body, their local spatial distributions differ.

Dedication

To my grandparents

Acknowledgments

First, I would like to express my acknowledgement to my advisor Dr. Romesh C. Batra for his guidance and advice throughout the course of my doctoral studies. His patience and passion for research are greatly admired. His encouragement and support for this dissertation work are deeply appreciated.

I would also like to thank my committee members for their valuable comments and help on this work and for making time to serve as my committee. I thank all of my professors from whom I have taken classes, and I would like to address special thanks to respectable Dr. Liviu Librescu, who encouraged me a lot at the beginning of my research. In addition, I want to express my gratitude to my colleagues in Dr. Batra's group for their friendships and inspiring ideas.

Lastly, I would like to say thank you to my parents and brother. Without their encouragement and support, I could not have persisted on doing my best in my education.

Contents

List of Figures

List of Tables

Chapter 1

Introduction

Nanoindentation is a popular experimental technique to determine mechanical properties of thin films. In a typical indentation experiment, a pyramidal or spherical diamond indenter is driven into a material while applied load and displacement are continuously monitored. Most models to describe the load-displacement curve assume either the Hertz pressure at the contact surface (Johnson, 1985); or are based on Sneddon's contributions in this area (Sneddon, 1965); e.g. see Oliver and Pharr (1992). Those models adopted Hertz' assumptions such as elliptical contact area, frictionless contact, small contact area compared to the dimensions of contacting bodies so that the indented body can be approximated as a half-space and that deformations occur within the elastic limit. The Oliver-Pharr method, extending from prior research by Sneddon and others (Loubet et al., 1984; Doerner and Nix, 1986), has been successfully applied to thin films.

Nanoindentation tests have also been applied to measure the elastic modulus of polymeric materials (Briscoe and Sebastian, 1996; Briscoe et al., 1996). However, for quasi-static indentation, viscoelastic behavior affects the shape of the unloading curve and the corresponding obtained modulus values are high relative to that obtained from bulk measurements (Lucas et al., 1997). With some experimental adjustment, the nanoindentation technique has also been applied to one-dimensional nanostructures (Zhu et al., 2007), such as multi-walled carbon nanotubes (MWNTs), silicon carbide nanorods (Wong et al., 1997), nanowires (Marszalek et al., 2000) and nanofibers (Tan et al., 2005). The nanoindentation technique has also been applied

in bio-mechanics, bionics and related fields. Measuring the microscopic mechanical properties of bone tissue is important to understand the etiology and pathogenesis of many bone diseases (Hoffler et al., 2005). The intrinsic stiffness of articular cartilage can be estimated by the arthroscopic indentation technique (Toyras et al., 2001). Nanoindentation investigation of dental calcified tissues has improved our understanding of the mechanical behavior of enamel (Habelitz et al., 2001), dentin (Angker et al., 2003) and cementum (Ho et al., 2004) at a nanoscale. Furthermore, in the bionics field, the nanoindentation can help to investigate the special structures and functions of natural biomaterials and biomimetic materials such as the cuticle of a Dung beetle (Sun & Tong, 2005). In many applications, the indented sample cannot be regarded as a linear isotropic half space. For example, the viscoelasticity of polymers, the nonlinearity of some biomaterials, and the thinness of some biomaterials cannot be ignored in the interpretation of load-displacement curves derived from nanoindentation tests. These applications require different continuum models to describe the contact problem.

Atomistic simulations of nanoindentation of various materials have been very popular in recent research and have been very helpful in revealing mechanisms of some interesting phenomena. The jump-to-contact phenomenon has been observed by several groups (Pethica and Oliver, 1989; Landman et al., 1990; Rafii-Tabar et al., 1992), and it describes the 'bulging up' of surface atoms to meet the indenter tip (with higher modulus than that of the indented sample) before the tip makes the actual contact with the surface. Atomistic simulations of this phenomenon give further information on adhesive forces (Landman et al., 1992; Bhushan et al., 1995), which are also responsible for the formation of a connective neck of atoms between the tip and the sample during the retraction of the indenter. Kallman et al. (1993) observed a localized crystalline-to-amorphous transition in silicon (Si) at temperatures close to the melting point, which is consistent with experiments performed by Clarke et al. (1988) and Minowa and Sumino (1992). Their simulations reveal the dependence of the yield strength of Si on atomic structures, rate of deformation and temperature.

Solid-state amorphization has also been observed in nanoindentation simulations of 3C-SiC (Szlufarska et al., 2004). Defect-stimulated growth and coalescence of dislocation loops are found to be the atomistic mechanisms underlying the crystalline-to-amorphous transition. The molecular dynamics (MD) simulations have also been used to study defects generated by nanoindentation. Kelchner et al. (1998) reported that initial partial dislocation loops were nucleated off the indenting axis below the gold (Au) (111) surface. Li et al. (2002) and Van Vliet et al. (2003) performed MD simulations of copper (Cu) (111) and aluminum (Al) (111) nanoindentations for the comprehensive study of dislocation nucleation and kinetics. They verified that homogeneous dislocation nucleation indeed occurs. Furthermore, they obtained the transition from homogeneous dislocation nucleation to source formation and then to prolific heterogeneous dislocation nucleation. Using both energy minimization and constant temperature MD, de la Fuente et al. (2002) demonstrated the formation and movement of hillocks on Au (001) surface under the nanoindenter. Similar investigations on the defect evolution when indenting FCC (001) surface were also presented by Gannepalli and Mallapragada (2002). As for FCC single crystals, defect generation mechanisms in indented crystal surfaces of other lattice structures have been studied, such as Fe single crystal surface by Smith et al. (2003) and Si (001) surface by Gannepalli and Mallapragada (2001). The effects of grain boundary on defect formation when indenting bi- and poly-crystals have been examined through atomistic simulations by Feichtinger et al. (2003) and Lilleodden et al. (2003). Lilleodden et al. (2003) investigated the experimentally observed grain boundary proximity effect, i.e., preferential dislocation emission from the grain boundary occurs during indentation close to that boundary.

Atomistic simulations have mainly supplemented experimentally obtained information until now. Nevertheless, atomistic simulations with higher accuracy, faster speed, and capability of dealing with lager systems are expected (Ghoniem et al., 2003) to provide further insight into the mechanics and the physics of the nanoindentation process. The time scales for MD simulations require about 1m/s

indentation speed while the nanoindenter or atomic force microscope (AFM) can only operate at 0.001 m/s. Limitations in computational resources affect not only the time duration, but also the system's dimensions that can be simulated. Therefore, multiscale techniques are very important for the simulation of real nanoindentation experiments.

Chapter 2

Contact of a smooth rigid indenter with an anisotropic linear elastic layer

2.1 Introduction

Thin films are used in numerous applications such as protective surfaces in artificial joints, underfills in flip chip technology, and coatings on optical equipment and turbine blades. Mechanical properties of thin films and nanosize objects are usually measured with an indentation test, and the value of the elastic modulus in the indentation direction is extracted from the slope of the load versus indentation curve. Such tests are also used to determine elastic moduli of articular cartilage (Toyras et al., 2001) which can provide useful information about the health of the tissue especially when these tests are done in vivo. At the other extreme, similar mechanics issues arise in contact problems of bearings with rubber linings, and in the textile and paper machinery where a steel cylinder contacts another cylinder coated with a layer of rubberlike material. Depending upon dimensions of the indenter, the layer, and the contact zone, the problem may be analyzed as either plane stress, plane strain or as three-dimensional (3D). A 3D problem is usually studied numerically with the finite element method.

In most applications Young's modulus of the indenter material is significantly higher than that of the material of the elastic layer being indented, and the indenter can be regarded as rigid. This is certainly true for the indentation of a soft tissue, and for

rollers used in the paper and textile industries. Furthermore, the deformable layer is bonded to a material that may also be regarded as rigid. When indentation depth is small in comparison to the thickness of the deformable layer, the radius of the indenter, and the width of the layer, the response of the material of the layer may be regarded as linear elastic. Contact problems for even linear elastic materials are challenging because, in general, the shape of the contact area and the pressure distribution on it are unknown a priori. The problem formulation usually involves mixed boundary conditions of normal displacements prescribed on the contact area and surface tractions assigned on the boundary surface close to the indenter but not contacting it. The complexity of the problem increases with an increase in the degree of anisotropy of the material of the indented layer. Analytical solutions of linear problems for isotropic materials with different approximations have been summarized by Johnson (1985). Whereas two elastic moduli characterize a linear elastic isotropic material, the number of elastic moduli for a cubic, a transversely isotropic, and an orthotropic material equal 3, 5 and 9 respectively. Both the analysis of the contact problem and the identification of material moduli from test results become more challenging when the layer material is anisotropic.

Contact problems for transversely isotropic materials have been investigated by Green and Zerna (1954) and Turner (1966). Willis (1966) employed the double Fourier transform technique to analyze the Hertz contact problem for a transversely isotropic half space. Swanson (2004) used Willis's method of double Fourier transforms to reduce governing coupled partial differential equations for the three displacement components to ordinary differential equations which involve derivatives with respect to the coordinate in the indentation direction. Assuming that each displacement component has the same exponential variation in the indentation direction, the problem is reduced to solving a system of three simultaneous algebraic equations. By assuming that edges of the indented layer are simply supported, which is usually not the case for a layer bonded to a rigid substrate, Swanson (2004) found displacement and stress distributions within the layer by using an approach similar to that of Srinivas and Rao

(1970). Swanson (2004) compared the computed solution with that of Turner (1966) for transversely isotropic materials, and also gave solutions for orthotropic materials. Swanson (2004) asserted that the solution technique can not be adopted for general anisotropic materials because Srinivas and Rao's (1970) approach is only applicable to orthotropic materials.

Swadener and Pharr (2000) simplified Willis's (1966) method by using the surface Green function derived earlier by Barnett and Lothe (1975), and studied the indentation of an anisotropic half-space by rigid frictionless parabolic and conical indenters. Fan and Hwu (1996), Hwu and Fan (1998), Ning et al. (2002), and Lin and Ovaert (2004) have combined Stroh's formalism with the analytical continuation (Muskhelishvili, 1954) and the conjugate gradient methods to study indentation of an anisotropic half space by rough indenters of arbitrary profiles. Aboussaleh and Boukhili (1998) have analyzed the contact between a composite laminate and a rigid indenter by assuming that the laminate has a plane of elastic symmetry parallel to its mid-surface and the variation of stresses through the laminate thickness in known. Wu and Yen (1994) employed Green's function to investigate the contact between a simply supported orthotropic plate and a rigid sphere. Based on experimental results, Yang and Sun (1982) and Tan and Sun (1985) modified the Hertzian contact law for an orthotropic layer by assuming that the pressure distribution on the contact surface and the width of the contact area for an anisotropic layer can be derived from those for an isotropic layer by replacing Young's modulus by the elastic modulus of the anisotropic layer in the indentation direction. It seems that the indentation of an anisotropic layer of finite width and thickness has not been studied analytically.

Here we adopt Stroh's formalism (1958, 1962) to study infinitesimal deformations of an anisotropic layer of finite width and thickness bonded to a rigid substrate and indented by an indenter of arbitrary profile with the goal of deriving a relation between the axial load and the indentation depth. The analytical function in Stroh's formalism is expressed as Fourier sine and cosine series with their coefficients

decaying exponentially in the thickness direction; e.g. see Vel and Batra (2000) who used this technique to analyze deformations of an anisotropic plate under different boundary conditions. The unknown constants in the Fourier series are determined by satisfying boundary conditions in an average sense. The convergence of the series solution is established by numerically solving two contact problems; one for an isotropic and the other for an orthotropic layer and comparing their solutions with results available in the literature. Subsequently, parametric studies are performed to delineate the effect of various material and geometric parameters upon the load required to indent an orthotropic layer by a prescribed amount. Lastly, the indentation of a layer by a flat indenter is studied.

2.2 Problem formulation

The problem studied, shown schematically in Figure 2.1, involves a linear elastic, homogeneous and anisotropic layer bonded to a rigid substrate and indented by a rigid circular cylinder. It is assumed that the length of the cylinder and of the layer in the x_2 - direction (perpendicular to the plane of the paper) is very large as compared to dimensions of the layer within the plane of the paper (i.e., the length *L,* and the thickness *h* of the layer). Also, the radius *R* of the cylinder is much smaller than the length *L* of the layer, and the applied axial load *P* is such as to induce infinitesimal deformations of the layer. As the cylinder is pressed statically into the linear elastic layer, points of the layer underneath the cylinder move vertically down, those not on the axis of the cylinder also move axially outwards while those near the free surface of the layer and adjacent to the rigid cylinder move upwards. We denote indentation of the cylinder into the layer by u_0, and the semi-contact width by *c;* u_0 and *c* are depicted in Figure 2.1.

We use rectangular Cartesian coordinates to describe infinitesimal deformations of the layer, and assume that the displacement field **u** and hence stresses and strains

induced in the layer are functions of x_1 and x_3 only. Thus the state of deformation of the layer corresponds to that of generalized plane strain. In the absence of body forces, equations governing deformations of the layer are

$$\sigma_{ij,j} = 0, \qquad i = 1,2,3, \tag{2.1}$$

$$\sigma_{ij} = C_{ijkl} e_{kl}, \qquad C_{ijkl} = C_{jikl} = C_{klij}, \tag{2.2}$$

$$e_{kl} = \frac{1}{2}\left(u_{k,l} + u_{l,k}\right), \tag{2.3}$$

where $\sigma_{ij} = \sigma_{ji}$ is the Cauchy stress tensor, $\sigma_{ij,j} = \partial \sigma_{ij} / \partial x_j$, a repeated index implies summation over the range of the index, e_{kl} is the infinitesimal strain tensor, u_i is the displacement of a point in the x_i-direction, and C_{ijkl} is an elastic constant of the material of the linear elastic layer. Symmetries indicated in Eq. (2.2) imply that, for a three-dimensional problem, C_{ijkl} can be written as a symmetric 6×6 matrix, and σ_{ij} and e_{kl} as 6×1 matrices. Henceforth, we assume that C_{ijkl} is positive-definite which is equivalent to presuming that the strain energy density is positive for every non-rigid deformation of the body.

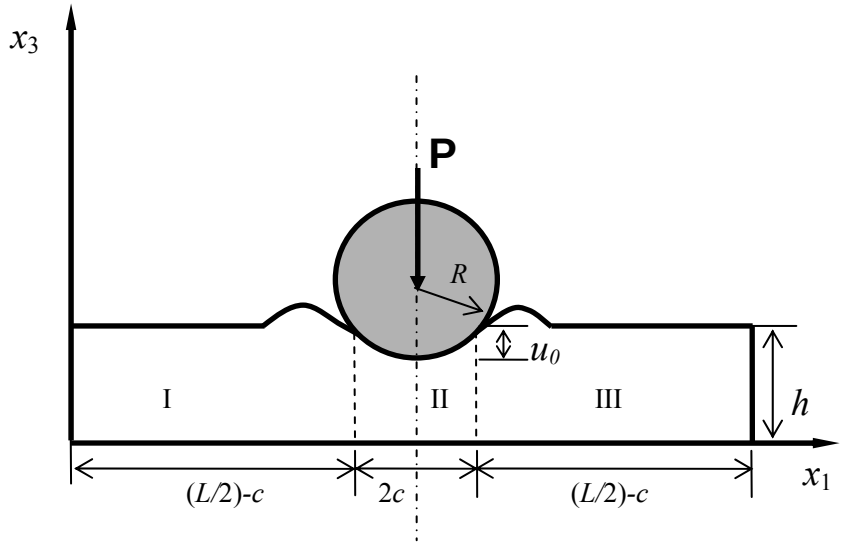

Figure 2.1 Schematic sketch of the problem studied

Substitution from Eq. (2.3) into Eq. (2.2), and the result into Eq. (2.1) yields the following second-order coupled partial differential equations for u_1, u_2 and u_3:

$$C_{ijkl} u_{l,kj} = 0, \qquad i = 1,2,3. \tag{2.4}$$

Pertinent boundary conditions are:

$$\sigma_{11} = \sigma_{31} = 0 \qquad \text{on} \quad x_1 = 0, L\,, \tag{2.5.1}$$

$$u_1 = u_3 = 0 \qquad \text{on} \quad x_3 = 0\,, \tag{2.5.2}$$

$$\sigma_{13} = \sigma_{33} = 0 \qquad \text{on} \quad x_3 = h \quad \text{and} \quad |x_1 - L/2| > c\,, \tag{2.5.3}$$

$$\big(\mu \sin^2\theta + \sin\theta\cos\theta\big)\sigma_{11} - \big(\mu \sin 2\theta + \cos 2\theta\big)\sigma_{31} + \big(\mu\cos^2\theta - \sin\theta\cos\theta\big)\sigma_{33} = 0\,,$$

$$u_3 = g(x_1) \quad \text{on} \quad x_3 = h \quad \text{and} \quad |x_1 - L/2| \le c\,. \tag{2.5.4}$$

Here $\theta = \arcsin((x_1 - L/2)/R)$, μ is the coefficient of friction between the rigid indenter and the deformable layer, c the semi-contact width, and the function $g(x_1)$ depends upon the shape of the indenter. In cylindrical coordinates, the left-hand side of Eq. (2.5.4) equals $(\sigma_{r\theta} - \mu\sigma_{rr})$, where $\sigma_{r\theta}$ and σ_{rr} are, respectively, tangential and the normal tractions at a point on the contact surface. When the contact surface between the indenter and the deformable layer can be regarded as smooth, $\mu = 0$. Points of the contact surface where $\sigma_{rr} \ge 0$ do not contact the indenter. We assume that there is no separation between the indenter and the deformable layer; thus the contact surface is contiguous. For a rigid circular cylinder of radius *R*,

$$g(x_1) = R - u_0 - \sqrt{R^2 - (x_1 - L/2)^2}\,, \tag{2.6}$$

where u_0 is the indentation (e.g. see Figure 2.1). In a 3D problem, boundary conditions on end faces parallel to the x_1x_3 - plane also need to be specified.

We study infinitesimal deformations of the layer, hence $c/R << 1$. Disregarding the curvature of the cylinder, we write the axial load *P* per unit length of the cylinder as

$$P = -\int_{L/2-c}^{L/2+c} \sigma_{33}\, dx_3\,. \tag{2.7.1}$$

If the curvature of cylinder is considered,

$$P = -\int_{L/2-c}^{L/2+c} \big(\sigma_{33} - \sigma_{13}\tan\theta\big)\, dx_3 \tag{2.7.2}$$

Out of three variables *P*, *c* and u_0 characterizing the indentation of the cylinder into the layer, only one can be specified, and the other two are determined as a part of the solution of the problem. Here we prescribe *c* and find corresponding values of *P* and u_0.

2.3 Analytical solution of the problem

Following Fan and Hwu (1996), Hwu and Fan (1998), and Vel and Batra (2000) we use the Eshelby-Stroh formalism to find a general solution of the above formulated boundary-value problem. Accordingly, we divide the deformable layer into three regions I, II and III as exhibited in Figure 2.1. The region I extends from the left edge $x_1 = 0$ of the layer to the vertical surface $x_1 = (L/2) - c$ that passes through the left-most contact point, the region II of width $2c$ is directly under the contact surface, and region III extends from $x_1 = (L/2) + c$ to the right edge $x_1 = L$ of the layer. We require that displacements and surface tractions be continuous across the interface between regions I and II, and the interface between regions II and III. That is

$$u_i((L/2-c)^-, x_3) - u_i((L/2-c)^+, x_3) = 0, \qquad i = 1,2,3, \tag{2.8.1}$$

$$u_i((L/2+c)^-, x_3) - u_i((L/2+c)^+, x_3) = 0, \qquad i = 1,2,3, \tag{2.8.2}$$

$$\sigma_{i1}((L/2-c)^-, x_3) - \sigma_{i1}((L/2-c)^+, x_3) = 0, \quad i = 1,2,3, \tag{2.8.3}$$

$$\sigma_{i1}((L/2+c)^-, x_3) - \sigma_{i1}((L/2+c)^+, x_3) = 0, \quad i = 1,2,3. \tag{2.8.4}$$

While finding a general solution of the governing equations, we assume that

$$u_i = a_i f(z), \qquad z = x_1 + p x_3, \qquad i = 1,2,3, \tag{2.9}$$

where f is an arbitrary analytic function of z, and a_1, a_2, a_3 and p are complex constants to be determined. Substitution for u_i from Eq. (2.9) into Eq. (2.4) yields

$$\left[C_{i11l} + p\left(C_{i13l} + C_{i31l}\right) + p^2 C_{i33l}\right] a_l = 0, \tag{2.10}$$

where we have assumed that $f''(z) = d^2 f / dz^2 \neq 0$. We define 3×3 matrices $\mathbf{Q}$, $\mathbf{R}$ and $\mathbf{T}$ as follows:

$$Q_{il} = C_{i11l}, \quad R_{il} = C_{i13l}, \quad T_{il} = C_{i33l}. \tag{2.11}$$

Using symmetries of the elasticity matrix C_{ijkl} indicated in Eq. (2.2), we write the eigen-value problem defined by Eq. (2.10) in direct notation as

$$\left[\mathbf{Q} + p(\mathbf{R} + \mathbf{R}^{\mathrm{T}}) + p^2 \mathbf{T}\right]\mathbf{a} = \mathbf{0}. \tag{2.12}$$

The positive-definiteness of $\mathbf{C}$ implies that $\mathbf{Q}$ and $\mathbf{T}$ are positive-definite matrices. With the definition

$$\mathbf{b} = -\frac{1}{p}\left(\mathbf{Q} + p\mathbf{R}\right)\mathbf{a} = \left(\mathbf{R}^{\mathrm{T}} + p\mathbf{T}\right)\mathbf{a}, \tag{2.13}$$

the eigen-value problem defined by Eq. (2.12) can be written as

$$\mathbf{N}\boldsymbol{\zeta} = p\boldsymbol{\zeta}, \tag{2.14}$$

where

$$\mathbf{N} = \begin{bmatrix} -\mathbf{T}^{-1}\mathbf{R}^{\mathrm{T}} & \mathbf{T}^{-1} \\ \mathbf{R}\mathbf{T}^{-1}\mathbf{R}^{\mathrm{T}} - \mathbf{Q} & -\mathbf{R}\mathbf{T}^{-1} \end{bmatrix}, \qquad \boldsymbol{\zeta} = \begin{Bmatrix} \mathbf{a} \\ \mathbf{b} \end{Bmatrix}, \tag{2.15}$$

p is the eigen-value, and ζ the eigen-vector. For the strain energy density to be positive definite, p must be complex (Eshelby et al., 1953). Let (p_α, a_α), $\alpha = 1,2,...,6$ be eigen-solutions of Eq. (2.12) such that

$$\mathrm{Im}(p_\alpha) > 0\,,\ p_{\alpha+3} = \overline{p}_\alpha\,,\ \ a_{\alpha+3} = \overline{a}_\alpha\,,\quad \alpha = 1,2,3\,, \tag{2.16}$$

where $\overline{p}_\alpha$ is the complex conjugate of p_α. Assuming that all p's are distinct, a general solution of Eqs. (2.1) - (2.3) can be written as

$$\mathbf{u} = \sum_{\alpha=1}^{3}\left[\mathbf{a}_\alpha f_\alpha(z_\alpha) + \overline{\mathbf{a}}_\alpha f_{\alpha+3}(\overline{z}_\alpha)\right], \tag{2.17}$$

where f_α ($\alpha = 1,2,...,6$) are arbitrary analytic functions of z_α. The general solution (2.17) holds even when the six eigen-values are not distinct but there exist six linearly independent eigenvectors. Ting (1996) has discussed how to modify the general solution when the eigen-value problem defined by Eq. (2.12) does not have six linearly independent eigenvectors.

Substitution for $\mathbf{u}$ from Eq. (2.17) into Eq. (2.3) and the result into Eq. (2.2) gives

$$\boldsymbol{\sigma}_1 = -\sum_{\alpha=1}^{3}\left[p_\alpha \mathbf{b}_\alpha f'_\alpha(z_\alpha) + \overline{p}_\alpha \overline{\mathbf{b}}_\alpha f'_{\alpha+3}(\overline{z}_\alpha)\right], \tag{2.18}$$

$$\boldsymbol{\sigma}_3 = -\sum_{\alpha=1}^{3}\left[\mathbf{b}_\alpha f'_\alpha(z_\alpha) + \overline{\mathbf{b}}_\alpha f'_{\alpha+3}(\overline{z}_\alpha)\right], \tag{2.19}$$

where

$$(\boldsymbol{\sigma}_1)_i = \sigma_{i1}\,, \qquad (\boldsymbol{\sigma}_3)_i = \sigma_{i3}\,. \tag{2.20}$$

We note that $\boldsymbol{\sigma}$ given by Eq. (2.18) satisfies the equilibrium Eq. (2.1) for all choices of the analytic function $f_\alpha(z)$. In order to satisfy boundary conditions (2.5) and continuity conditions (2.8) we assume the following series solution for the n^{th} ($\mathrm{n} = 1,2,3$) region.

$$f_\alpha^{(n)}(z_\alpha^{(n)}) = d_\alpha^{(n)} + z_\alpha^{(n)} v_\alpha^{(n)} + \left(z_\alpha^{(n)}\right)^2 w_\alpha^{(n)} + \sum_{k=1}^{\infty}\left\{q_{k\alpha}^{(n)} \exp(\lambda_{k\alpha}^{(n)} z_\alpha^{(n)}) + r_{k\alpha}^{(n)} \exp(\lambda_{k\alpha}^{(n)}(p_\alpha^{(n)} h - z_\alpha^{(n)}))\right\}$$

$$+ \sum_{m=1}^{\infty}\left\{s_{m\alpha}^{(n)} \exp(\eta_{m\alpha}^{(n)} z_\alpha^{(n)}) + t_{m\alpha}^{(n)} \exp(\eta_{m\alpha}^{(n)}(l^{(n)} - z_\alpha^{(n)}))\right\}, \quad 0 \le x_1^{(n)} \le l^{(n)}, \tag{2.21}$$

where

$$z_\alpha^{(n)} = x_1^{(n)} + p_\alpha^{(n)} x_3^{(n)}, \quad \lambda_{k\alpha}^{(n)} = \frac{k\pi i}{l^{(n)}}, \quad \eta_{m\alpha}^{(n)} = -\frac{m\pi i}{p_\alpha^{(n)} h}, \quad i = \sqrt{-1}. \tag{2.22}$$

The unknowns $d_\alpha^{(n)}$ and $w_\alpha^{(n)}$ are assumed to be real while $v_\alpha^{(n)}, q_{k\alpha}^{(n)}, r_{k\alpha}^{(n)}, s_{m\alpha}^{(n)}$ and $t_{m\alpha}^{(n)}$ are complex; these will be determined from the boundary conditions, and the continuity conditions at the interfaces. In Eqs. (2.21) and (2.22), $l^{(n)}$ (n = 1, 2, 3) is the width of the n^{th} segment. Note that each term in series (2.21) is an analytical function of $z_\alpha^{(n)}$. The choice (2.21) for $f_\alpha(z)$ is dictated by shapes of segments.

Substituting for $f_\alpha(z_\alpha)$ from Eq. (2.21) into Eqs. (2.17)-(2.19), we get the following for the displacements $\mathbf{u}^{(n)}$ and stresses $\boldsymbol{\sigma}_1^{(n)}$ and $\boldsymbol{\sigma}_3^{(n)}$ in the n^{th} segment:

$$\mathbf{u}^{(n)} = \mathbf{A}\left\{\mathbf{d}^{(n)} + \left\langle z_*^{(n)}\right\rangle \mathbf{v}^{(n)} + \left\langle \left(z_*^{(n)}\right)^2\right\rangle \mathbf{w}^{(n)} + \sum_{k=1}^{\infty}\left[\left\langle\!\left\langle \exp\left(\beta_{k*}^{(n)}\right)\right\rangle\!\right\rangle \mathbf{q}_k^{(n)} + \left\langle\!\left\langle \exp\left(\gamma_{k*}^{(n)}\right)\right\rangle\!\right\rangle \mathbf{r}_k^{(n)}\right]\right.$$

$$\left. + \sum_{m=1}^{\infty}\left[\left\langle\!\left\langle \exp\left(\delta_{m*}^{(n)}\right)\right\rangle\!\right\rangle \mathbf{s}_m^{(n)} + \left\langle\!\left\langle \exp\left(\xi_{m*}^{(n)}\right)\right\rangle\!\right\rangle \mathbf{t}_k^{(n)}\right]\right\} + \text{conjugate}, \tag{2.23}$$

$$\boldsymbol{\sigma}_1^{(n)} = \mathbf{B}\left\{-\left\langle p_*^{(n)}\right\rangle \mathbf{v}^{(n)} - \left\langle 2p_*^{(n)} z_*^{(n)}\right\rangle \mathbf{w}^{(n)} + \sum_{k=1}^{\infty}\left[-\left\langle\!\left\langle \lambda_{k*}^{(n)} p_*^{(n)} \exp\left(\beta_{k*}^{(n)}\right)\right\rangle\!\right\rangle \mathbf{q}_k^{(n)} + \left\langle\!\left\langle \lambda_{k*}^{(n)} p_*^{(n)} \exp\left(\gamma_{k*}^{(n)}\right)\right\rangle\!\right\rangle \mathbf{r}_k^{(n)}\right]\right.$$

$$\left. + \sum_{m=1}^{\infty}\left[-\left\langle\!\left\langle \eta_{m*}^{(n)} p_*^{(n)} \exp\left(\delta_{m*}^{(n)}\right)\right\rangle\!\right\rangle \mathbf{s}_m^{(n)} + \left\langle\!\left\langle \eta_{m*}^{(n)} p_*^{(n)} \exp\left(\xi_{m*}^{(n)}\right)\right\rangle\!\right\rangle \mathbf{t}_k^{(n)}\right]\right\} + \text{conjugate}, \tag{2.24}$$

$$\boldsymbol{\sigma}_3^{(n)} = \mathbf{B}\left\{\mathbf{v}^{(n)} + \left\langle 2z_*^{(n)}\right\rangle \mathbf{w}^{(n)} + \sum_{k=1}^{\infty}\left[\left\langle\!\left\langle \lambda_{k*}^{(n)} \exp\left(\beta_{k*}^{(n)}\right)\right\rangle\!\right\rangle \mathbf{q}_k^{(n)} - \left\langle\!\left\langle \lambda_{k*}^{(n)} \exp\left(\gamma_{k*}^{(n)}\right)\right\rangle\!\right\rangle \mathbf{r}_k^{(n)}\right]\right.$$

$$\left. + \sum_{m=1}^{\infty}\left[\left\langle\!\left\langle \eta_{m*}^{(n)} \exp\left(\delta_{m*}^{(n)}\right)\right\rangle\!\right\rangle \mathbf{s}_m^{(n)} - \left\langle\!\left\langle \eta_{m*}^{(n)} \exp\left(\xi_{m*}^{(n)}\right)\right\rangle\!\right\rangle \mathbf{t}_k^{(n)}\right]\right\} + \text{conjugate}, \tag{2.25}$$

where

$$\mathbf{A} = [\mathbf{a}_1\ \mathbf{a}_2\ \mathbf{a}_3], \quad \mathbf{B} = [\mathbf{b}_1\ \mathbf{b}_2\ \mathbf{b}_3],$$

$$\beta_{k\alpha}^{(n)} = \lambda_{k\alpha}^{(n)} z_\alpha^{(n)}, \quad \gamma_{k\alpha}^{(n)} = \lambda_{k\alpha}^{(n)} \left(p_\alpha^{(n)} h - z_\alpha^{(n)} \right),$$

$$\delta_{m\alpha}^{(n)} = \eta_{m\alpha}^{(n)} z_\alpha^{(n)}, \quad \xi_{m\alpha}^{(n)} = \eta_{m\alpha}^{(n)} \left(l^{(n)} - z_\alpha^{(n)} \right),$$

$$\left\langle \phi_* \psi_* \chi_* \right\rangle = \mathrm{diag}\left[\phi_1 \psi_1 \chi_1, \phi_2 \psi_2 \chi_2, \phi_3 \psi_3 \chi_3 \right],$$

$$\left(\mathbf{d}^{(n)} \right)_\alpha = d_\alpha^{(n)}, \ \alpha = 1, 2, 3. \tag{2.26}$$

The unknowns $\mathbf{d}^{(n)}$ and $\mathbf{w}^{(n)}$ are assumed to be real while $\mathbf{v}^{(n)}$, $\mathbf{q}_k^{(n)}$, $\mathbf{r}_k^{(n)}$, $\mathbf{s}_m^{(n)}$, $\mathbf{t}_m^{(n)}$ are complex and defined in a way similar to $\mathbf{d}^{(n)}$, and conjugate stands for the complex conjugate of the explicitly stated terms.

In terms of the 3×3 diagonal matrices $\mathbf{I}_u^l, \mathbf{I}_\sigma^l, \mathbf{I}_u^r, \mathbf{I}_\sigma^r, \mathbf{I}_u^t, \mathbf{I}_\sigma^t, \mathbf{I}_u^b, \mathbf{I}_\sigma^b$ whose elements are constants, and

$$\mathbf{I}_u^l + \mathbf{I}_\sigma^l = \mathbf{I}_u^r + \mathbf{I}_\sigma^r = \mathbf{I}_u^t + \mathbf{I}_\sigma^t = \mathbf{I}_u^b + \mathbf{I}_\sigma^b = \mathbf{I}, \tag{2.27}$$

where $\mathbf{I}$ is the 3×3 identity matrix, boundary conditions (2.5) with $\mu = 0$ can be written as

$$\mathbf{I}_u^l \mathbf{u} + \mathbf{I}_\sigma^l \boldsymbol{\sigma}_1 = \mathbf{0} \qquad \text{on} \quad x_1 = 0, \tag{2.28.1}$$

$$\mathbf{I}_u^r \mathbf{u} + \mathbf{I}_\sigma^r \boldsymbol{\sigma}_1 = \mathbf{0} \qquad \text{on} \quad x_1 = L, \tag{2.28.2}$$

$$\mathbf{I}_u^b \mathbf{u} + \mathbf{I}_\sigma^b \boldsymbol{\sigma}_3 = \mathbf{0} \qquad \text{on} \quad x_3 = 0, \tag{2.28.3}$$

$$\mathbf{I}_u^t \mathbf{u} + \mathbf{I}_\sigma^t \boldsymbol{\sigma}_3 = \mathbf{0} \qquad \text{on} \quad x_3 = h, \quad |x_1 - L/2| > c, \tag{2.28.4}$$

$$\mathbf{I}_u^t \mathbf{u} + \mathbf{I}_\sigma^t \boldsymbol{\sigma}_3' = \begin{bmatrix} 0 & 0 & g(x_1) \end{bmatrix}^{\mathrm{T}} \quad \text{on} \quad x_3 = h, |x_1 - L/2| \le c, \tag{2.28.5}$$

where $\left(\boldsymbol{\sigma}_3' \right)_1 = \left(\mu \sin^2\theta + \sin\theta\cos\theta \right)\sigma_{11} + \left(\mu\cos^2\theta - \sin\theta\cos\theta \right)\sigma_{33} - \left(\mu \sin 2\theta + \cos 2\theta \right)\sigma_{31}$. Instead of satisfying point-wise boundary conditions (2.28) and continuity conditions (2.8), we enforce them in an average sense as detailed below:

$$\int_{-l^{(n)}}^{l^{(n)}} \left\{ \mathbf{I}_u^{nt} \mathbf{u}^{(n)}(x_1^{(n)}, h) + \mathbf{I}_\sigma^{nt} \boldsymbol{\sigma}_3^{(n)}(x_1^{(n)}, h) - \mathbf{g}^{nt}(x_1^{(n)}) \right\} \exp\left(j \frac{i\pi x_1^{(n)}}{l^{(n)}} \right) dx_1^{(n)} = \mathbf{0}, \tag{2.29.1}$$

$$\int_{-l^{(n)}}^{l^{(n)}} \left\{ \mathbf{I}_u^{nb} \mathbf{u}^{(n)}(x_1^{(n)}, 0) + \mathbf{I}_\sigma^{nb} \boldsymbol{\sigma}_3^{(n)}(x_1^{(n)}, 0) - \mathbf{g}^{nb}(x_1^{(n)}) \right\} \exp\left(j \frac{i\pi x_1^{(n)}}{l^{(n)}} \right) dx_1^{(n)} = \mathbf{0},$$

$$j = 0,1,2\ldots; \ n = 1, 2, 3, \tag{2.29.2}$$

$$\int_{-h}^{h} \left\{ \mathbf{I}_u^l \mathbf{u}^{(1)}(0, x_3) + \mathbf{I}_\sigma^l \boldsymbol{\sigma}_1^{(1)}(0, x_3) - \mathbf{g}^l(x_3) \right\} \exp\left(j \frac{i\pi x_3}{h} \right) dx_3 = \mathbf{0}, \tag{2.29.3}$$

$$\int_{-h}^{h}\left\{\mathbf{I}_u^r\mathbf{u}^{(3)}(0,x_3)+\mathbf{I}_\sigma^r\boldsymbol{\sigma}_1^{(3)}(0,x_3)-\mathbf{g}^r(x_3)\right\}\exp\left(j\frac{i\pi x_3}{h}\right)dx_3=\mathbf{0},\quad j=0,\,1,\,2\ldots;\ (2.29.4)$$

$$\int_{-h}^{h}\left\{\mathbf{u}^{(n)}(l^{(n)},x_3)-\mathbf{u}^{(n+1)}(0,x_3)\right\}\exp\left(j\frac{i\pi x_3}{h}\right)dx_3=\mathbf{0},\qquad (2.30.1)$$

$$\int_{-h}^{h}\left\{\boldsymbol{\sigma}_1^{(n)}(l^{(n)},x_3)-\boldsymbol{\sigma}_1^{(n+1)}(0,x_3)\right\}\exp\left(j\frac{i\pi x_3}{h}\right)dx_3=\mathbf{0},\quad j=0,\,1,\,2\ldots;\ n=1,\,2.\quad (2.30.2)$$

Here $l^{(1)}=l^{(3)}=(L/2)-c$, $l^{(2)}=2c$; $\mathbf{I}_u^{1t}=\mathbf{I}_u^{3t}=\mathrm{diag}[0,1,0]$, $\mathbf{I}_\sigma^{1t}=\mathbf{I}_\sigma^{3t}=\mathrm{diag}[1,0,1]$, $\mathbf{I}_u^{2t}=\mathrm{diag}[0,1,1]$, $\mathbf{I}_\sigma^{2t}=\mathrm{diag}[1,0,0]$; $\mathbf{I}_u^{l}=\mathbf{I}_u^{r}=\mathrm{diag}[0,1,0]$, $\mathbf{I}_\sigma^{l}=\mathbf{I}_\sigma^{r}=\mathrm{diag}[1,0,1]$; $\mathbf{I}_\sigma^{1b}=\mathbf{I}_\sigma^{2b}=\mathbf{I}_\sigma^{3b}=\mathrm{diag}[0,0,0]$, $\mathbf{I}_u^{1b}=\mathbf{I}_u^{2b}=\mathbf{I}_u^{3b}=\mathrm{diag}[1,1,1]$; $\mathbf{g}^{2t}(x_1^{(n)})=\mathrm{diag}[0,\,0,\,g(x_1)]$, $\mathbf{g}^{1t}(x_1^{(n)})=\mathbf{g}^{3t}(x_1^{(n)})=\mathbf{g}^{1b}(x_1^{(n)})=\mathbf{g}^{2b}(x_1^{(n)})=\mathbf{g}^{3b}(x_1^{(n)})=\mathbf{g}^{l}(x_3)=\mathbf{g}^{r}(x_3)=\mathrm{diag}\ [0,\,0,\,0]$.

Eq. (2.29.1) can be directly applied to the indentation problem for a flat punch. However, in order to avoid the appearance of the unknown indentation depth u_0 in boundary conditions for cylindrical or parabolic indenters, we differentiate both sides of Eq. $(2.5.4)_2$ with respect to x_1, and use

$$u_3'^{(2)}(x_1,h)=g'(x_1)\qquad (2.31)$$

as the boundary condition in region II where a prime indicates differentiation with respect to x_1. Thus in segment II, we enforce

$$\int_{-l^{(2)}}^{l^{(2)}}\left\{\mathbf{I}_{u'}^{2t}\mathbf{u}'^{(2)}(x_1^{(2)},h)+\mathbf{I}_\sigma^{2t}\boldsymbol{\sigma}_3^{(2)}(x_1^{(2)},h)-\mathbf{g}'^{2t}(x_1^{(2)})\right\}\exp\left(j\frac{i\pi x_1^{(2)}}{l^{(2)}}\right)dx_1^{(2)}=\mathbf{0}\qquad (2.29.1^*)$$

where $\mathbf{I}_{u'}^{2t}=\mathrm{diag}[0,0,1]$ and $\mathbf{g}'^{2t}(x_1^{(2)})=\mathrm{diag}[0,\,0,\,g'(x_1)]$. Once the problem has been solved, the indentation u_0 can be found from Eq. (2.29.1).

By substituting from Eq. (2.25) into Eqs. (2.29) and (2.30), we determine the unknown parameters $\mathbf{d}^{(n)}$, $\mathbf{v}^{(n)}$, $\mathbf{w}^{(n)}$, $\mathbf{q}_k^{(n)}$, $\mathbf{r}_k^{(n)}$, $\mathbf{s}_m^{(n)}$ and $\mathbf{t}_m^{(n)}$ (n = 1, 2, 3; k = 0,1,2…; m = 0,1,2…). The polynomial and the exponential functions corresponding to each unknown parameter, and the prescribed function $g'(x_1)$ are extended as even functions over the interval $(-l^{(n)},0)$. By truncating m to M in Eqs. (2.29) and (2.30), and equating the real and the imaginary parts on both sides of those equations,

we obtain the number of real equations equal to the number of real unknowns. To maintain approximately the same period of the largest harmonic on all interfaces and boundaries, we truncate k to $K^{(n)}$ for the n^{th} segment with

$$K^{(n)} = \text{Ceil}\left(M \frac{l^{(n)}}{h} \right) \tag{2.32}$$

where Ceil(*) gives the smallest integer greater than or equal to *.

Based on the above-stated algorithm, we have developed a computer code in MATLAB. As described in the following section, the code is verified by comparing computed results for two problems with those available in the literature.

2.4 Verification of the Computer Code

We determine the number of terms to be retained in the series solution (cf. Eq. (2.23)) and verify our algorithm as follows. We first obtain a converged solution for a layer made of an orthotropic material with principal material axes coincident with the rectangular Cartesian coordinate axes exhibited in Figure 2.1, and compare presently computed results with those available in the literature. Subsequently, we verify the code for an isotropic layer.

2.4.1 Indentation of an orthotropic half space by a smooth rigid parabolic indenter

We compare our results with the analytical solution of Hwu and Fan (1998) for the indentation of an orthotropic half-space by the smooth rigid parabolic indenter, $x_3 = \dfrac{(x_1 - L/2)^2}{2R}$ where R is the radius of curvature of the indenter at the point ($L/2$, 0).

For plane strain deformations in the x_1x_3-plane, Hooke's law for an orthotropic

material can be written as

$$\begin{Bmatrix}\sigma_{11}\\ \sigma_{33}\\ \sigma_{13}\end{Bmatrix}=\begin{bmatrix}C_{11} & C_{13} & 0\\ C_{13} & C_{33} & 0\\ 0 & 0 & C_{55}\end{bmatrix}\begin{Bmatrix}e_{11}\\ e_{33}\\ 2e_{13}\end{Bmatrix}, \tag{2.33}$$

where

$$C_{11}=\frac{1-\nu_{23}\nu_{32}}{\Delta}E_1,\quad C_{33}=\frac{1-\nu_{12}\nu_{21}}{\Delta}E_3,$$
$$C_{13}=\frac{\nu_{31}+\nu_{21}\nu_{32}}{\Delta}E_1=\frac{\nu_{13}+\nu_{12}\nu_{23}}{\Delta}E_3,\quad C_{55}=G_{31},$$
$$\Delta=1-\nu_{12}\nu_{21}-\nu_{23}\nu_{32}-\nu_{31}\nu_{13}-2\nu_{21}\nu_{32}\nu_{13}. \tag{2.34}$$

Here E_i is Young's modulus in the x_i- direction, G_{31} is the shear modulus in the x_3x_1- plane, and

$$\nu_{ij}=-\frac{\text{normal strain in the } x_j\text{- direction}}{\text{normal strain in the } x_i\text{- direction}} \tag{2.35}$$

for a uniaxial stress applied along the x_i-direction. According to Hwu and Fan (1998), the normal stress, σ_{33}, between the indenter and the half space with the material principal axes coincident with the rectangular Cartesian coordinate axes is given by

$$\sigma_{33}=-\frac{1}{\beta R}\sqrt{c^2-(x_1-L/2)^2},\quad |x_1-L/2|<c, \tag{2.36}$$

where

$$\frac{1}{\beta}=\alpha_2\kappa_2E_3, \tag{2.37.1}$$

$$\alpha_2=(1-\nu_{23}\nu_{32})^{-1/2}, \tag{2.37.2}$$

$$\kappa_2=\left(E_3/G_{31}+2\eta_1\sqrt{E_3/E_1}\right)^{-1/2}, \tag{2.37.3}$$

$$\eta_1=\sqrt{(1-\nu_{12}\nu_{21})(1-\nu_{23}\nu_{32})}-\sqrt{(\nu_{31}+\nu_{21}\nu_{32})(\nu_{13}+\nu_{23}\nu_{12})}. \tag{2.37.4}$$

In order to compute numerical results we assign following values to various material

and geometric parameters.

$$E_1 = 25.0\,\text{GPa},\quad E_2 = E_3 = 1.0\,\text{GPa},\quad G_{23} = 0.2\,\text{GPa},$$
$$G_{12} = G_{31} = 0.5\,\text{GPa},\quad \nu_{12} = \nu_{23} = \nu_{13} = 0.25,$$
$$L = 1.0\ \text{m},\quad h = 0.4\,\text{m},\quad R = 0.5\,\text{m}, 2c = 0.1\,\text{m}. \tag{2.38}$$

Then $\nu_{21} = \nu_{31} = 0.01$ and $\nu_{32} = 0.25$ can be calculated from values of parameters listed in Eq. (2.38) and the following relations: $E_i/\nu_{ij} = E_j/\nu_{ji}$ (no sum on i and j). Since $2c/L = 0.1$, it is reasonable to assume that null tractions applied on the left and the right vertical surfaces do not influence the solution in the vicinity of the contact region. The computed value of u_0 was found to be less than $0.1h$ signifying thereby the applicability of the analytical solution for the half space to the present problem. We have compared in Figure 2.2 pressure distribution on the contact surface given by the analytical solution of Hwu and Fan (1998) with that computed from the present code by setting K = 500 in the series solution represented by Eqs. (2.23) – (2.25). It is clear that the two pressure distributions agree well with each other, and the maximum error in the computed pressure for $(x_1 - L/2) < 0.9c$ is 2.7%.

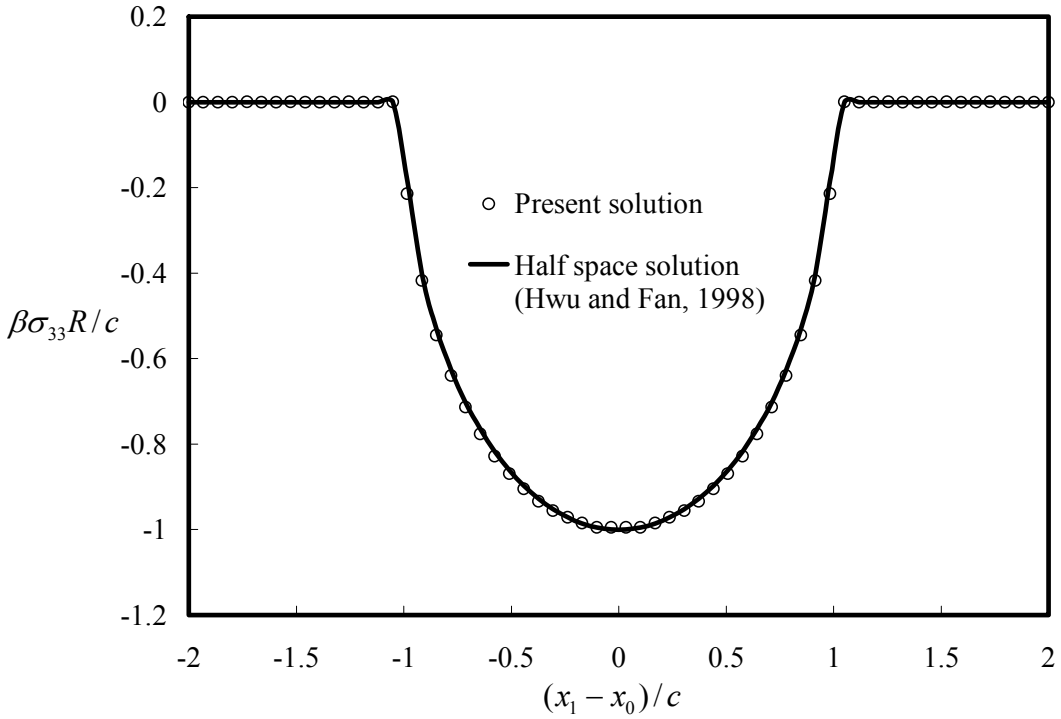

Figure 2.2 For an orthotropic layer, comparison of the presently computed pressure distribution on the contact surface with that of Hwu and Fan (1998).

2.4.2 Indentation of an isotropic elastic layer by a smooth rigid cylinder

For $c/h<1$, Meijers (1968) has derived the following expression for the pressure on the contact surface between a smooth rigid circular cylinder of radius R and an isotropic elastic layer perfectly bonded to a rigid base.

$$\sigma_{33}=-\frac{E}{2(1-\nu^2)}\frac{\sqrt{c^2-(x_1-L/2)^2}}{R}$$
$$\left[1+\frac{1}{8}\alpha_1\left(\frac{c}{h}\right)^2+\frac{1}{64}\left(\alpha_1^2+5\alpha_2+4\alpha_2(x_1-L/2)^2/c^2\right)\left(\frac{c}{h}\right)^4\right],\quad |x_1-L/2|<c, \tag{2.39}$$

where E equals Young's modulus, and for Poisson's ratio $\nu=0.3$, $\alpha_1=5.7278$ and $\alpha_2=-7.8479$. Values of parameters α_1 and α_2 depend upon the value of Poisson's ratio, and have been computed by Meijers (1968) for $\nu=0.0$, 0.3, 0.4, 0.45, 0.48 and 0.5. For values of *c/h* between 0 and 0.7, Meijers (1968) has shown that Eq. (2.21) gives converged values of the pressure distribution on the contact surface and of the indentation depth.

We solve the problem by the Eshelby-Stroh formalism given above and compare our solution with that of Meijers (1968). For an isotropic linear elastic material, eigen-values and eigen-vectors of the eigen-value problem defined by Eq. (2.14) are

$$p_1=p_2=p_3=i,\ p_4=p_5=p_6=-i, \tag{2.40.1}$$

$$\begin{bmatrix}1 & i & 0\\ i & -1 & 0\\ 0 & 0 & 0\end{bmatrix}\mathbf{a}=\mathbf{0}, \tag{2.40.2}$$

$$\mathbf{b}_\alpha=(\mathbf{R}^{\mathrm{T}}+p\mathbf{T})\mathbf{a}_\alpha. \tag{2.40.3}$$

That is, there are only two independent eigenvectors for isotropic materials, and the parameter β in Eq. (2.37) is given by $\beta=\frac{2(1-\nu^2)}{E}$. Ting (1982) has discussed modifications needed to get general solutions for an isotropic material. However, in

stead of following this rather complex procedure, we alter values by $\pm 1\%$ of elastic constants to get unequal eigen-values of the eigen-value problem defined by Eq. (2.14).

As shown in Figure 2.3, the presently computed pressure distribution on the contact surface matches well with that given by Meijers (1968), and the maximum deviation between the two pressure distributions for $(x_1 - L/2) < 0.9c$ is 6.0%.

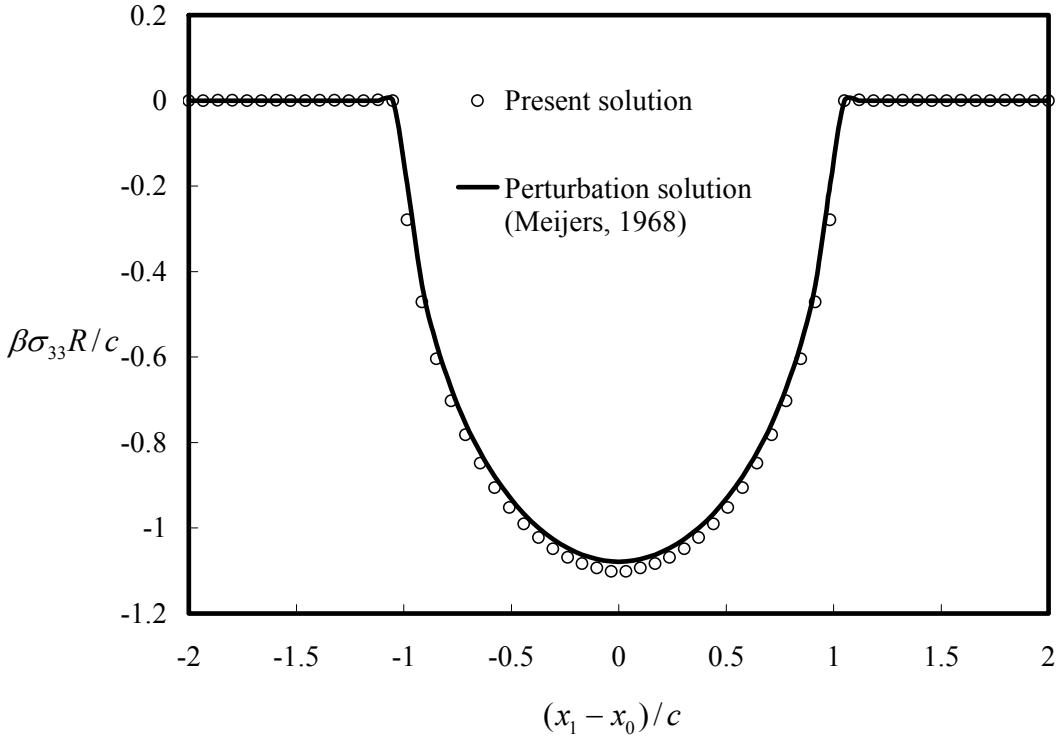

Figure 2.3 For an isotropic layer with v=0.3, c/h=1/3, c/L=0.05, comparison of the presently computed pressure distribution on the contact surface with that of Meijers (1968).

2.4.3 Effect of number of terms in the series solution

The effect of the number of terms in the series solution given by Eq. (2.23) is investigated by comparing, for the above two problems, the total axial load (cf. Eq. (2.7.1)) from the analytical solution with that obtained from the numerical solution. For an orthotropic half space indented by a smooth parabolic indenter, Eqs. (2.7.1) and (2.36) give

$$P_{\text{ortho}} = \frac{\pi c^2}{2\beta R}. \tag{2.41}$$

For an isotropic linear elastic layer bonded to a rigid substrate, we conclude from Eqs. (2.7.1) and (2.39) that

$$P_{\text{iso}} = \frac{\pi E c^2}{4(1-\nu^2)R}\left[1 + \frac{1}{8}\alpha_1\left(\frac{c}{h}\right)^2 + \frac{1}{64}\left(\alpha_1^2 + 6\alpha_2\right)\left(\frac{c}{h}\right)^4\right]. \tag{2.42}$$

For different values of $K = \sum_{n=1}^{3} K^{(n)}$, we have listed in Table 2.1 the percentage error between the axial loads given by Eqs. (2.22) and (2.23) and their values obtained from the solution of the corresponding problems with the present method. It is clear that the retention of 1600 terms in the series solution gives an error in the axial load of about 3.5%. Of course, it does not provide any information about the error in the local stresses, strains and displacements. In keeping with the goal of finding a relation between the axial load and the indentation, we accept this error in the axial load, and compute results presented herein with K = 1600.

Table 2.1 Effect of number of terms in the series solution on the percentage error in the axial loads for the contact problems involving orthotropic and isotropic layers.

Orthotropic layer (c/h=0.125, c/L=0.05; parabolic indenter)		Isotropic layer (c/h=1/3, c/L=0.05, $\nu = 0.3$; circular cylindrical indenter)	
Number, K, of terms in the series solution	$\%\ \text{Error} = 100 \cdot \left\lvert P - P_{\text{ortho}} \right\rvert / P_{\text{ortho}}$	Number, K, of terms in the series solution	$\%\ \text{Error} = 100 \cdot \left\lvert P - P_{\text{iso}} \right\rvert / P_{\text{iso}}$
400	1.9	400	7.0
600	1.3	800	5.0
800	1.0	1200	4.1
1000	0.8	1600	3.5

2.5 Parametric studies

For an orthotropic layer bonded to a rigid substrate and indented by a smooth parabolic rigid indenter, we first delineate the effect of varying geometric parameters and then material parameters. When studying the effect of geometric parameters, we

assign values to material parameters listed in Eq. (2.19); thus $\beta = 1.49\text{GPa}^{-1}$. We also have studied the influence of the coefficient of friction between the two contacting surfaces on the axial load and the depth of indentation.

2.5.1 Geometric parameters

There are four geometric parameters, namely, the radius R of the indenter, the half contact width c, and the length L and the thickness h of the deformable layer. Recall that the indentation u_0 is computed after the contact problem has been solved. Eqs. (2.36) and (2.39) suggest that lengths should be non-dimensionalized with the semi-contact width c. We thus need to study the effect of varying L/c, h/c and R/c.

Effect of changing c/h

With c, L and R kept fixed so that c/L=0.05 and c/R=0.05, and varying the layer thickness h, we have plotted in Figure 2.4 the variation with c/h of the non-dimensional axial load, P, and the non-dimensional indentation u_0/h.

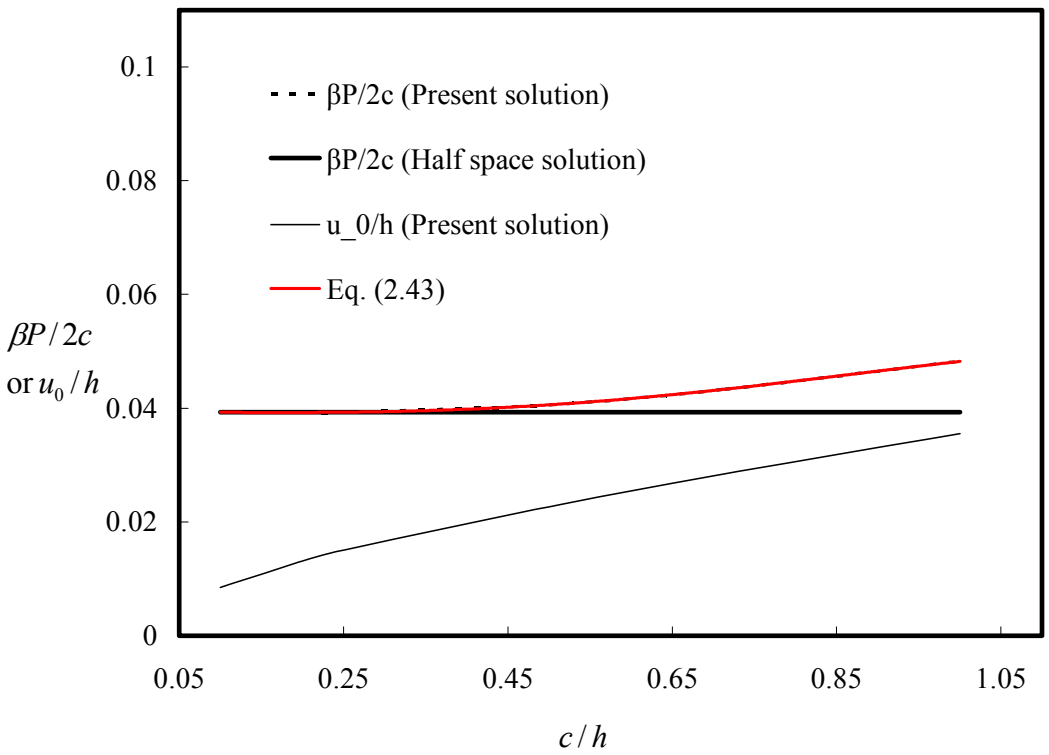

Figure 2.4 For c/L=0.05 and c/R=0.05, variation with c/h of the axial load and the depth of indentation.

It is clear that for *c/h* > 0.2, *P* for the finite thickness layer deviates noticeably from that for the half-space. Both the non-dimensional indentation and the non-dimensional axial load increase monotonically with an increase in *c/h*. Whereas the slope of the *P vs. c/h* curve continues to increase with an increase in the value of *c/h*, that of u_0/h vs. *c/h* monotonically decreases at least in the range of values of *c/h* studied herein. In addition, Figure 2.4 also shows that when *c/h* is less than about 0.6, the present computed value of *P* is very close to that obtained from the half-space solution (the error is less than 5%). For $u_0/h < 0.1$, the difference between the presently computed value of *P* and that derived from the half-space solution can be neglected. Thus the indented sample can be regarded as a half space if the indentation depth is less than 10% of the sample thickness.

The least squares fit to the computed values of $\beta P/2c$ vs. c/h is

$$\frac{\beta P}{2c} = 0.0393 - 0.0003\left(\frac{c}{h}\right) - 0.007\left(\frac{c}{h}\right)^2 + 0.0344\left(\frac{c}{h}\right)^3 - 0.0182\left(\frac{c}{h}\right)^4 \qquad (2.43)$$

It is evident from the plot of Eq. (2.43) given in Figure 2.4 that it provides a very good fit to the computed values. For $c/h \le 0.1$, one can take $\beta P/2c = 0.0393$.

Effect of changing c/R

We now set *c/L* = 0.05 and *c/h* = 0.5, and vary *R*; the corresponding axial load, *P*, is plotted in Figure 2.5. Since *c/R* can reach 0.5 in this case and the present analytical solution is only valid for small values of *c/R*, we calculate the axial load *P* by both Eqs. (2.7.1) and (2.7.2). Recall that for the half space *P* is a linear function of *c/R* with slope equal to π/4; cf. Eq. (2.41). For the finite thickness of the orthotropic layer, the slope of the *P* vs. *c/R* curve with *P* computed by using Eq. (2.7.2) is higher than π/4; the axial load *P* given by Eq. (2.7.1) is not a linear function of *c/R* for large values of *c/R*.

Effect of changing c/L

It is clear that from the results depicted in Figure 2.6 that for $0.05 < c/L < 0.2$, the ratio c/L has virtually no effect on the both the non-dimensional axial load $\beta P/2c$

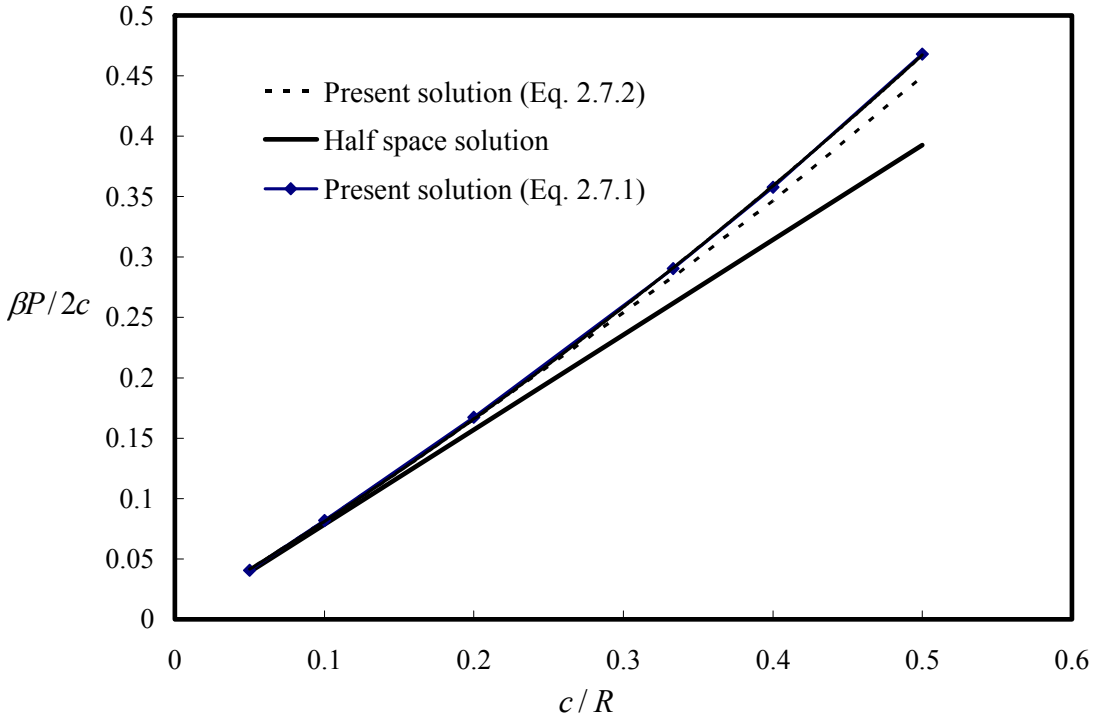

Figure 2.5 For $c/L = 0.05$ and $c/h = 0.5$, variation with c/R of the axial load.

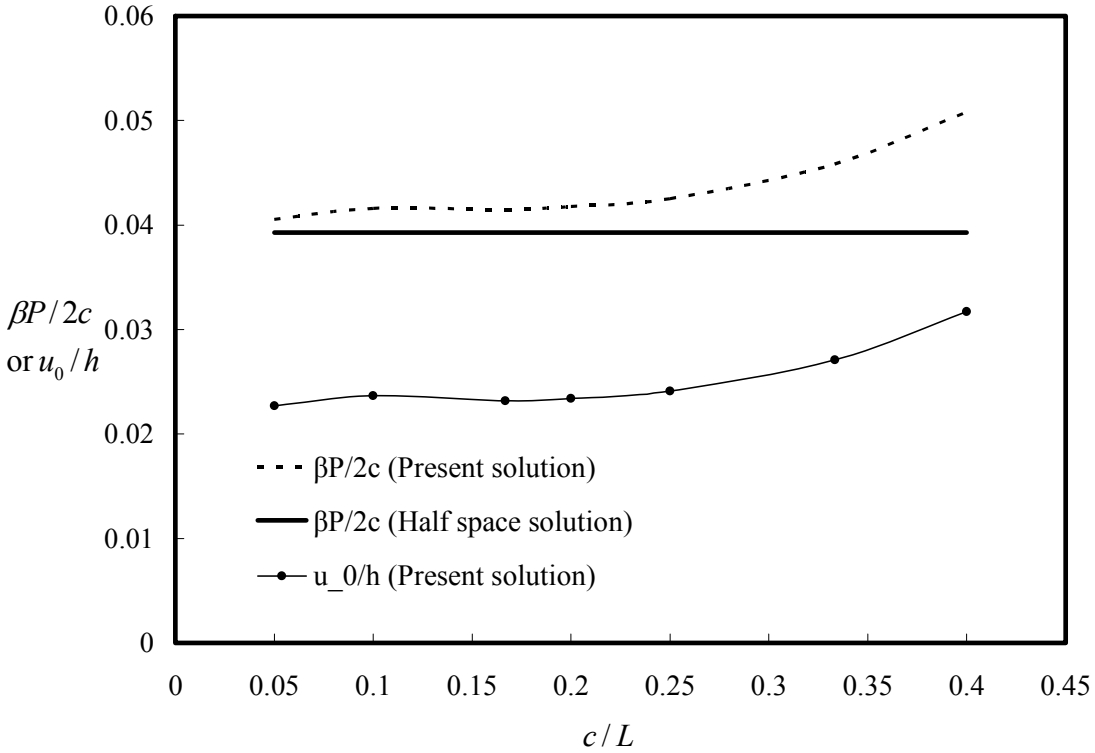

Figure 2.6 For $c/h = 0.5$ and $c/R = 0.05$, variation with c/L of the axial load and the depth of indentation.

and the non-dimensional indentation u_0/h. Whereas the non-dimensional axial load equals 0.039 for the half space, it equals 0.042 for the finite thickness layer. However, for $c/L > 0.25$, the non-dimensional axial load for the finite thickness layer is much larger than that for the half space.

Results plotted in Figures 2.4, 2.5 and 2.6 suggest that the half space solution can be used when $u_0/h \le 0.1$, $c/h \le 0.4$, $c/L \le 0.2$ and $c/R \le 0.15$.

2.5.2 Material parameters

Equation (2.36) evinces that the axial load on a parabolic indenter contacting an orthotropic half space depends on the material elasticities through the parameter β. With parameters assigned values listed in Eq. (2.38), we vary the value of one parameter at a time and determine the corresponding change in the value of β. Results of this exercise, listed in Table 2.2, illustrate that values of Young's modulus E_3 and of the shear modulus G_{13} significantly affect the value of β. Accordingly, for $c/R = 0.05$, $c/L = 0.05$ and $c/h = 0.5$, we have plotted in Figures 2.7 and 2.8 variations with E_3 and G_{13} of the axial load P and of the non-dimensional indentation u_0; values of other material parameters are the same as those given in Eq. (2.38). The axial load increases nearly linearly as E_3'/E_3 is increased from 1 to 5. Subsequently, for the same value of the half contact width, the axial load increases more rapidly with an increase in E_3'/E_3. For a ten fold increase in E_3'/E_3, the axial load increases by a factor of almost 10. However, the change in the indentation depth is less dramatic as it decreases to nearly one-half of its initial value as E_3 is enhanced by a factor of 10. The increase in G_{13} does not affect the axial load as much as the increase in E_3 does. For example, for $G_{13}'/G_{13} = 10$, the axial load for the same semi-contact width increases by about 90% and the depth of indentation by about 40%.

These results reveal that Yang and Sun's (1982), and Tan and Sun's (1985)

approximation in replacing E by E_3 in the axial load vs. the indentation relation for an isotropic material to get results for an orthotropic material dose not introduce noticeable errors. This is because values of material parameters other than E_3 do not have significant effect on the indentation load. Their approximation is equivalent to assuming that the layer material is transversely isotropic with x_3-axis as the axis of transverse isotropy. However, it remains to be seen if the approximation is reasonable for a 3D indentation test, i.e., when the x_3-dimension of the indenter and the layer is comparable to the semi- contact width.

Table 2.2 Variation in the value of β with a change in the value of one material parameter.

	$\lvert(\beta'-\beta)/\beta'\rvert$		$\lvert(\beta'-\beta)/\beta'\rvert$		$\lvert(\beta'-\beta)/\beta'\rvert$
$E_1'=10E_1$	0.056	$G_{12}'=10G_{12}$	0.000	$\nu_{12}'=0.1\nu_{12}$	0.004
$E_2'=10E_2$	0.030	$G_{13}'=10G_{13}$	1.050	$\nu_{13}'=0.1\nu_{13}$	0.004
$E_3'=10E_3$	4.364	$G_{23}'=10G_{23}$	0.000	$\nu_{23}'=0.1\nu_{23}$	0.031

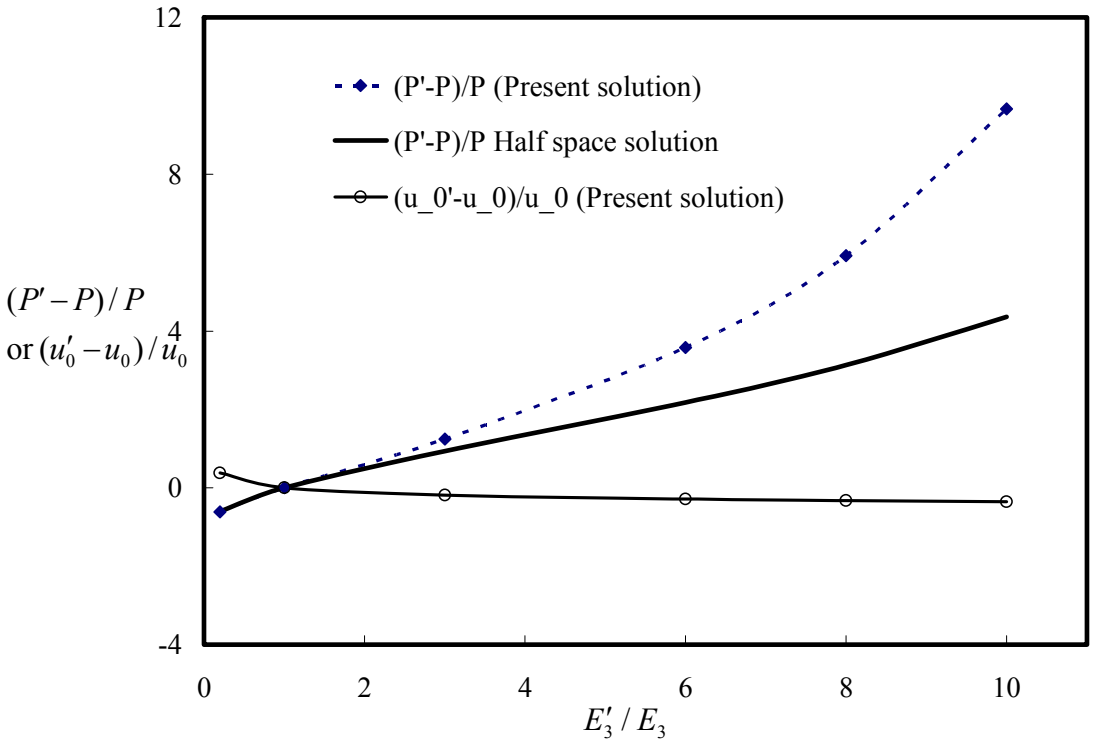

Figure 2.7 For c/R = 0.05, c/L = 0.05 and c/h = 0.5, variation with E_3'/E_3 of the axial load and the depth of indentation.

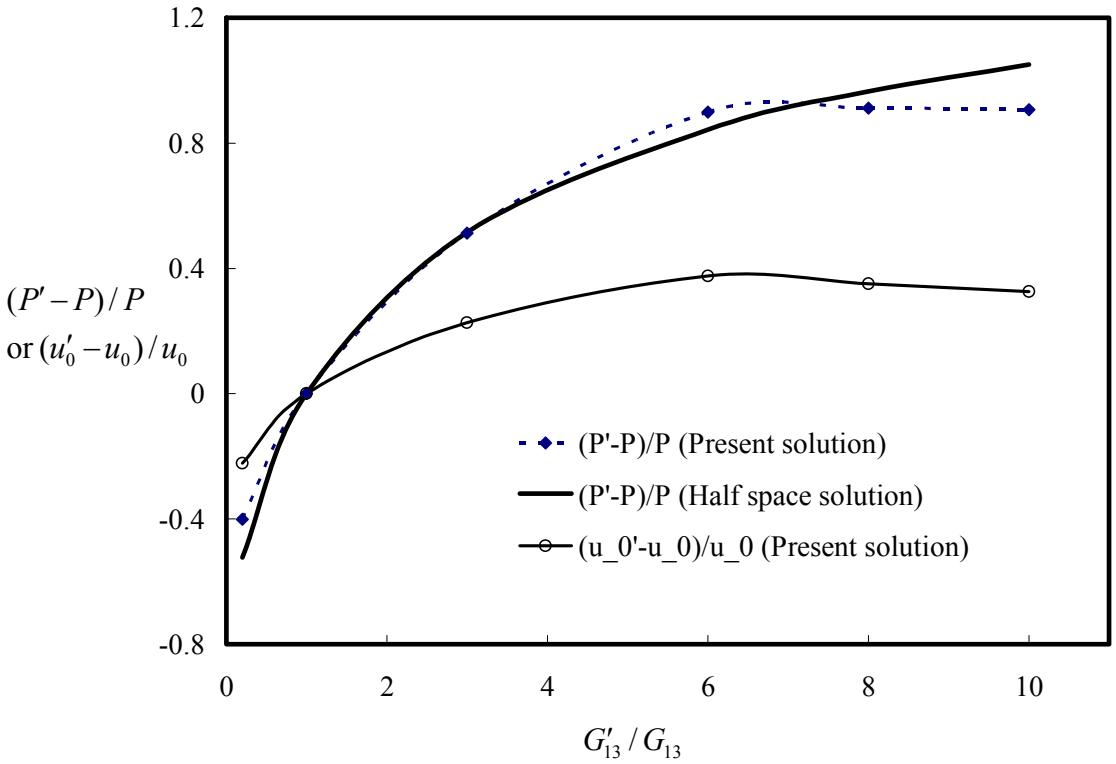

Figure 2.8 For *c/R* = 0.05, *c/L* = 0.05 and *c/h* = 0.5, variation with G_{13}'/G_{13} of the axial load and the depth of indentation.

2.5.3 Coefficient of friction

Results plotted in Figure 2.9 suggest that the axial load decreases and the indentation depth increases gradually with an increase in the value of the coefficient of friction μ. When μ is enhanced from 0 to 0.9, the average axial stress $\beta P/2c$ decreases by only 2.6% and the depth of indentation, u_0/h, increases by just 1.1%. Thus it is reasonable to assume smooth contact between the indenter and the layer.

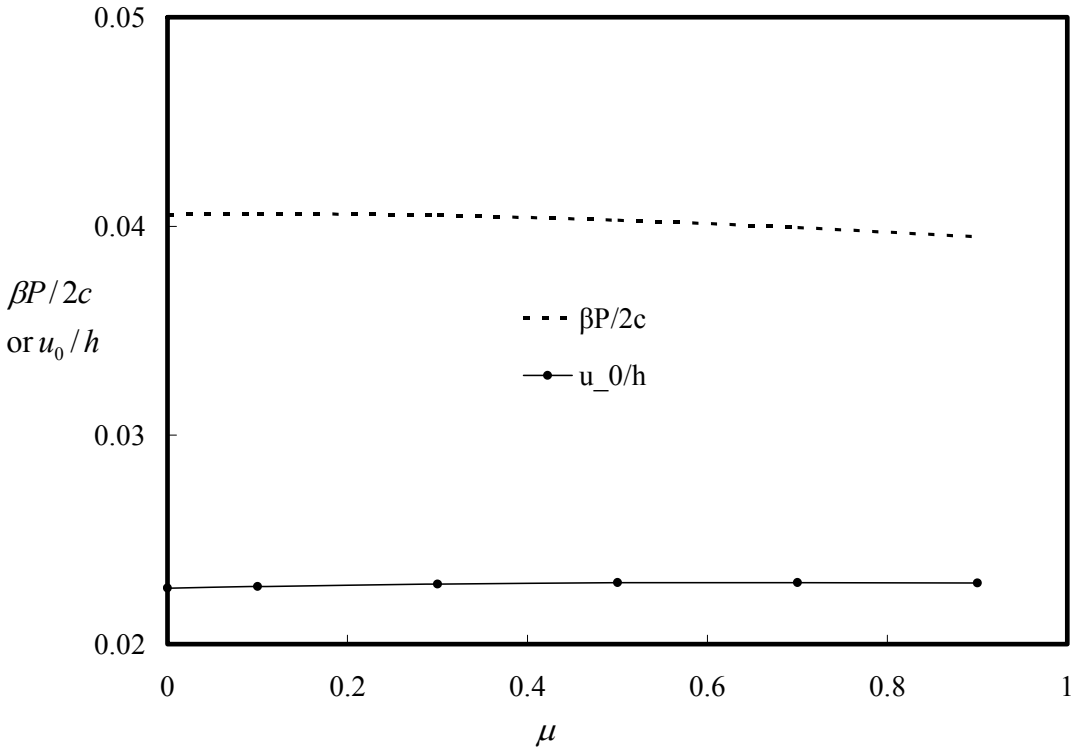

Figure 2.9 For c/R = 0.05, c/L = 0.05 and c/h = 0.5, variation with the coefficient of friction of the axial load and the depth of indentation.

2.6 Indentation with flat punch

In this section, we consider the indentation of an orthotropic layer of finite width L and finite thickness h by a rigid frictionless and flat indenter with horizontal base of width $2a$ positioned at ($L/2$-a, $L/2$+a). The indentation depth is δ. Figures 2.10 and 2.11 are plots of the x_3- displacement and of the normal stress σ_{33} acting at points on the top surface of the layer. Plots of u_3 and σ_{33} at points of the top surface that are close to the flat punch reveal that

$$\sigma_{33}(x_1,h) \sim 1/\sqrt{(L/2+a-x_1)/a} \qquad x_1 \to (L/2+a)^- \tag{2.44}$$

$$u_3(x_1,h) \sim \sqrt{(-L/2-a+x_1)/a} \qquad x_1 \to (L/2+a)^+ \tag{2.45}$$

These results agree with the analytical solution of the indentation of a linear anisotropic half space by a flat indenter (Hwu and Fan, 1998) and the asymptotic solution of the indentation of a linear elastic isotropic layer by a flat indenter (Haider

and Holmes, 1995). Except for points near the indenter periphery, the pressure distribution on the indented surface is uniform.

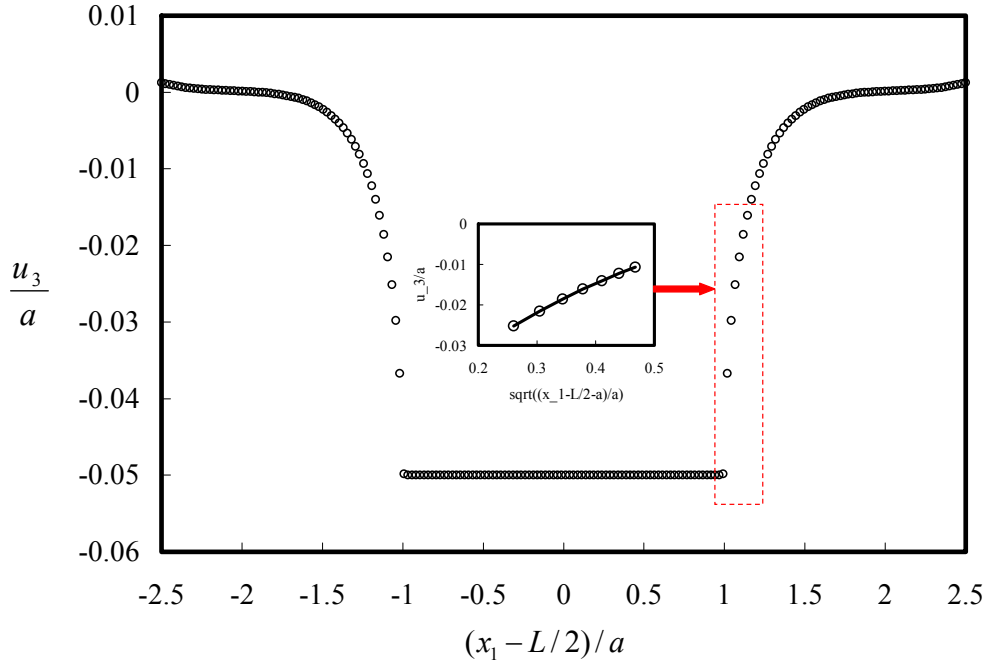

Figure 2.10 For a = 0.2m, L = 1m, h = 0.1m and δ=0.01m, plot of u_3 on the top surface and singular behavior of u_3 near the edge of the indenter.

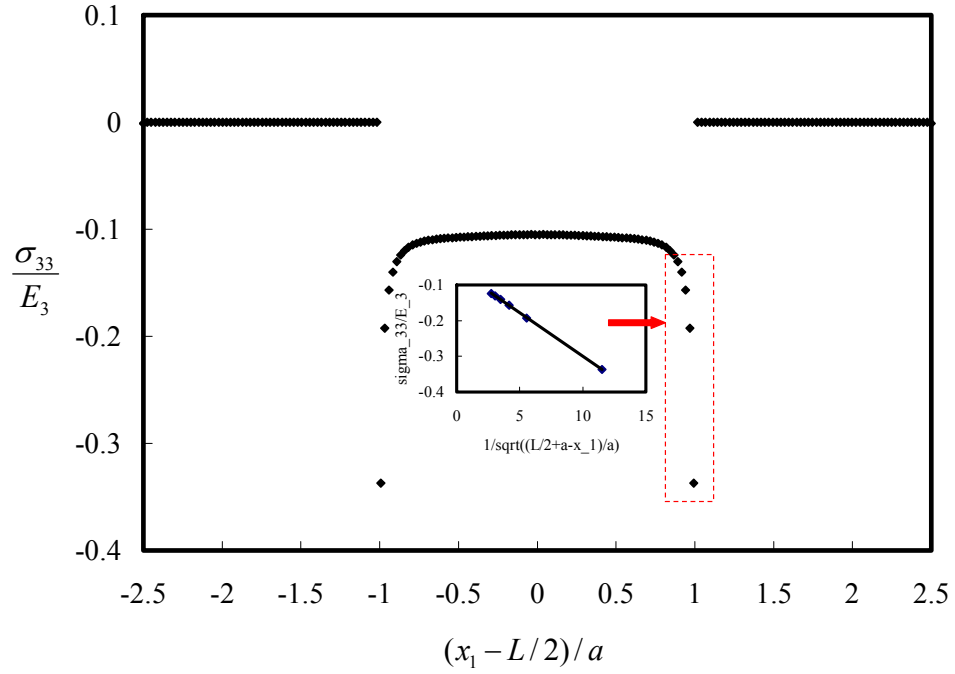

Figure 2.11 For a = 0.2m, L = 1m, h = 0.1m and δ=0.01m, plot of σ_{33} on the top surface and the singular behavior of σ_{33} near the edge of the indenter.

2.7 Conclusions

We have used the Eshelby-Stroh formalism to study infinitesimal deformations of a linear elastic anisotropic layer perfectly bonded to a rigid substrate and statically deformed by a cylindrical indenter. The problem is formulated in terms of the a priori unknown semi-contact width, c. Boundary conditions on all surfaces are satisfied in the sense of Fourier series. Computed axial loads for the indentation of an orthotropic layer by a smooth parabolic cylinder and of an isotropic layer by a smooth circular cylinder are found to compare well with the corresponding analytical solutions. The influence on the axial load of various geometric and material parameters has been delineated. These results have revealed that the non-dimensional axial load is independent of c/L for $c/L < 0.2$ where $2c$ equals the contact width and L the width of the layer. For an indenter of radius R, the non-dimensional axial load varies linearly with c/R as for a half space. However, the slope of the axial load vs. the indentation line for the finite thickness layer is higher than that of the line for the half space. The coefficient of friction between the layer material and the indenter has very little effect on the axial load required to indent the layer by a given depth. Among the material elasticities of the orthotropic layer, the elastic modulus in the direction of indentation has the most effect on the axial load and that is followed by the shear modulus in the plane of deformation. Poisson's ratios have negligible effects on the axial load.

The half space solution can be used for indentation depths less than one-tenth the layer thickness h provided that $c/h \le 0.4$, $c/L \le 0.2$ and $c/R \le 0.15$ where L is the length of the layer and R the indenter radius.

The problem formulation is valid for a general anisotropic layer. Thus indentation problems for cubic, transversely isotropic, orthotropic and isotropic materials can be analyzed even though results for only isotropic and orthotropic materials are

presented in the paper.

The problem formulation is also valid for indenters of different profiles. Results for a flat punch indenting a layer comprised of a linear elastic anisotropic material are found to match well with results available in the literature.

Chapter 3

Identification of Elastic Constants of FCC Metals from 2D Load-Indentation Curves

3.1 Introduction

Very promising engineering applications of nanocomposites and nanofilms in miniaturization of engineering and electronic components have aroused considerable interest in finding mechanical properties of these materials. A commonly used mechanical test for determining elastic moduli of a material is the indentation test. With continuous improvements in accurately measuring very small loads and indentation depths, the technique is being applied to nano-materials which are generally anisotropic. It is commonly believed that the indentation load vs. the indentation depth response during the unloading part of the test corresponds to elastic response of the indented material. An interpretation of test results and the extraction of material moduli will be facilitated if analytical expressions relating the indentation load and the indentation depth were available. For anisotropic materials one needs to ascertain values of more than one elastic constant. Thus either different types of tests (e.g., tension, torsion etc.) or similar tests on different orientations of the specimen are needed.

Analytical solutions of even linear three-dimensional (3D) boundary-value problems

for elastic bodies are hard to find. Even though solutions in the form of infinite series (or finite series with a large number of terms) for some 3D boundary-value problems are available, they are not easily applicable to test data. A possibility is to use specimen geometries and test configurations so that deformations induced can be approximated as either plane strain or plane stress. The former (latter) is usually applicable when one of the specimen dimensions is very large (small) as compared to the other two lateral dimensions. Here we study indentation problems when deformations of the indented body can be approximated as plane strain, and the indenter can be regarded as rigid. Thus elastic constants of the indenter material are very large as compared to those of the material being tested. Furthermore, by restricting indentation depths to very small values as compared to the smallest dimension of specimen, one can use solutions for the half space to interpret test results.

Doerner and Nix (1986) and Oliver and Pharr (1992) have analyzed infinitesimal deformations of a half space indented by a flat punch, and a paraboloid indenter respectively. The Oliver and Pharr (1992) solution has been widely adopted to determine the elastic modulus of the material from results of indentation tests on nanosize specimens. Doerner and Nix (1986) have given an empirical relation to account for the compliance of the substrate to which the specimen is perfectly bonded. The deformations of the substrate are usually considered when the indentation depth exceeds about 30% of the film thickness. Bhattacharya and Nix (1988a, b) used the finite element method to study elastic and plastic deformations during submicron scale indentations by conical indenters of a thin film bonded to a substrate. They developed empirical equations to determine hardness for both hard-film/soft-substrate and soft-film/hard-substrate systems. Huber et al. (2001, 2002) used neural networks, trained by results of the finite element simulations of nanoindentation, to identify values of elastic-plastic and visco-plastic material parameters.

Several works on indentation of anisotropic materials have been reviewed in Chapter

2. We note that Vlassak and Nix (1994) have provided an expression for the indentation modulus of an anisotropic solid, and have used it to interpret results of indentation experiments. By changing the orientation of the specimen, they found values of more than one elastic constant of the material. However, an examination of the indentation load vs. the indentation depth plots does not reveal any explicit correlation between experimental data and elastic moduli of anisotropic materials. Therefore, an inverse method is needed to extract values of material elasticities through suitable post-processing of the test data. Depending upon the number of independent elastic constants for an anisotropic material, the inverse process can be quite complicated. Sasaki et al. (2004) combined the finite element simulation results of nanoindentation tests with an optimization technique to determine five material parameters of a transversely isotropic material.

Spherical rather than pyramid shaped indenters have been used in indentation tests to reduce the non-axisymmetric residual stress field generated during the indentation process, and obtain more reliable data before cracks are generated. A spherical indenter has a simpler geometry than a Vickers or a Berkovitch indenter, and analytical solutions for deformations induced by a spherical indenter can be obtained for some specimen shapes and sizes.

Here we focus on finding values of three elastic constants of a face-centered cubic (FCC) material such as gold, copper, and aluminum. By assuming that the specimen can be modeled as a half space and its deformations as plane strain, we first derive an expression for the axial load in terms of elastic constants of the specimen material and the indentation depth. This relationship together with results of three indentation tests with the specimen oriented differently enables us to find values of the three elastic constants.

3.2 Load-displacement relation for an anisotropic half space indented by a rigid circular cylinder

As described in Chapter 2, Fan and Hwu (1996) and Hwu and Fan (1998) have used the Eshelby-Stroh formalism to analyze the 2D generalized plane strain contact problem in which a long parabolic cylinder indents a linear elastic, anisotropic and homogeneous half space. They focused on finding the stress distribution on the contact surface, and did not provide an explicit relation between the axial load P and the indentation depth u_0. We derive here such a relation.

A schematic sketch of the contact problem being studied is shown in Figure 3.1. In rectangular Cartesian coordinates, equations governing generalized plane strain deformations of the half space are

$$\sigma_{ij,j} = 0\,, \tag{3.1}$$

$$\sigma_{ij} = C_{ijkl} u_{k,l}\ , \tag{3.2}$$

$$C_{ijkl} = C_{jikl} = C_{ijlk} = C_{klij}\,. \tag{3.3}$$

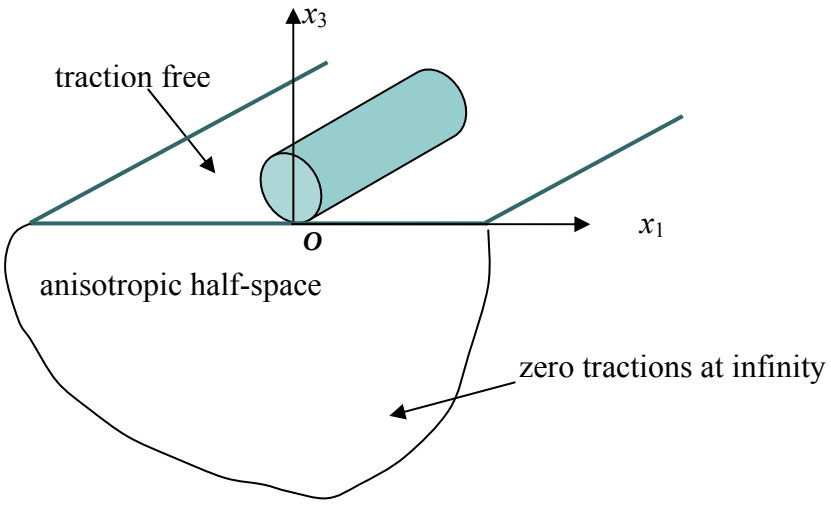

Figure 3.1 Schematic sketch of the indentation of an anisotropic half space by a rigid cylindrical indenter.

Here σ_{ij} is the Cauchy stress tensor, C_{ijkl} is an elastic constant of the material of the half space, a comma followed by index j indicates partial differentiation with

respect to the position x_j of a material point, and a repeated index implies summation over the range of the index. The length of the cylinder in the x_2- direction is large as compared to its diameter, the contact width, and the indentation depth. Hence a generalized plane strain state of deformation in the x_1x_3- plane is considered in the sense that all three displacement components and stresses induced are presumed not to depend upon x_3.

Using Stroh's formalism (Stroh, 1958, 1962), we can write a general solution of Eqs. (3.1) - (3.3) as

$$\mathbf{u} = \mathbf{A}\mathbf{f}(z) + \overline{\mathbf{A}\mathbf{f}(z)}, \tag{3.4.1}$$

$$\mathbf{\Phi} = \mathbf{B}\mathbf{f}(z) + \overline{\mathbf{B}\mathbf{f}(z)}, \tag{3.4.2}$$

where $\mathbf{A} = [\mathbf{a}_1\ \mathbf{a}_2\ \mathbf{a}_3]$, $\mathbf{B} = [\mathbf{b}_1\ \mathbf{b}_2\ \mathbf{b}_3]$, $\mathbf{f}(z) = [f_1(z_1), f_2(z_2), f_3(z_3)]^{\mathrm{T}}$, $z_\alpha = x_1 + p_\alpha x_2$, p_α, $(\mathbf{a}_\alpha, \mathbf{b}_\alpha)$ $(\alpha = 1,2,3)$ are eigenvalues and eigenvectors of the fundamental elasticity matrix $\mathbf{N}$. That is,

$$\mathbf{N}\boldsymbol{\zeta} = p\boldsymbol{\zeta}, \tag{3.5.1}$$

where $\boldsymbol{\zeta} = (\mathbf{a}, \mathbf{b})$ is an eigenvector of the matrix $\mathbf{N}$ with eigenvalue p,

$$\mathbf{N} = \begin{bmatrix} -\mathbf{T}^{-1}\mathbf{R}^{\mathrm{T}} & \mathbf{T}^{-1} \\ \mathbf{R}\mathbf{T}^{-1}\mathbf{R}^{\mathrm{T}} - \mathbf{Q} & -\mathbf{R}\mathbf{T}^{-1} \end{bmatrix}, \tag{3.5.2}$$

and $Q_{ik} = C_{i1k1} = Q_{ki}$, $R_{ik} = C_{i1k3}$ and $T_{ik} = C_{i3k3} = T_{ki}$ are 3×3 matrices. The function $\mathbf{u}$ represents displacements, and the function $\mathbf{\Phi}$ serves as a potential for stresses. That is

$$\sigma_{i1} = -\phi_{i,3}, \tag{3.6.1}$$

$$\sigma_{i3} = \phi_{i,1}, \qquad i = 1,3. \tag{3.6.2}$$

The holomorphic complex valued function $\mathbf{f}(z)$ is to be determined by satisfying the equilibrium equations and the prescribed boundary conditions. The superscript T denotes the transpose, and the overbar over a variable represents its complex conjugate.

When the indentation depth u_0 is small as compared to the radius R of the circular

indenter, the profile of the circular indenter in the vicinity of the contact point (0,-u_0) in Figure 3.1 can be replaced by a parabolic indenter without introducing a significant error. The pressure on the contact surface between a smooth rigid parabolic indenter $x_3 = x_1^2/2R$, and a homogeneous anisotropic half-space is given by (e.g., see Hwu and Fan (1998), Hwu (1993))

$$\sigma_{33} = -\frac{1}{\beta R}\sqrt{a^2 - x_1^2}\,, \qquad |x_1| < a\,, \tag{3.7}$$

where contact extends from $x_1 = -a$ to $x_1 = a$, $\beta = (M^{-1})_{33}$, and $\mathbf{M}^{-1} = i\mathbf{A}\mathbf{B}^{-1}$. Since the matrix $\mathbf{M}$ is Hermitian (Ting, 1996), i.e., $\mathbf{M} = \overline{\mathbf{M}}^{\mathrm{T}}$, $(M^{-1})_{33}$ is a real number. For an orthotropic material

$$\frac{1}{\beta} = \frac{1}{(M^{-1})_{33}} = \sqrt{\frac{C_{55}(\sqrt{C_{11}C_{33}} - C_{13})}{C_{11}(C_{13} + 2C_{55} + \sqrt{C_{11}C_{33}})}}\left(C_{13} + \sqrt{C_{11}C_{33}}\right). \tag{3.8}$$

Here C_{ij} is an elastic constant of the orthotropic half space in the contracted notation in which the stress and the strain tensors are written as six dimensional vectors, and the 4th order elasticity tensor C_{ijkl} as a 6×6 symmetric matrix.

Barnett and Lothe (1975) and Ting (1996) have given the following expression for the displacement field in an orthotropic half-space loaded by a line force $\mathbf{f} = -[f_1 \quad f_2 \quad f_3]^{\mathrm{T}}$.

$$\mathbf{u} = \frac{1}{\pi}\mathrm{Im}\{\mathbf{A} < \ln z_* > \mathbf{B}^{-1}\mathbf{f}\}, \tag{3.9}$$

where $< \ln z_* >= \mathrm{diag}[\ln z_1, \ln z_2, \ln z_3]$. For a line load only in the vertical direction, i.e., (f_1=f_2=0), Eq. (3.9) gives the following expression for the vertical displacement of a point of the half space:

$$u_3 = -\frac{f_3}{\pi}\mathrm{Im}\left[A_{31}(B^{-1})_{13}\ln z_1 + A_{32}(B^{-1})_{23}\ln z_2 + A_{33}(B^{-1})_{33}\ln z_3\right]. \tag{3.10}$$

Thus for a point on the vertical axis

$$u_3(x_1,0) = -\frac{f_3}{\pi}\mathrm{Im}\left[A_{31}(B^{-1})_{13} + A_{32}(B^{-1})_{23} + A_{33}(B^{-1})_{33}\right]\ln x = \frac{f_3(M^{-1})_{33}}{\pi}\ln x \tag{3.11}$$

For the contact problem being studied here, the displacement of a point on the vertical axis can be computed from Eq. (3.11) by setting $f_3 = \sigma_{33} ds$ and integrating the right-hand side of the resulting equation from - *a* to + *a*. The result is

$$u_3(x,0) = -\frac{(M^{-1})_{33}}{\pi} \int_{-a}^{a} \sigma_{33}(s) \ln|x-s| ds \,. \tag{3.13}$$

Substituting for σ_{33} from Eq. (3.7) into Eq. (3.13), we obtain

$$u_3(x,0) = \frac{1}{\pi R} \int_{-a}^{a} \sqrt{a^2 - s^2} \ln|x-s| ds \,. \tag{3.14}$$

Noting that Eq. (3.14) has been derived without using any essential boundary condition, we remove the rigid body translation by measuring the vertical displacement of a point relative to that a reference point $(x_0,0)$; e.g. see Johnson (1985, p.17). Thus

$$u_3'(x_1,0) = u_3(x_1,0) - u_3(x_0,0) = \frac{1}{\pi R} \int_{-a}^{a} \sqrt{a^2 - s^2} \ln\left|\frac{x_1 - s}{x_0 - s}\right| ds \,, \tag{3.15}$$

$u_3'(x_0,0) = 0$, and the prime indicates the displacement of a point relative to that of the point $(x_0,0)$.

The indentation depth u_0 can be computed from

$$u_0 = -u_3(0,0) + u_3(x_0,0) = -\frac{1}{\pi R} \int_{-a}^{a} \sqrt{a^2 - s^2} \ln \frac{|s|}{x_0 - s} ds = \frac{a^2}{2R}\left[-\ln a + \ln(2x_0\sqrt{e})\right] + O\left(\frac{1}{x_0^2}\right) \tag{3.16}$$

Also, the axial load *P* per unit length of the indenter found by integrating Eq. (3.7) over the contact width is given by

$$P = \int_{-a}^{a} \sigma_{33}(x_1,0) dx_1 = \frac{\pi a^2}{2\beta R} \,. \tag{3.17}$$

We choose the reference point on the free surface of the half space and far from the contact area, i.e., $x_1 >> a$. Solving Eq. (3.17) for *a* and substituting for *a* in Eq. (3.16), we obtain the following load-displacement relation for the contact problem:

$$-\frac{1}{\beta}\frac{\pi u_0}{P} = \ln\sqrt{P} - \ln\sqrt{P_0} \,, \tag{3.18}$$

where $P_0 = \dfrac{2\pi e x_0^2}{\beta R}$.

3.3 Determination of elasticities of a cubic material

3.3.1 Method

An FCC single crystal is a cubic material and has three independent elastic constants. With lattice directions [100], [010] and [001] aligned along the rectangular Cartesian coordinate axes, the 6×6 matrix **C** of elasticities has the following form:

$$\mathbf{C} = \begin{bmatrix} C_{11} & C_{12} & C_{12} & 0 & 0 & 0 \\ C_{12} & C_{11} & C_{12} & 0 & 0 & 0 \\ C_{12} & C_{12} & C_{11} & 0 & 0 & 0 \\ 0 & 0 & 0 & C_{44} & 0 & 0 \\ 0 & 0 & 0 & 0 & C_{44} & 0 \\ 0 & 0 & 0 & 0 & 0 & C_{44} \end{bmatrix} \tag{3.19}$$

With respect to rectangular Cartesian coordinate axes x_i' (i=1, 2, 3) obtained by rotating axes x_j with the matrix **a** given by

$$\mathbf{a} = \begin{bmatrix} a_{11} & a_{12} & a_{13} \\ a_{21} & a_{22} & a_{23} \\ a_{31} & a_{32} & a_{33} \end{bmatrix}, \tag{3.20}$$

where a_{ij} equals cosine of the angle between x_i' and x_j, the matrix $\mathbf{C}'$ of elasticities is related to the matrix **C** by

$$\mathbf{C}' = \mathbf{Q}\mathbf{C}\overline{\mathbf{Q}}^{-1} \tag{3.21}$$

where

$$\mathbf{Q} = \begin{bmatrix} a_{11}^2 & a_{12}^2 & a_{13}^2 & 2a_{12}a_{13} & 2a_{11}a_{13} & 2a_{11}a_{12} \\ a_{21}^2 & a_{22}^2 & a_{23}^2 & 2a_{22}a_{23} & 2a_{21}a_{23} & 2a_{21}a_{22} \\ a_{31}^2 & a_{32}^2 & a_{33}^2 & 2a_{32}a_{33} & 2a_{31}a_{33} & 2a_{31}a_{32} \\ a_{21}a_{31} & a_{22}a_{32} & a_{23}a_{33} & a_{23}a_{32}+a_{22}a_{33} & a_{23}a_{31}+a_{33}a_{21} & a_{31}a_{22}+a_{32}a_{21} \\ a_{31}a_{11} & a_{32}a_{12} & a_{33}a_{13} & a_{32}a_{13}+a_{33}a_{12} & a_{31}a_{13}+a_{33}a_{11} & a_{31}a_{12}+a_{32}a_{11} \\ a_{11}a_{21} & a_{12}a_{22} & a_{13}a_{23} & a_{13}a_{22}+a_{12}a_{23} & a_{13}a_{21}+a_{11}a_{23} & a_{12}a_{21}+a_{11}a_{22} \end{bmatrix} \tag{3.22}$$

and

$$\overline{\mathbf{Q}} = \begin{bmatrix} a_{11}^2 & a_{12}^2 & a_{13}^2 & a_{12}a_{13} & a_{11}a_{13} & a_{11}a_{12} \\ a_{21}^2 & a_{22}^2 & a_{23}^2 & a_{22}a_{23} & a_{21}a_{23} & a_{21}a_{22} \\ a_{31}^2 & a_{32}^2 & a_{33}^2 & a_{32}a_{33} & a_{31}a_{33} & a_{31}a_{32} \\ 2a_{21}a_{31} & 2a_{22}a_{32} & 2a_{23}a_{33} & a_{23}a_{32}+a_{22}a_{33} & a_{23}a_{31}+a_{33}a_{21} & a_{31}a_{22}+a_{32}a_{21} \\ 2a_{31}a_{11} & 2a_{32}a_{12} & 2a_{33}a_{13} & a_{32}a_{13}+a_{33}a_{12} & a_{31}a_{13}+a_{33}a_{11} & a_{31}a_{12}+a_{32}a_{11} \\ 2a_{11}a_{21} & 2a_{12}a_{22} & 2a_{13}a_{23} & a_{13}a_{22}+a_{12}a_{23} & a_{13}a_{21}+a_{11}a_{23} & a_{12}a_{21}+a_{11}a_{22} \end{bmatrix} \tag{3.23}$$

As shown in Figure 3.2, besides the x_j-axes, we consider three sets of rectangular Cartesian coordinate axes x_i', namely, those obtained by rotating the coordinate axes x_j through -45° about the x_1 - axis, the x_2 - axis, and the x_3 - axis. Values of $1/\beta$ with respect to these four sets of coordinate axes are denoted below by $(1/\beta)_{\mathrm{I}}$, $(1/\beta)_{\mathrm{II}}$, $(1/\beta)_{\mathrm{III}}$, and $(1/\beta)_{\mathrm{IV}}$ respectively; their values in terms of elements of the matrix C are given below as Eqs. (3.24).

$$\left(\frac{1}{\beta}\right)_{\mathrm{I}} = \left(\frac{1}{\beta}\right)_{\mathrm{III}} = \sqrt{\frac{C_{44}(C_{11}-C_{12})}{C_{11}\gamma}}\left(C_{12}+C_{11}\right) \tag{3.24.1}$$

$$\left(\frac{1}{\beta}\right)_{\mathrm{II}} = \sqrt{\frac{C_{44}(\sqrt{C_{11}\gamma/2}-C_{12})}{C_{11}\left(C_{12}+2C_{44}+\sqrt{C_{11}\gamma/2}\right)}}\left(C_{12}+\sqrt{C_{11}\gamma/2}\right), \tag{3.24.2}$$

$$\left(\frac{1}{\beta}\right)_{\mathrm{IV}} = \sqrt{\frac{2C_{44}(\sqrt{C_{11}\gamma/2}-C_{12})}{\gamma\left(C_{12}+2C_{44}+\sqrt{C_{11}\gamma/2}\right)}}\left(C_{12}+\sqrt{C_{11}\gamma/2}\right) \tag{3.24.3}$$

$$\gamma = C_{12}+2C_{44}+C_{11} \tag{3.24.4}$$

By dividing each side of Eq. (3.24.3) by the corresponding side of Eq. (3.24.2), we obtain

$$\left(\frac{1}{\beta}\right)_{\mathrm{IV}} \Big/ \left(\frac{1}{\beta}\right)_{\mathrm{II}} = \sqrt{\frac{2}{\gamma}}\,. \tag{3.24.4}$$

The three unknowns C_{11}, C_{12}, C_{44} can be determined in terms of $(1/\beta)_{\mathrm{I}}$, $(1/\beta)_{\mathrm{II}}$, $(1/\beta)_{\mathrm{III}}$ and $(1/\beta)_{\mathrm{IV}}$ by simultaneously solving Eqs. (3.24.1), (3.24.2) and (3.24.4).

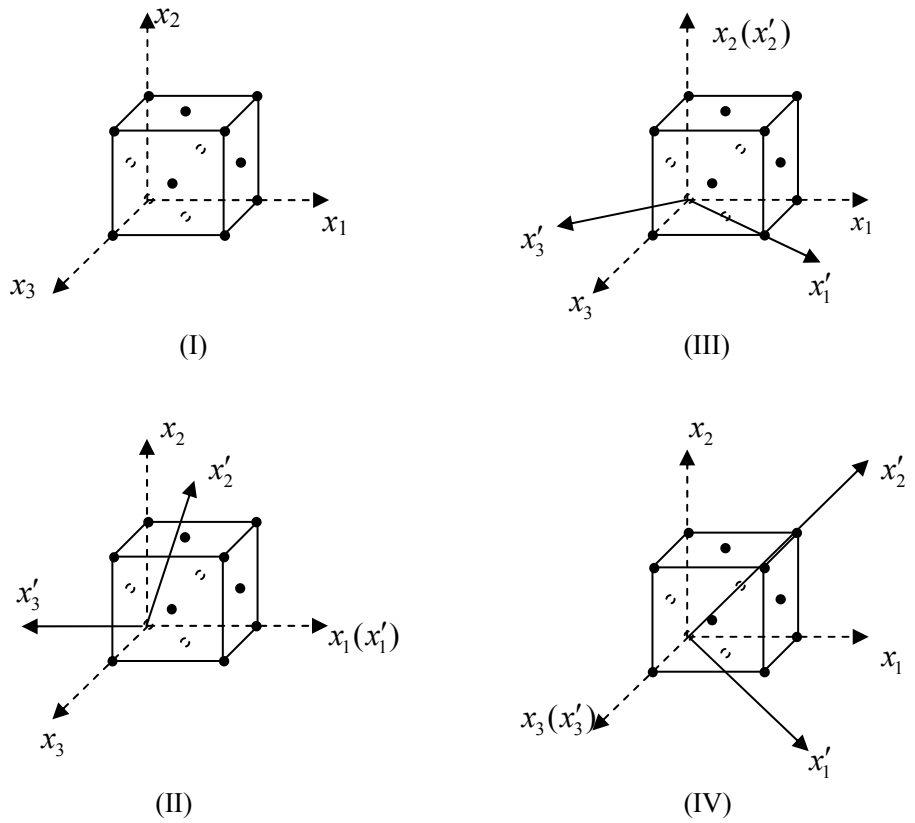

Figure 3.2 (I) Rectangular Cartesian coordinate axes x_j aligned with the lattice directions [100], [010] and [001]; (II) – (IV) rectangular Cartesian coordinate axes x_i' obtained by rotating axes x_j through -45° about the x_1 - axis, the x_2 - axis, and the x_3 - axis respectively.

We propose the following procedure for finding the three elastic constants of an FCC material. Perform indentation tests on a sample of the material with lattice vectors coincident with the four sets of coordinate axes x_i' given above, and find the corresponding values of $(1/\beta)$ by using slopes of the axial load versus indentation curves and Eq. (3.18). Then solve simultaneously Eqs. (3.24.1), (3.24.2) and (3.24.4) for C_{11}, C_{12} and C_{44}.

3.3.2 Application of the Method

We use the above-stated method to find three elastic constants of a single crystal of gold. We use numerical method developed in Chapter 2 to perform four virtual (i.e., numerical) indentation tests on a gold crystal of dimensions 204 Å × 102 Å with lattice vectors oriented as stated in Section 3.3.1. The radius of the cylinder in the

four numerical experiments is taken to be 40Å. The bottom surface of the layer is kept fixed, the left and the right surfaces are traction free, and the top surface is indented with a parabolic indenter. During all simulations, the indentation is kept less than 10.2 Å, (i.e., 10 % of the height of the specimen) and the contact width less than 20 Å (i.e., less than 10 % of the specimen width). These constraints should minimize the effect of boundary conditions on the left and the right surfaces, and ensure that the relation (3.18) between the axial load and the indentation depth for the half space derived in Section 3.2 is approximately valid.

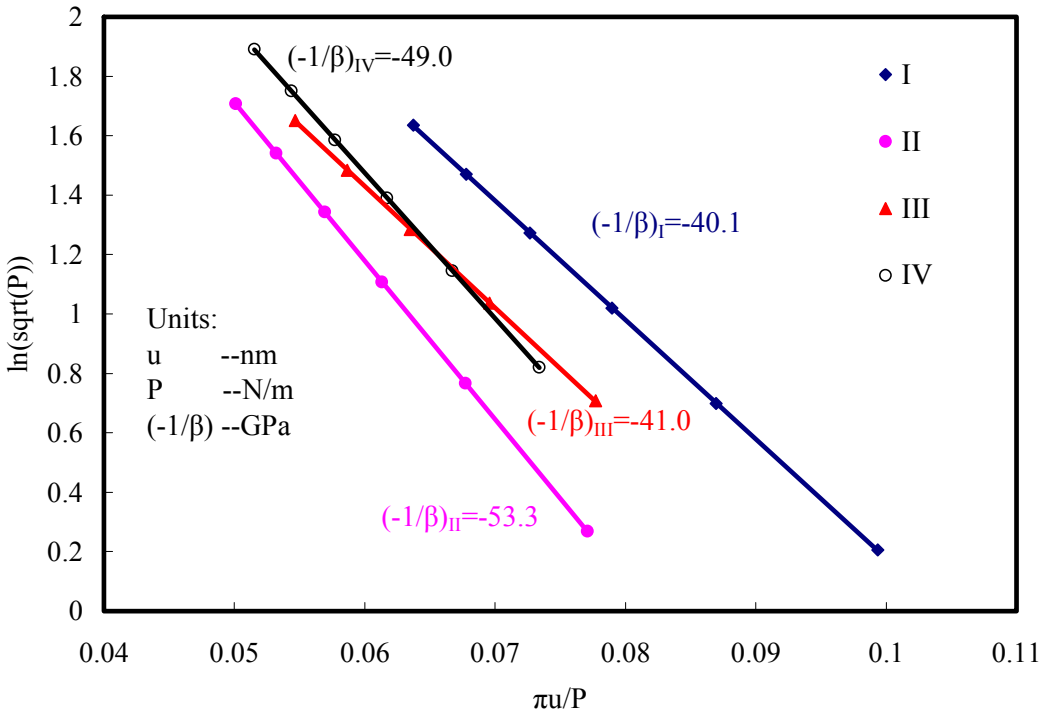

Figure 3.3 Plot of the indentation load versus the indentation depth for four virtual experiments on a gold crystal.

We assume that a gold crystal can be modeled as a continuum, and the analysis of Section 3.2 is applicable to the indentation of the gold crystal. We plot results of our virtual tests in the form of the indentation load versus the indentation depth curves as shown in Figure 3.3. Eq. (3.18) implies that the plot of $\ln\sqrt{P}$ versus $\pi u_0/P$ should be a straight line. Accordingly, we fit straight lines by the least squares method to the data plotted in Figure 3.3 and find slopes of the lines with the following results.

$$(1/\beta)_{\mathrm{I}} = 40.1\mathrm{GPa}$$

$$(1/\beta)_{\text{II}} = 53.3\text{GPa}$$
$$(1/\beta)_{\text{III}} = 41.0\text{GPa}$$
$$(1/\beta)_{\text{IV}} = 49.0\text{GPa} \qquad (3.25)$$

Since results for tests 1 and 3 should be the same, we take average of values of $(1/\beta)_{\text{I}}$ and $(1/\beta)_{\text{III}}$, and set $(1/\beta)_{\text{I}} = (1/\beta)_{\text{III}} = 40.55\text{GPa}$. Substitution from Eq. (3.25) into Eqs. (3.24.1), (3.24.2) and (3.24.4) and solving simultaneously these three equations, we get

$$C_{11} = 179.3\text{GPa}, \quad C_{12} = 154.5\text{GPa}, \quad C_{44} = 45.3\text{GPa}$$

which differ by less than 3% from the values of C_{11}, C_{12} and C_{44} used as input into the code.

Here we have conducted virtual experiments in which it is possible to find precisely the four orientations of the specimen. However, in a laboratory, there may be errors introduced in rotating the specimen through the desired angle. Accordingly, we conducted another set of numerical tests in which the angle of rotation was set randomly between -39° and -51°. Results of these simulations are depicted in Figure 3.4. Following the same procedure as for the analysis of results plotted in Figure 3.3, we get $C_{11} = 166.1\text{GPa}$, $C_{12} = 142.6\text{GPa}$, $C_{44} = 47.4\text{GPa}$, which differ from their values input into the code by less than 10.3% .

3.3.3 Remarks

One possible difficulty in adopting the procedure outlined above to physical experiments is to use a very long cylindrical indenter. For commonly used conical and spherical indenters, deformations of the indented body can not be approximated as 2D. Whereas one can deduce load-indentation plots through numerical experiments, the identification of material elasticities becomes an iterative process. For finding all three elastic constants of an FCC metal, the iterative process can become computationally expensive. The situation is further compounded if the lattice orientation can not be a priori determined.

The proposed technique can also be applied to find elastic constants of materials of other symmetries. For example, one will need five (six) suitably selected linearly independent orientations of the specimen for a transversely isotropic (an orthotropic) material so that all elastic constants appear at least once in the expression for the slope of the load vs. indentation curve. Since β given by Eq. (3.8) is a nonlinear function of the material elasticities, one will need to solve simultaneously a system of five or six nonlinear algebraic equations to evaluate the material elasticities. If necessary, these equations can be solved by an iterative method.

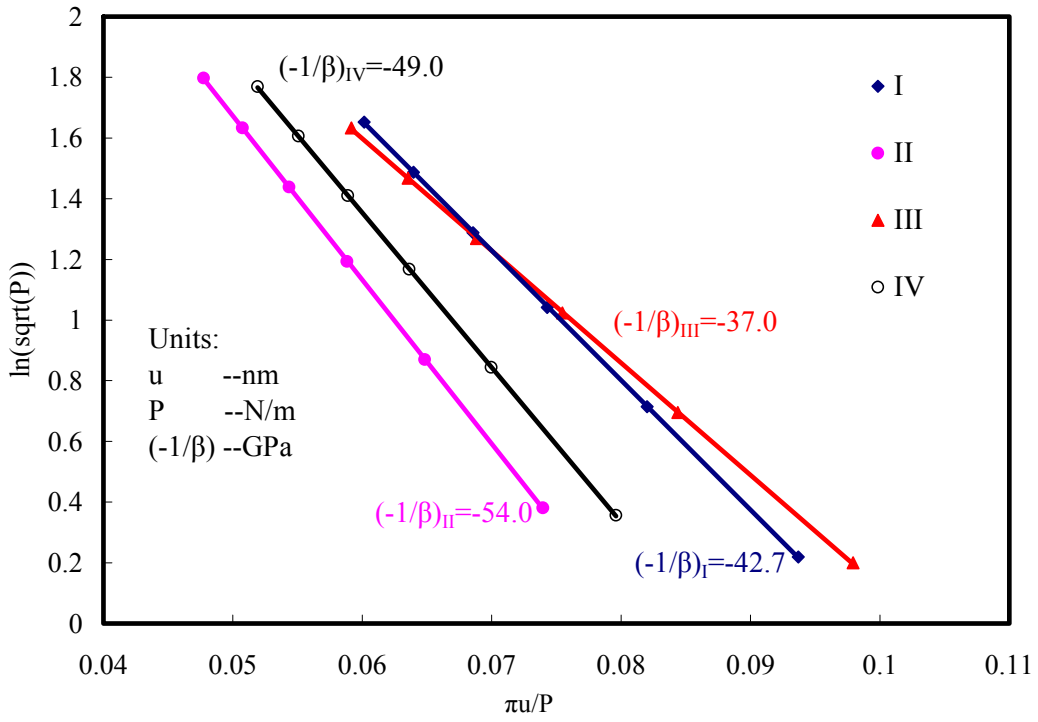

Figure 3.4 Plot of the indentation load versus the indentation depth for four virtual experiments on a gold crystal with specimens mis-oriented by less than 6°.

3.4 Conclusions

We have developed an expression relating the axial load to the depth of indentation for plane strain deformations of an anisotropic half space indented by a rigid parabolic indenter. This expression involves material elasticities. By using results of three indentation tests on a face centered cubic material with each test performed on a differently oriented specimen, we obtain three linearly independent equations for the

three elastic constants. It is shown that when the indentation depth and the contact width are less than 10% of the smallest dimension of the thin layer of the specimen bonded to a relatively rigid substrate, then the proposed inverse method yields very good values of the three elastic constants of a face centered cubic material.

Chapter 4

Relations between Continuum Stress and Strain Tensors, and MM Simulations of Mechanical Tests

4.1 Introduction

The key to multiscale modeling is to bridge length and time scales between continuum variables and quantities defined at the atomic level. Thus one needs to establish equivalence among continuum field variables, such as stress, strain, temperature, elastic constants, heat flux and temperature and the atomic variables such as the positions of atoms, their velocities, and material parameters appearing in the molecular mechanics/dynamics (MM/MD) potential. One thus needs to find continuum structures whose thermo-mechanical response to external stimuli (e.g., surface tractions, temperatures and the heat flux) is equivalent to that of the atomic system exposed to the same external stimuli. For a given material, the motion of atoms is generally governed by the MM/MD potential which also determines characteristics of the equivalent continuum structure (ECS).

A commonly used definition of stress tensor in atomistic studies using MD potentials is the virial stress that is based on a generalization of the virial theorem of Clausius

(1870) for gas pressure, and has two parts. One part is associated with the motion of atoms across a fixed spatial surface through a point. This motion of atoms 'exerts' forces on the surface. The other part of the virial stress arises from interatomic forces. Considering these two effects Lutsko (1988) has derived, an expression similar to the virial stress, by applying the continuum equation of the balance of linear momentum to an atomic system, and averaging computed stresses over the volume of the continuum region perceived to equal the region occupied by the atomic system. However, Zhou (2003) has mentioned that Lutsko's use of the material time derivative is probably incorrect. Furthermore, there is some disagreement about contributions from the kinetic terms to Lutsko's definition of the stress. Some authors (e.g., see Irving and Kirkwood (1950), and Hardy (1982)) have argued that only the fluctuation part of the velocity of an atom should be used to find the virial stress. Zhou (2003) assumed that the motion of a particle does not directly exert mechanical forces on other particles or surfaces, and the interatomic force term alone determines stresses and can be identified with the Cauchy stress tensor. However, kinetic terms do not appear in MM simulations in which the temperature of all atoms is assumed to be steady and equal 0 K, and atoms are assumed to move rather slowly so as not to affect their temperatures. Therefore, for a pair-wise inter-atomic potential, the average Cauchy stress $\overline{\boldsymbol{\sigma}}$ in a region of volume Ω can be written as

$$\overline{\boldsymbol{\sigma}} = \frac{1}{2\Omega} \sum_{\alpha} \sum_{\beta(\neq\alpha)} \mathbf{r}^{\alpha\beta} \otimes \mathbf{f}^{\alpha\beta} \tag{4.1}$$

where $\mathbf{r}^{\alpha\beta} = \mathbf{r}^{\beta} - \mathbf{r}^{\alpha}$ gives the relative position of atom β with respect to that of atom α, and $\mathbf{f}^{\alpha\beta}$ is the interatomic force applied on atom α by atom β. Here and below, superscript Greek indices refer to atom number, Latin letters used as subscripts to components of a tensor with respect to a rectangular Cartesian coordinate system, and summations only on Latin repeated indices are implied. For radially symmetric potentials such as pairwise potentials found by the embedded atom method (EAM), the potential energy of a system of atoms depends only on the interatomic distance, and the interatomic force $\mathbf{f}^{\alpha\beta}$ is assumed to be given by

$$\mathbf{f}^{\alpha\beta} = \frac{\partial \phi(r^{\alpha\beta})}{\partial \mathbf{r}^{\alpha\beta}} = \frac{\partial \phi(r^{\alpha\beta})}{\partial r^{\alpha\beta}} \frac{\mathbf{r}^{\alpha\beta}}{r^{\alpha\beta}}. \tag{4.2}$$

Substitution from Eq. (4.2) into Eq. (4.1) gives

$$\overline{\boldsymbol{\sigma}} = \frac{1}{2\Omega} \sum_{\alpha} \sum_{\beta(\neq\alpha)} \frac{\partial \phi(r^{\alpha\beta})}{\partial r^{\alpha\beta}} \frac{\mathbf{r}^{\alpha\beta} \otimes \mathbf{r}^{\alpha\beta}}{r^{\alpha\beta}}, \tag{4.3}$$

where $\phi(r^{\alpha\beta})$ is the energy of the atomic system, and $\otimes$ denotes the tensor product between two vectors.

Thus in MM simulations, the local Cauchy stress $\boldsymbol{\sigma}^{\alpha}$ in the ECS at the point that corresponds to atom α can be written as

$$\boldsymbol{\sigma}^{\alpha} = \frac{1}{2\Omega^{\alpha}} \sum_{\beta(\neq\alpha)} \mathbf{r}^{\alpha\beta} \otimes \mathbf{f}^{\alpha\beta} \tag{4.4}$$

where Ω^{α} is the volume associated with atom α.

We note that Eq. (4.4) gives stresses at discrete points, namely, present spatial locations of atoms in the ECS. Zhou (2003) proposed the following expression (4.5) for finding the Cauchy stress at points on the line joining current positions of atoms α and β.

$$\boldsymbol{\sigma}(\mathbf{r}) = \frac{1}{2} \sum_{\alpha} \sum_{\beta(\neq\alpha)} \mathbf{r}^{\alpha\beta} \otimes \mathbf{f}^{\alpha\beta} \delta[\mathbf{r} - (\mathbf{r}^{\beta\alpha} l + \mathbf{r}^{\beta})] \tag{4.5}$$

Here $0 < l < 1$, $\delta[\mathbf{r} - (\mathbf{r}^{\beta\alpha} l + \mathbf{r}^{\beta})]$ is the Dirac delta function and the summation is performed over all particles in the system. It is non-zero along the line segment joining $\mathbf{r}^{\alpha}$ and $\mathbf{r}^{\beta}$ and is zero elsewhere. The integral of $\delta[\mathbf{r} - (\mathbf{r}^{\beta\alpha} l + \mathbf{r}^{\beta})]$ over the whole volume equals one so we can regard this delta function as having the dimension of (volume)$^{-1}$. Eq. (4.5) does not provide smooth distribution of stresses as is likely to be the case in a continuous body.

Shen and Atluri (2004) have used the Smoothed Particle Hydrodynamics (SPH) method to smooth out discrete forces acting at the atomic positions, and used the balance of linear momentum to compute the Cauchy stress in the ECS. We note that

the smoothing kernel of the SPH method is similar to the localization function employed by Hardy (1982), Hardy et al. (2002) and Zimmerman et al. (2004). While using the method of Fourier transform to derive an expression for the Cauchy stress, Shen and Atluri (2004) implicitly considered an infinite region and assumed that tractions vanish at the boundaries of this region.

In Section 4.2, we use the principle of virtual work to derive an expression for the Cauchy stress in terms of the MM potential. In Section 4.3, we use the Cauchy-Born rule to find the deformation gradient at positions in the ECS that correspond to atomic positions in the discrete system, and use it to characterize the onset of dislocations in plane strain indentation of a gold crystal.

4.2 Equivalent stress for a MM system

For a non-polar continuum, the stress tensor is defined as follows (e.g. see Batra, 2005). At any time, within a body, conceive a smooth, closed diaphragm. Then the action of the part of the body outside that diaphragm and adjacent to it on the part of the body inside the diaphragm is equipollent to a force field $\mathbf{t}$ defined on the diaphragm. Using the balance of linear momentum, and the assumption that $\mathbf{t}$ depends upon the orientation of the surface only through its outward unit normal $\mathbf{n}$, i.e., $\mathbf{t} = \mathbf{t}(\mathbf{r},\mathbf{n})$, it is proved that $\mathbf{t}$ is a linear function of $\mathbf{n}$. Thus

$$t_i(\mathbf{r},\mathbf{n}) = \sigma_{ij}(\mathbf{r}) n_j, \qquad i,j = 1,2,3, \tag{4.6}$$

where

$$\sigma_{ij}(\mathbf{r}) = t_i(\mathbf{r},\mathbf{e}_j), \qquad i,j = 1,2,3, \tag{4.7}$$

$\mathbf{e}_j$ is the unit vector along the x_j- axis, and $\boldsymbol{\sigma}$ is the Cauchy stress tensor. In the absence of body forces, the conservation of linear momentum implies that

$$\mathrm{div}\boldsymbol{\sigma} = \rho\ddot{\mathbf{u}}, \tag{4.8}$$

where ρ and $\mathbf{u}$ are, respectively, the mass density and the displacement of a particle, and the superimposed dot indicates material time derivative. For a static

problem

$$\text{div}\boldsymbol{\sigma} = \mathbf{0}. \tag{4.9}$$

The conservation of moment of linear momentum is satisfied if and only if

$$\sigma_{ij} = \sigma_{ji}. \tag{4.10}$$

We now briefly outline the procedure followed by Zhou (2003) and Lutsko(1988) to derive Eq. (4.5). Conceive that an atom α has a small region of volume V associated with it, and assign the same volume V to the subregion of the ECS that surrounds the point corresponding to atom α in the ECS. Then, the equation of motion for this region can be written as

$$\rho\ddot{\mathbf{u}} = \sum_{\alpha} m^{\alpha}\ddot{\mathbf{r}}^{\alpha}\delta(\mathbf{r} - \mathbf{r}^{\alpha}). \tag{4.11}$$

Eq. (4.9) should be interpreted in an integral sense, i.e., its left and right sides are integrated over the region V. Thus ρ and $\ddot{\mathbf{u}}$ equal the mean mass density and the average acceleration of the material in region V of the ECS. With $m^{\alpha}\ddot{\mathbf{r}}^{\alpha} = \mathbf{f}^{\alpha}$ being the total force on atom α, Eq. (4.11) can be combined with Eq. (4.8) to get

$$\text{div}\boldsymbol{\sigma} = \sum_{\alpha} \mathbf{f}^{\alpha}\delta(\mathbf{r} - \mathbf{r}^{\alpha}). \tag{4.12}$$

Recall that the Fourier transform $\hat{F}(\mathbf{s})$ of a function $F(\mathbf{r})$ is defined as

$$\hat{F}(\mathbf{s}) = \int_V F(\mathbf{r})e^{\mathrm{i}\mathbf{s}\cdot\mathbf{r}}dV. \tag{4.13}$$

Following Shen and Atluri (2004), we take the Fourier transform of both sides of Eq. (4.12), and simplify the left-hand side of the resulting equation as follows.

$$\begin{aligned}
&\int_V (\nabla\cdot\boldsymbol{\sigma})e^{\mathrm{i}\mathbf{s}\cdot\mathbf{r}}dV \\
&= \int_V \left[\nabla\cdot\left(e^{\mathrm{i}\mathbf{s}\cdot\mathbf{r}}\boldsymbol{\sigma}\right) - \nabla\left(e^{\mathrm{i}\mathbf{s}\cdot\mathbf{r}}\right)\cdot\boldsymbol{\sigma}\right]dV, \\
&= \int_{\partial V} \mathbf{n}\cdot\left(e^{\mathrm{i}\mathbf{s}\cdot\mathbf{r}}\boldsymbol{\sigma}\right)da - \mathrm{i}\mathbf{s}\cdot\int_V \left(e^{\mathrm{i}\mathbf{s}\cdot\mathbf{r}}\boldsymbol{\sigma}\right)dV, \\
&= -\mathrm{i}\mathbf{s}\cdot\hat{\boldsymbol{\sigma}}.
\end{aligned} \tag{4.14}$$

For simplicity, we consider an infinite system here. But the derivation and conclusions apply to finite systems with external forces (Murdoch, 2007). Thus, the Fourier transform of Eq. (4.12) gives

$$
\begin{aligned}
\mathbf{is}\cdot\hat{\boldsymbol{\sigma}}(\mathbf{s}) &= -\sum_{\alpha}\mathbf{f}^{\alpha}e^{\mathbf{is}\cdot\mathbf{r}^{\alpha}} \\
&= -\sum_{\alpha}\sum_{\beta\neq\alpha}\mathbf{f}^{\alpha\beta}e^{\mathbf{is}\cdot\mathbf{r}^{\alpha}} \\
&= -\frac{1}{2}\sum_{\alpha}\sum_{\beta\neq\alpha}\left[\mathbf{f}^{\alpha\beta}e^{\mathbf{is}\cdot\mathbf{r}^{\alpha}} + \mathbf{f}^{\beta\alpha}e^{\mathbf{is}\cdot\mathbf{r}^{\beta}}\right] \\
&= \mathbf{is}\cdot\frac{1}{2}\sum_{\alpha}\sum_{\beta\neq\alpha}\mathbf{r}^{\alpha\beta}\otimes\mathbf{f}^{\alpha\beta}\frac{e^{\mathbf{is}\cdot\mathbf{r}^{\alpha}} - e^{\mathbf{is}\cdot\mathbf{r}^{\beta}}}{\mathbf{is}\cdot\mathbf{r}^{\beta\alpha}}
\end{aligned}
\quad , \tag{4.15}
$$

The inverse Fourier transform of Eq. (4.15) yields the expression given in Eq. (4.5) for the Cauchy stress.

Instead of the Dirac delta function $\delta(\mathbf{r}-\mathbf{r}^{\alpha})$, Shen and Atluri (2004) use the localization function $w\left(\left|\mathbf{r}^{\alpha}-\mathbf{r}\right|\right)$ in Eq. (4.12) and write it as

$$
\operatorname{div}\boldsymbol{\sigma} = \sum_{\alpha}\mathbf{f}^{\alpha}w\left(\left|\mathbf{r}^{\alpha}-\mathbf{r}\right|\right). \tag{4.16}
$$

The localization function $w\left(\left|\mathbf{r}^{\alpha}-\mathbf{r}\right|\right)$ is a smooth non-negative function of compact support with the maximum value at $\mathbf{r}=\mathbf{r}^{\alpha}$, decays with an increase in $\left|\mathbf{r}-\mathbf{r}^{\alpha}\right|$, and is normalized so that

$$
\int w\left(\left|\mathbf{r}^{\alpha}-\mathbf{r}\right|\right)d\mathbf{r} = 1\,. \tag{4.17}
$$

One can use the bond function $B^{\alpha\beta}(\mathbf{r})$ between atoms α and β introduced by Hardy (1982) to obtain the same expression for the Cauchy stress as that derived by Shen and Atluri (2004). The bond function is defined by

$$
B^{\alpha\beta}(\mathbf{r}) \equiv \int_0^1 w\left(\lambda\mathbf{r}^{\alpha\beta}+\mathbf{r}^{\alpha}-\mathbf{r}\right)d\lambda \tag{4.18}
$$

The value of $B^{\alpha\beta}(\mathbf{r})$ at any point equals the weighted fraction of the length between atoms α and β. Thus, it can be written as

$$
w\left(\left|\mathbf{r}^{\beta}-\mathbf{r}\right|\right) - w\left(\left|\mathbf{r}^{\alpha}-\mathbf{r}\right|\right) = -\mathbf{r}^{\alpha\beta}\cdot\nabla_{\mathbf{r}}B^{\alpha\beta}(\mathbf{r}) \tag{4.19}
$$

which can be obtained by integrating

$$
\frac{\partial w\left(\lambda\mathbf{r}^{\alpha\beta}+\mathbf{r}^{\alpha}-\mathbf{r}\right)}{\partial\lambda} = -\mathbf{r}^{\alpha\beta}\cdot\nabla_{\mathbf{r}}w\left(\lambda\mathbf{r}^{\alpha\beta}+\mathbf{r}^{\alpha}-\mathbf{r}\right), \tag{4.20}
$$

from $\lambda=0$ to 1. Since $\mathbf{f}^{\alpha\beta}=-\mathbf{f}^{\beta\alpha}$, Eq. (4.16) can be written as

$$
\begin{aligned}
\text{div}\boldsymbol{\sigma} &= \sum_{\alpha}\sum_{\beta}\mathbf{f}^{\alpha\beta}w\left(\left|\mathbf{r}^{\alpha}-\mathbf{r}\right|\right) \\
&= \frac{1}{2}\sum_{\alpha}\sum_{\beta}\mathbf{f}^{\alpha\beta}\left[w\left(\left|\mathbf{r}^{\alpha}-\mathbf{r}\right|\right)-w\left(\left|\mathbf{r}^{\beta}-\mathbf{r}\right|\right)\right] \\
&= \frac{1}{2}\sum_{\alpha}\sum_{\beta}\mathbf{f}^{\alpha\beta}\left[\mathbf{r}^{\alpha\beta}\cdot\nabla_{\mathbf{r}}B^{\alpha\beta}(\mathbf{r})\right]
\end{aligned}
\tag{4.21}
$$

Therefore

$$
\boldsymbol{\sigma} = \frac{1}{2}\sum_{\alpha}\sum_{\beta}\mathbf{f}^{\alpha\beta}\otimes\mathbf{r}^{\alpha\beta}B^{\alpha\beta}(\mathbf{r}). \tag{4.22}
$$

An interesting feature of the above derivation of the expression for the Cauchy stress tensor is that all six components of the Cauchy stress are obtained from three equations corresponding to the balance of linear momentum. Also, while simplifying expressions in Eq. (4.14) the divergence theorem is applied to an infinite region and its boundaries are taken to be traction free. The non-uniqueness of the derived expression for the Cauchy stress follows from the fact that any second order symmetric tensor with zero divergence and resulting in null tractions on boundaries of an infinite region can be added to the left-hand side of Eq. (4.12) without affecting any of the other steps used in deducing the expression.

Here we use the principle of virtual work and the balance of internal energy to derive an expression for the Cauchy stress tensor. For the sake of simplicity, we neglect body forces. Using Cauchy's cut principle we consider a part of the body comprised of only interior atoms as shown in Figure 4.1(a); the corresponding ECS is exhibited in Figure 4.1 (b). The action of the rest of the body on that interior to the boundaries of the cut region is represented by tractions on the bounding surface of the cut region.

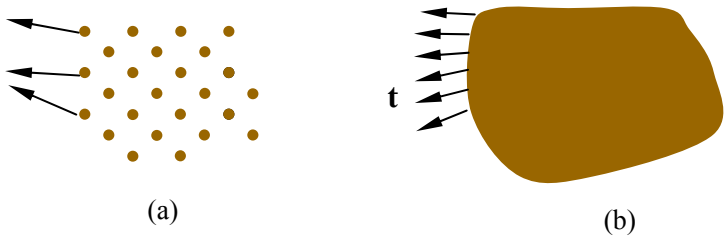

Figure 4.1 (a) Cut off region of an atomic system; (b) ECS with tractions on the bonding surface.

Corresponding to the virtual displacements $\delta\mathbf{r}^\alpha$ of atom α in the atomic system, we represent the corresponding virtual displacement field in the ECS by $\delta\mathbf{r}$. Then, according to the principle of virtual work, we have

$$\delta\int_V \rho e dV = \int_{\partial V} t_i \delta r_i da, \tag{4.23}$$

where e is the specific internal energy. The Reynolds transport theorem gives

$$\begin{aligned}\delta\int_V \rho e dV &= \int_V (\rho\delta e) dV \\ &= \int_V [\delta(\rho e) - e\delta\rho] dV \\ &= \int_V [\delta(\rho e) + \rho e(\delta r_i)_{,i}] dV\end{aligned} \tag{4.24}$$

Using the divergence theorem to simplify the term on the right-hand side of Eq. (4.23), we obtain

$$\int_{\partial V} t_i \delta r_i da = \int_{\partial V} \sigma_{ij} n_j \delta r_i da = \int_V (\sigma_{ij}\delta r_i)_{,j} dV. \tag{4.25}$$

Substituting from Eqs. (4.24) and (4.25) into Eq. (4.23) and requiring that it hold for every choice of the volume V, we obtain

$$\delta(\rho e) + \rho e(\delta r_i)_{,i} = (\sigma_{ij}\delta r_i)_{,j}. \tag{4.26}$$

We smoothen the inter-atomic potential ϕ^α by multiplying it with a smoothing kernel function $w(|\mathbf{r}^\alpha - \mathbf{r}|)$ and define the internal energy density, ρe, of the ECS by

$$\rho e = \sum_\alpha \phi^\alpha w(|\mathbf{r}^\alpha - \mathbf{r}|), \tag{4.27}$$

where

$$\phi^\alpha = \frac{1}{2}\sum_{\beta\neq\alpha} \phi^{\alpha\beta}(r^{\alpha\beta}), \tag{4.28}$$

for pair-wise potentials such as that obtained by the EAM; hereafter it is called the EAM potential. We note that values of ϕ^α and $w(|\mathbf{r}^\alpha - \mathbf{r}|)$ are invariant with respect to rigid body displacements superimposed on the MM system. Thus values of ρe, and hence e are also unchanged under superimposed rigid body displacements since the mass density is unaffected by these displacements.

It follows from Eq. (4.27) that

$$
\begin{aligned}
&\delta(\rho e)+\rho e(\delta r_i)_{,i} \\
&=\delta\sum_\alpha \phi^\alpha w\left(\left|\mathbf{r}^\alpha-\mathbf{r}\right|\right)+\sum_\alpha \phi^\alpha w\left(\left|\mathbf{r}^\alpha-\mathbf{r}\right|\right)(\delta r_i)_{,i} \\
&=\frac{1}{2}\sum_\alpha\sum_\beta \frac{\partial\phi^{\alpha\beta}}{\partial r^{\alpha\beta}}\frac{r_i^{\alpha\beta}}{r^{\alpha\beta}}\delta r_i^{\alpha\beta} w\left(\left|\mathbf{r}^\alpha-\mathbf{r}\right|\right)-\sum_\alpha \phi^\alpha\nabla_{\mathbf{r}}\left(w\left(\left|\mathbf{r}^\alpha-\mathbf{r}\right|\right)\right)\cdot\delta\mathbf{r}^\alpha \\
&+\sum_\alpha \phi^\alpha\nabla_{\mathbf{r}}\left(w\left(\left|\mathbf{r}^\alpha-\mathbf{r}\right|\right)\right)\cdot\delta\mathbf{r}+\sum_\alpha \phi^\alpha w\left(\left|\mathbf{r}^\alpha-\mathbf{r}\right|\right)\nabla_{\mathbf{r}}(\delta\mathbf{r}) \\
&=\frac{1}{2}\sum_\alpha\sum_\beta f_i^{\alpha\beta}\left(\delta r_i^\beta-\delta r_i^\alpha\right)w\left(\left|\mathbf{r}^\alpha-\mathbf{r}\right|\right)-\nabla_{\mathbf{r}}\cdot\sum_\alpha \phi^\alpha\left(w\left(\left|\mathbf{r}^\alpha-\mathbf{r}\right|\right)\delta\mathbf{r}^\alpha\right) \\
&+\nabla_{\mathbf{r}}\cdot\sum_\alpha \phi^\alpha w\left(\left|\mathbf{r}^\alpha-\mathbf{r}\right|\right)\delta\mathbf{r}
\end{aligned}
\tag{4.29}
$$

For a MM system, $\sum_\beta \mathbf{f}^{\alpha\beta}=\mathbf{0}$. Therefore,

$$
\sum_\alpha\sum_\beta f_i^{\alpha\beta}\delta r_i^\alpha w\left(\left|\mathbf{r}^\alpha-\mathbf{r}\right|\right)=0\text{,} \tag{4.30}
$$

and

$$
\begin{aligned}
&\frac{1}{2}\sum_\alpha\sum_\beta f^{\alpha\beta}\left(\delta r_i^\beta-\delta r_i^\alpha\right)w\left(\mathbf{r}^\alpha-\mathbf{r}\right) \\
&=\frac{1}{2}\sum_\alpha\sum_\beta f^{\alpha\beta}\left(\delta r_i^\beta+\delta r_i^\alpha\right)w\left(\mathbf{r}^\alpha-\mathbf{r}\right) \\
&=\frac{1}{2}\sum_\alpha\sum_\beta f^{\beta\alpha}\delta r_i^\alpha w\left(\mathbf{r}^\beta-\mathbf{r}\right)+\frac{1}{2}\sum_\alpha\sum_\beta f^{\alpha\beta}\delta r_i^\alpha w\left(\mathbf{r}^\alpha-\mathbf{r}\right) \\
&=\frac{1}{2}\sum_\alpha\sum_\beta f^{\alpha\beta}\delta r_i^\alpha\left[w\left(\mathbf{r}^\alpha-\mathbf{r}\right)-w\left(\mathbf{r}^\beta-\mathbf{r}\right)\right] \\
&=\frac{1}{2}\sum_\alpha\sum_\beta (\mathbf{f}^{\alpha\beta}\cdot\delta\mathbf{r}^\alpha)\left[\mathbf{r}^{\alpha\beta}\cdot\nabla_{\mathbf{r}}B^{\alpha\beta}(\mathbf{r})\right]
\end{aligned}
\tag{4.31}
$$

Hence

$$
\delta(\rho e)+\rho e(\delta x_i)_{,i}=\frac{1}{2}\sum_\alpha\sum_\beta (\mathbf{f}^{\alpha\beta}\cdot\delta\mathbf{r}^\alpha)\left[\mathbf{r}^{\alpha\beta}\cdot\nabla_{\mathbf{r}}B^{\alpha\beta}(\mathbf{r})\right]+\nabla_{\mathbf{r}}\cdot\sum_\alpha \phi^\alpha w\left(\left|\mathbf{r}^\alpha-\mathbf{r}\right|\right)\left(\delta\mathbf{r}-\delta\mathbf{r}^\alpha\right) \tag{4.32}
$$

By using three virtual displacements corresponding to rigid body rotations about the x_1-, the x_2- and the x_3- axes, we get equations that imply the symmetry of the Cauchy stress tensor. Three virtual displacements corresponding to translations along the x_1-, the x_2- and the x_3- axes give three equations for finding the six components of the Cauchy stress tensor. We propose that the remaining three equations be obtained by considering a parallelepiped with bounding surfaces parallel to the three coordinate

planes both in the MM system and in the ECS, and equating the work done by surface tractions during any virtual displacement. However, this is left for future study.

Here we choose the localization function w to be the Gaussian function

$$w(|\mathbf{x}|) = \begin{cases} \dfrac{1}{(\sqrt{\pi}h)^d} \exp\left(-\dfrac{|\mathbf{x}|^2}{h^2}\right) & |\mathbf{x}| \le r_w \\ 0 & |\mathbf{x}| \le r_w, \end{cases} \tag{4.33}$$

where d = 1, 2 and 3 respectively for 1D, 2D and 3D problems, and h is the smoothing length. As $h \to 0$, the localization function approaches the Dirac function $\delta(\mathbf{x})$ and Eq. (4.22) becomes Eq. (4.5). Based on results of numerical experiments Shen and Atluri (2004) have recommended that $h = 2a_0$ where a_0 is the length of lattice vector.

4.3 Equivalent strain for a MM system

We now find the deformation gradient $\mathbf{F}^\alpha$ at the point in the ECS that corresponds to the atomic position α in the MM system. The continuum relation

$$\Omega^\alpha = J\Omega_0^\alpha \tag{4.34}$$

relates the present volume Ω^α to the volume Ω_0^α associated with atom α in the reference (undeformed) configuration. The volume Ω_0^α equals the total volume of the MM system divided by the number of atoms. In Eq. (4.34) the Jacobian $J^\alpha = \det \mathbf{F}^\alpha$.

We use the Cauchy-Born rule to define the deformation gradient $\mathbf{F}^\alpha$ through the relation

$$\mathbf{r}^{\alpha\beta} = \mathbf{F}^\alpha \mathbf{R}^{\alpha\beta} \tag{4.35}$$

where atom β is adjacent to atom α, and $\mathbf{R}^{\alpha\beta} = \mathbf{R}^\beta - \mathbf{R}^\alpha$ is the vector between atoms α and β in the undeformed configuration. The method of least squares is used to find $\mathbf{F}^\alpha$, i.e., we minimize the function Λ defined by

$$\Lambda = \sum_{\beta} \left| \mathbf{r}^{\alpha\beta} - \mathbf{F}^{\alpha} \mathbf{R}^{\alpha\beta} \right|^2 = \sum_{i=1}^{3} \sum_{\beta} \left(r_i^{\alpha\beta} - F_{ik}^{\alpha} R_k^{\alpha\beta} \right)^2, \quad i, j, k = 1,2,3. \tag{4.36}$$

We set

$$\frac{\partial \Lambda}{\partial F_{ij}^{\alpha}} = \sum_{\beta} 2\left(r_i^{\alpha\beta} - F_{ik}^{\alpha} R_k^{\alpha\beta} \right) R_j^{\alpha\beta} = 0, \tag{4.37}$$

to obtain a system of nine simultaneous equations whose solution is

$$F_{ij}^{\alpha} = \frac{\Delta_{ij}^{\alpha}}{\Delta^{\alpha}}, \tag{4.38}$$

where

$$\Delta^{\alpha} = \begin{vmatrix} \sum_{\beta} R_1^{\alpha\beta} R_1^{\alpha\beta} & \sum_{\beta} R_1^{\alpha\beta} R_2^{\alpha\beta} & \sum_{\beta} R_1^{\alpha\beta} R_3^{\alpha\beta} \\ \sum_{\beta} R_2^{\alpha\beta} R_1^{\alpha\beta} & \sum_{\beta} R_2^{\alpha\beta} R_2^{\alpha\beta} & \sum_{\beta} R_2^{\alpha\beta} R_3^{\alpha\beta} \\ \sum_{\beta} R_3^{\alpha\beta} R_1^{\alpha\beta} & \sum_{\beta} R_3^{\alpha\beta} R_2^{\alpha\beta} & \sum_{\beta} R_3^{\alpha\beta} R_3^{\alpha\beta} \end{vmatrix}, \tag{4.39}$$

and Δ_{ij}^{α} is calculated by replacing the j^{th} column of Δ with the vector $\left[\sum_{\beta} r_i^{\alpha\beta} R_1^{\alpha\beta} \quad \sum_{\beta} r_i^{\alpha\beta} R_2^{\alpha\beta} \quad \sum_{\beta} r_i^{\alpha\beta} R_3^{\alpha\beta} \right]^{\mathrm{T}}$.

With $\mathbf{F}^{\alpha}$ and $\boldsymbol{\sigma}^{\alpha}$ known, we can compute other stress and strain tensors by using continuum mechanics relations amongst them.

Assuming that dislocations initiate where the deformation is highly heterogeneous, i.e., values of one or more components of $\mathbf{F}^{\alpha}$ are locally very large as compared to those at neighboring points we determine sites where dislocations initiate. Accordingly, we introduce an inhomogeneity parameter, Γ, by the following expression:

$$\Gamma^{\alpha} = \frac{\sum_{\beta} \left| \mathbf{r}^{\alpha\beta} - \mathbf{F}^{\alpha} \mathbf{R}^{\alpha\beta} \right|}{\sum_{\beta} \left| \mathbf{R}^{\alpha\beta} \right|}. \tag{4.40}$$

We note that the definition of Γ is independent of the lattice structure, and hence is

applicable to FCC, BCC and HPC lattices and even an amorphous structure. However, the centro-symmetry parameter (Kelchner et al., 1998) is first used to indicate the onset of dislocations is applicable to an FCC system, and needs modification when applied to other lattices. Furthermore, it cannot be applied to amorphous materials.

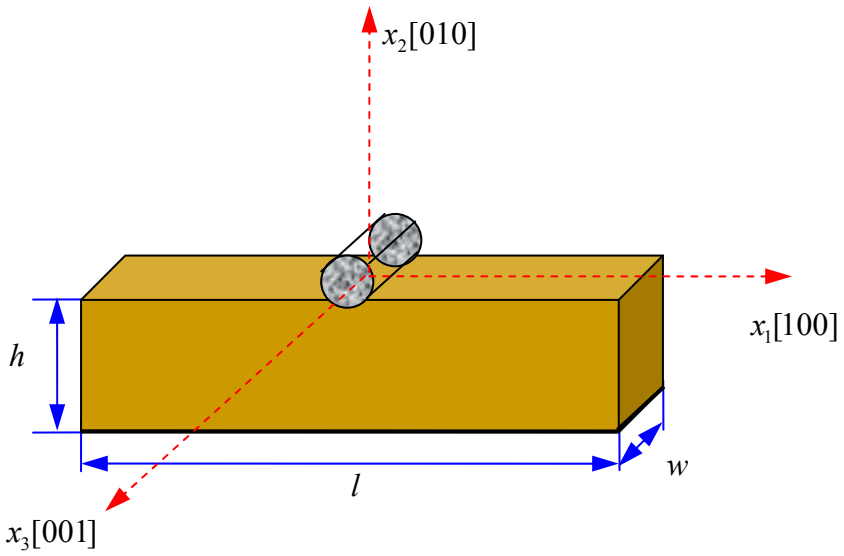

Figure 4.2 Schematic sketch of the problem studied.

4.4 Molecular Mechanics (MM) simulations of plane strain nanoindentation

A schematic sketch of the problem studied is shown in Figure 4.2. A 3-D gold lattice with dimensions $l \times h \times w$ is indented by a rigid circular cylinder. As shown in Figure 4.2, the x_1-, the x_2- and the x_3- axes are aligned along the [001], [010] and [001] directions, respectively. The rigid circular cylinder with the centroidal axis along the x_3- axis is pressed on the gold lattice in the x_2- direction. We use the freely available software LAMMPS (Large-scale Atomic/Molecular Massively Parallel Simulator (Plimpton, 1995; Plimpton et al., 1997)) to conduct MM simulations of the indentation of the gold lattice by a rigid cylinder. The problem is idealized as 2-D by applying periodic boundary conditions on the boundary planes perpendicular to the

x_3-axis. Non-periodic and shrink-wrapped boundaries are used for the x_1- and the x_2- bounding planes. Thus the vertical left and right bounding surfaces of the gold lattice, and the top surface except for the area contacting the rigid cylinder, are taken to be traction free. Atoms on the bottom 4 layers of the lattice are fixed; thus the effective thickness of the sample is less than *h*. When comparing results of the MM simulations with those of the corresponding continuum problems, we assume that the thickness of the continuous body equals the effective thickness of the gold lattice specimen, i.e. equals *h* minus the thickness of atomic layers in which atoms are not allowed to move. Furthermore, the continuous body is regarded as linear elastic, homogeneous and anisotropic with cubic symmetry. It is perfectly bonded to a rigid substrate and indented by a rigid circular cylinder with the assumption that lengths of the cylinder and the layer in the x_3- direction (perpendicular to the plane of the paper) are very large as compared to dimensions of the layer within the plane of the paper. Thus a plane strain state of deformation exists in the continuous body.

When studying indentation into the gold crystal, the rigid indenter is moved into the specimen in 0.1 Å increments, and the potential energy of the system is minimized after every incremental displacement. Since it is difficult to simulate the displacement boundary conditions between the indenter and the sample, we apply point forces to atoms on the contact surface. The force is given by

$$\mathbf{f}^{\alpha c} = \begin{cases} k(R - r^{\alpha})^2 \dfrac{\mathbf{r}^{\alpha}}{r^{\alpha}}, & r^{\alpha} \le R, \\ 0, & r^{\alpha} > R, \end{cases} \tag{4.41}$$

where k is a constant related to the stiffness of the indenter, R the radius of the indenter, and $\mathbf{r}^{\alpha}$ the vector between the indenter center and the α^{th} atom. We set k=100eV/ Å^3, which ensures that the indenter is essentially rigid, and take R=100Å. Once the potential energy has been minimized, we check if all atoms on the contact surface are within prescribed tolerances of the profile of the rigid circular indenter. The force $\mathbf{f}^{\alpha c}$ on each atom lying on the contact surface is adjusted till such is the case. Once the solution has converged, we sum axial components of $\mathbf{f}^{\alpha c}$ acting on

all atoms of the contact surface, call it the indentation load, and plot the load versus indentation curves.

(a)

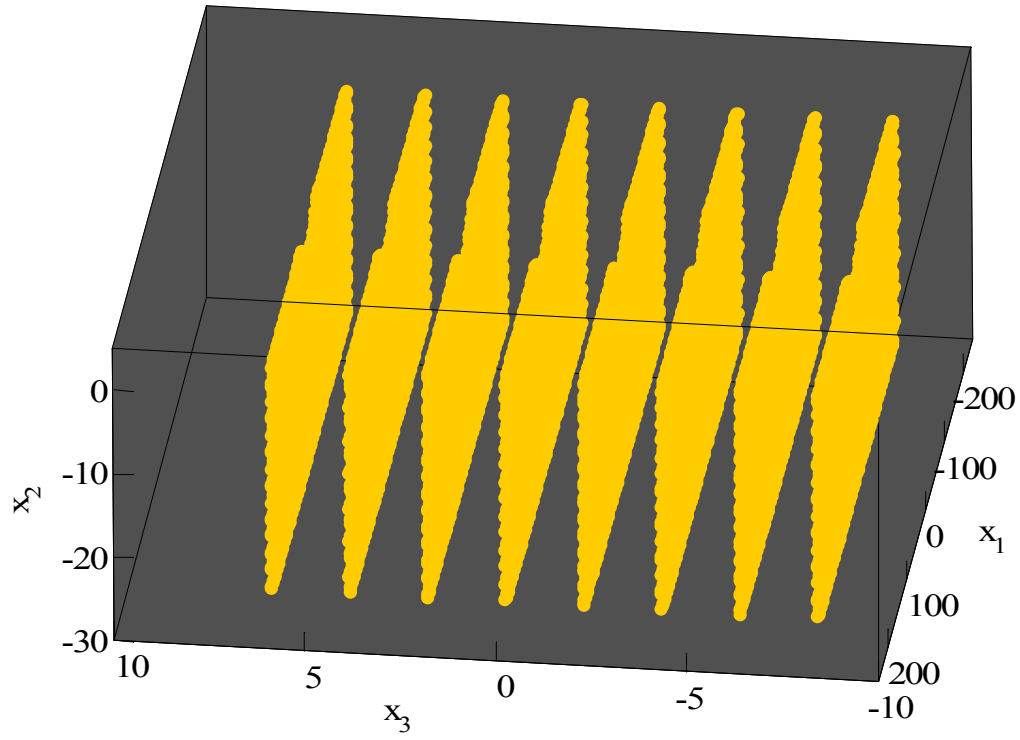

(b)

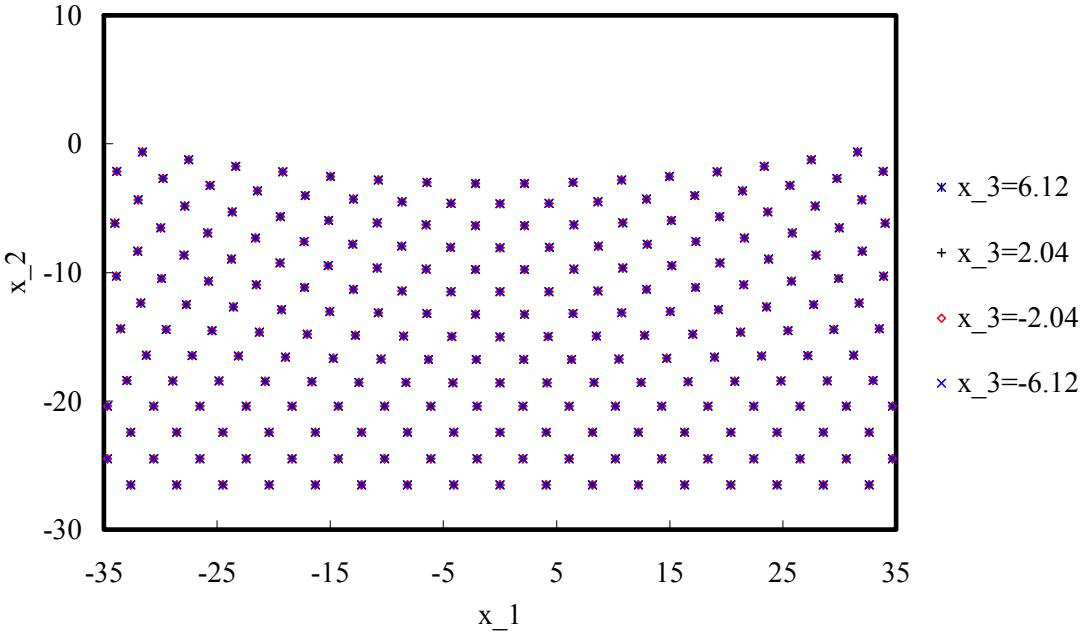

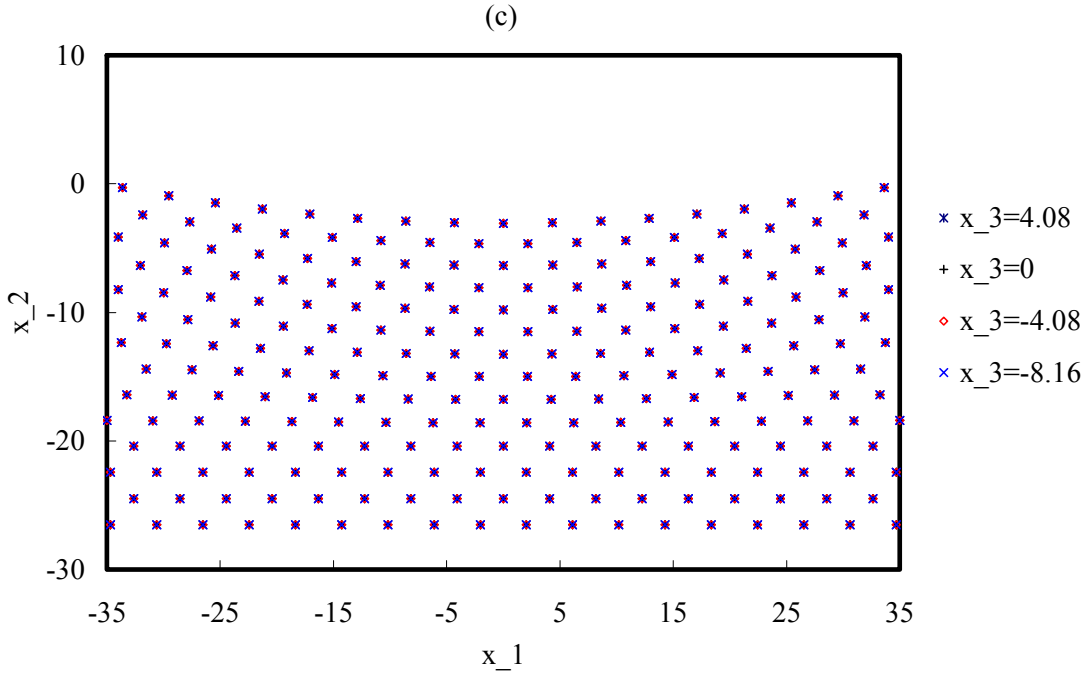

Figure 4.3 (a) 3D configuration; (b) 2D configurations of x_3 = 6.12, 2.04, -2.04, 6.12 Angstrom; (c) 2D configurations of planes x_3 = 4.08, 0, -4.08, -8.16 Angstrom for indentation depth of 3 Angstrom. (l = 408, h = 26.52, w = 16.32, Units: Angstrom)

Equivalence of periodic boundary conditions and plane deformation

The imposition of periodic boundary conditions on the x_3 bounding planes implies that atoms interact with each other across these boundaries, they can exit from one end surface of the domain of study and re-enter through the other end surface of the domain. As can be seen from results plotted in Figure 4.3(a), atoms inside the domain do not move in the x_3 - direction, and atoms in different layers have same displacements as is shown in Figure 4.3(b), (c). Thus, deformations of the body correspond to that of plane strain, and we will only plot stress distributions within one layer and compare those to the corresponding results from indentation tests on a continuous body.

EAM potential

Interactions among atoms are modeled by the EAM potentials (Foiles et al., 1986).

The EAM assumes that the density of the electron gas can be approximated by the sum of electron densities from surrounding atoms, and adds a repulsive term to account for the core-core interactions. The total binding energy of a collection of atoms is given by the sum of energies for each atom. That is,

$$E^b = \sum_\alpha E^\alpha \,, \tag{4.42}$$

$$E^\alpha = \frac{1}{2}\sum_\beta \phi(r^{\alpha\beta}) + F'\left(\sum_\beta \rho'(r^{\alpha\beta})\right). \tag{4.43}$$

The function $\phi(r^{\alpha\beta})$ represents the core-core repulsion, F' is the embedding function, and $\rho'(r^{\alpha\beta})$ is the contribution to the electron density at the site of atom α from the atom β.

As derived in Chapter 3, there is a linear relation between $\ln\sqrt{P}$ and $\pi u_0 / P$ for 2D indentation of a half space, where u_0 and P are the indentation depth and the contact load respectively. The slope of $\ln\sqrt{P}$ and $\pi u_0 / P$ is $-1/\beta$, which depends on material properties as described by Eq. (3.24.1) in Chapter 3; the value of $-1/\beta$ can be found from Eq. (3.24.1) and values of material elasticities listed below (Lilleodden et al., 2003).

$$C_{11} = 183\text{GPa}\,,\ \ C_{12} = 154\text{GPa}\,,\ \ C_{44} = 45\text{GPa} \tag{4.45}$$

For the gold crystal being studied, the ideal value of $-1/\beta$ should be -40.0GPa. From results of the indentation test on the MM system plotted in Figure 4.4(a), we find $-1/\beta$ to equal -39.6GPa. This agrees well with the expected value of -40.0GPa.

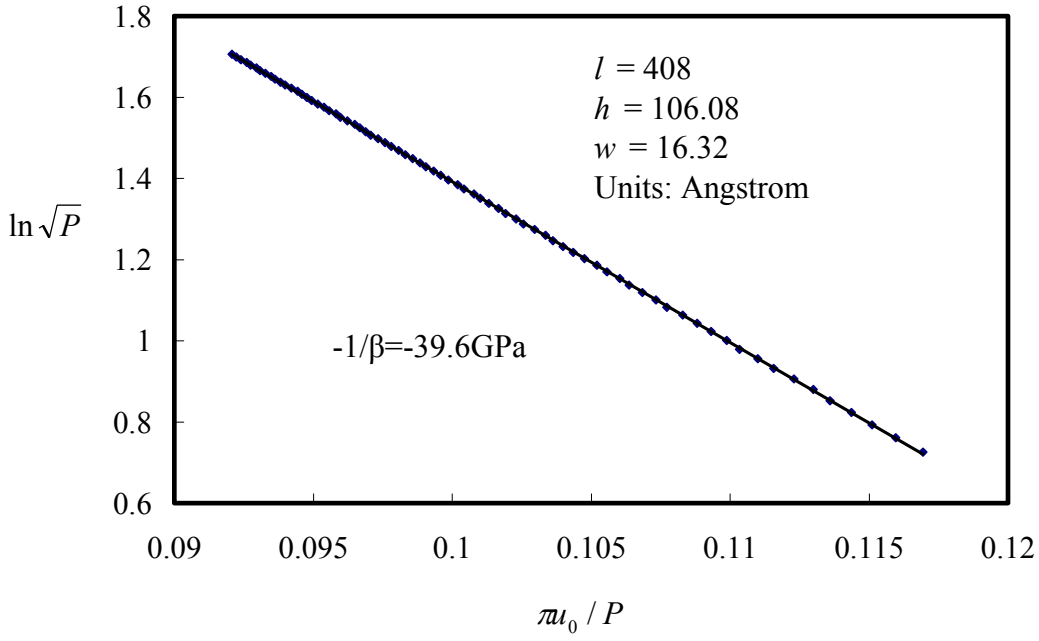
1.8
1.6
1.4
1.2
1
0.8
0.6
$\ln\sqrt{P}$
l = 408
h = 106.08
w = 16.32
Units: Angstrom
-1/β=-39.6GPa
0.09
0.095
0.1
0.105
0.11
0.115
0.12
$\pi\mu_0 / P$

(a)

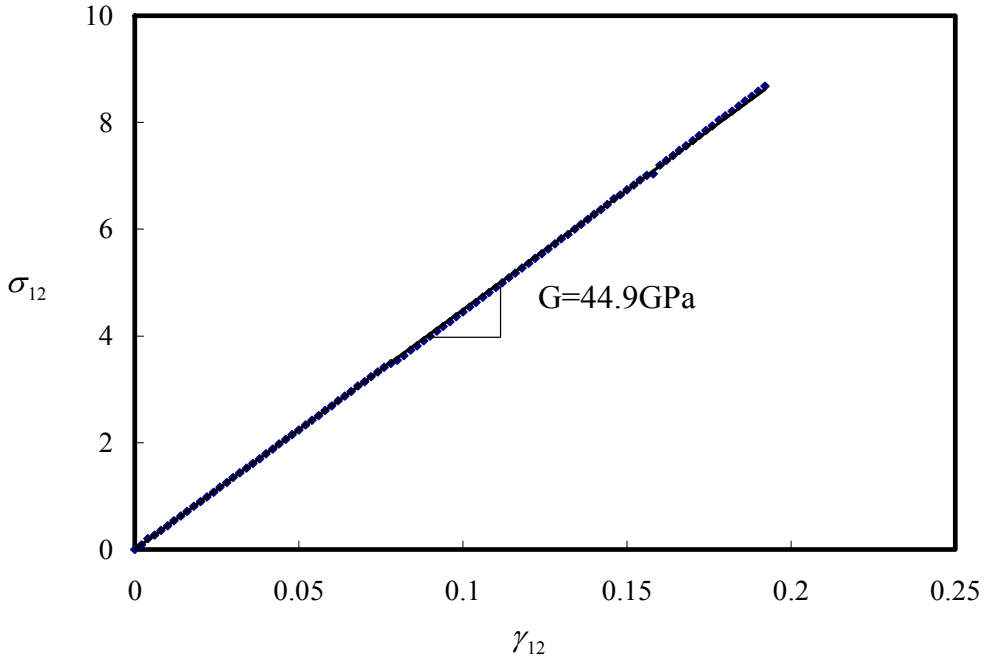
10
8
6
4
2
0
σ_{12}
G=44.9GPa
0
0.05
0.1
0.15
0.2
0.25
γ_{12}

(b)

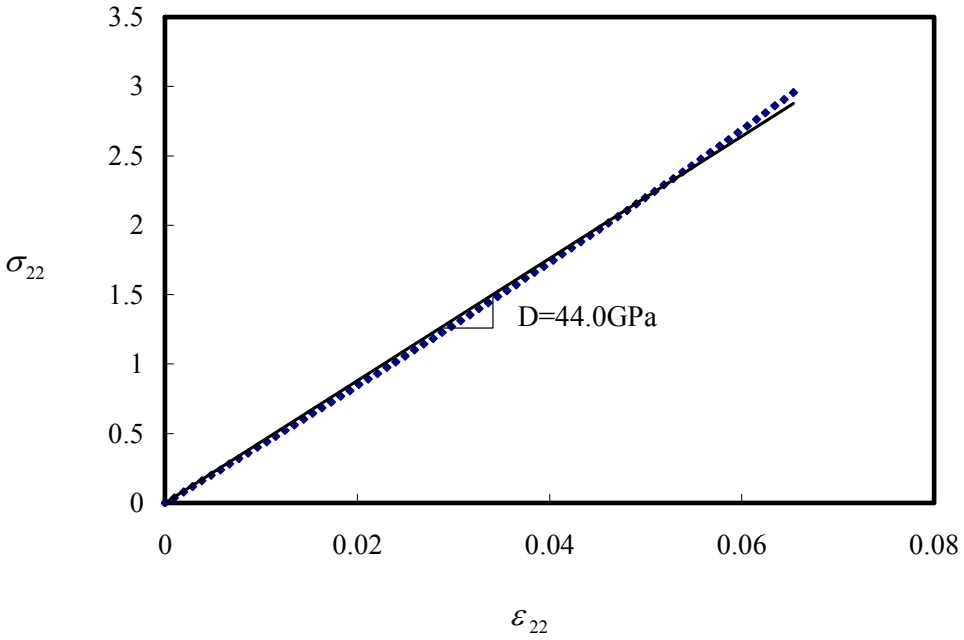

(c)

Figure 4.4 Plots of load vs. displacement curves; (a) $\ln\sqrt{P}$ vs. $\pi u_0 / P$ for MM simulations of the nanoindentation; (b) σ_{12} vs. γ_{12} for the simple shear test; and (c) σ_{22} vs. ε_{22} for the plane strain compression test.

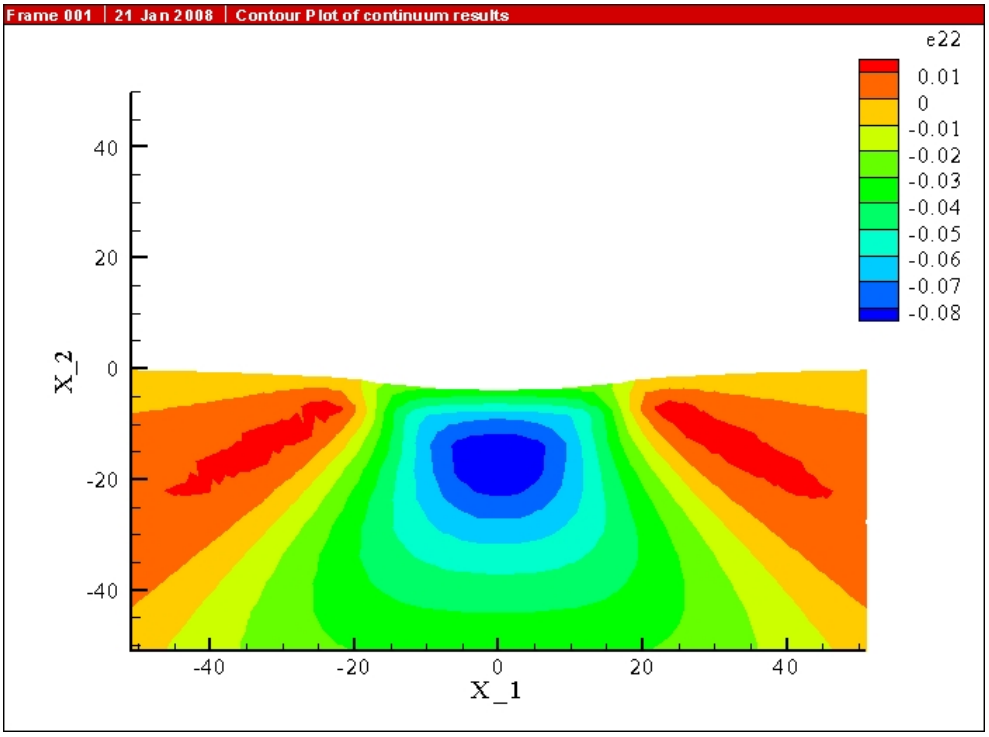

(a)

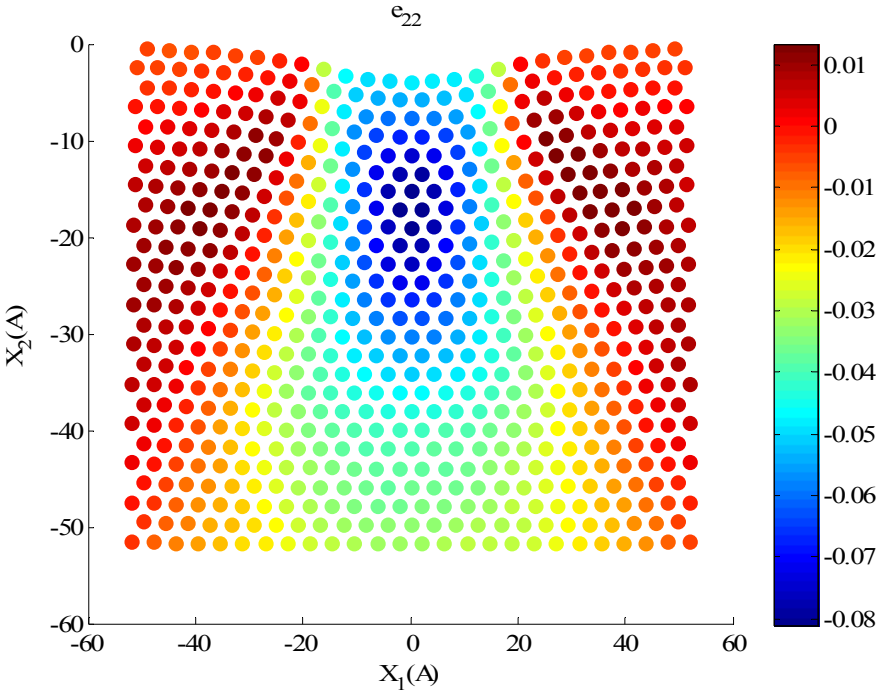

(b)

Figure 4.5 Plot of ε_{22} in the vicinity of the indentation area: (a) continuum level simulations; (b) atomic level simulations.

For the indentation depth of 3.9 Angstrom, Figure 4.5a, b exhibits the variation of the axial strain ε_{22} at points in the immediate vicinity of the indented area. Results from the atomic and the continuum simulations are in qualitative agreement with each other. In each case the maximum magnitude, 0.08, of ε_{22} occurs at a point that is on the axis of symmetry and is below the contact surface.

The distribution of the axial stress, σ_{22}, in the region near the contact surface obtained by the continuum and the atomic simulations is exhibited in Figure 4.6a,b. At points away from the contact surface, the two stress distributions agree with each other qualitatively but at points close to the contact surface the agreement between the two is not that good. The satisfaction of traction free boundary conditions in MM simulations is a challenge (Tsai, 1979; Cheung and Yip, 1991; Park et al., 2006), and is being currently pursued by several investigators.

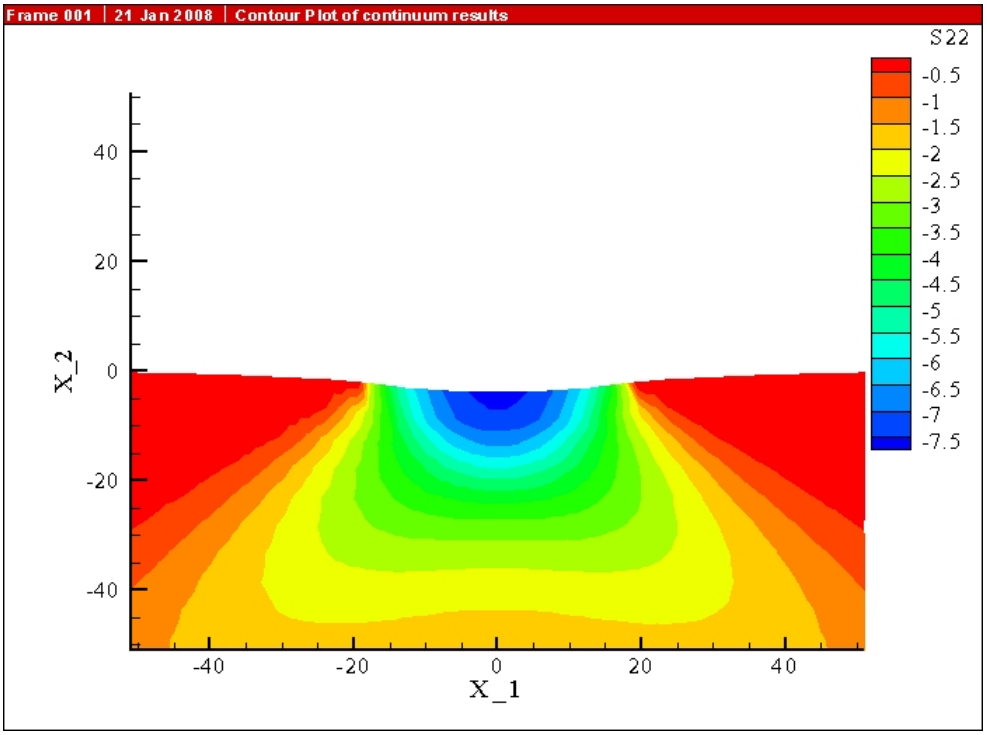

(a)

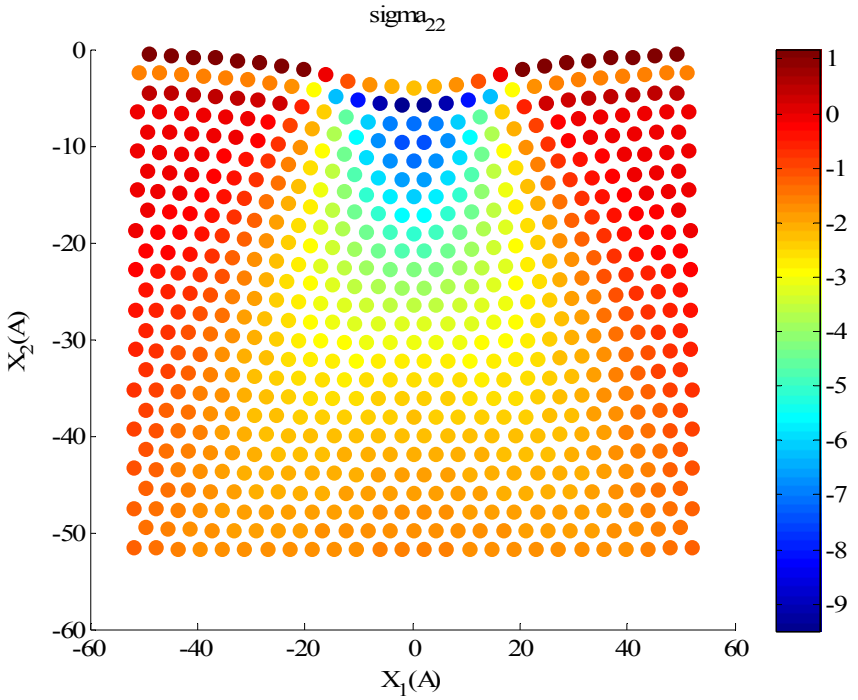

(b)

Figure 4.6 Variation of the axial stress, σ_{22}, in the region adjoining the contact surface, (a) continuum simulations, and (b) MM simulations (units: GPa).

Comaprison of results from the centrosymmetry parameter and the inhomogeneity parameter Γ

In Figure 4.7a, we have plotted load-displacement curve of 2D MM simulation of nanoindentation of a gold lattice. The load drop in that picture indicates the initiation of dislocations, or large inhomogeneous deformation. In Figure 4.7b, c, we have plotted the variations of the inhomogeneity parameter Γ right before and after the initiation of dislocations. It is clear that the inhomogeneity parameter Γ has a relatively higher value in the region with large inhomogeneous deformations than that in the homogeneously deformed region.

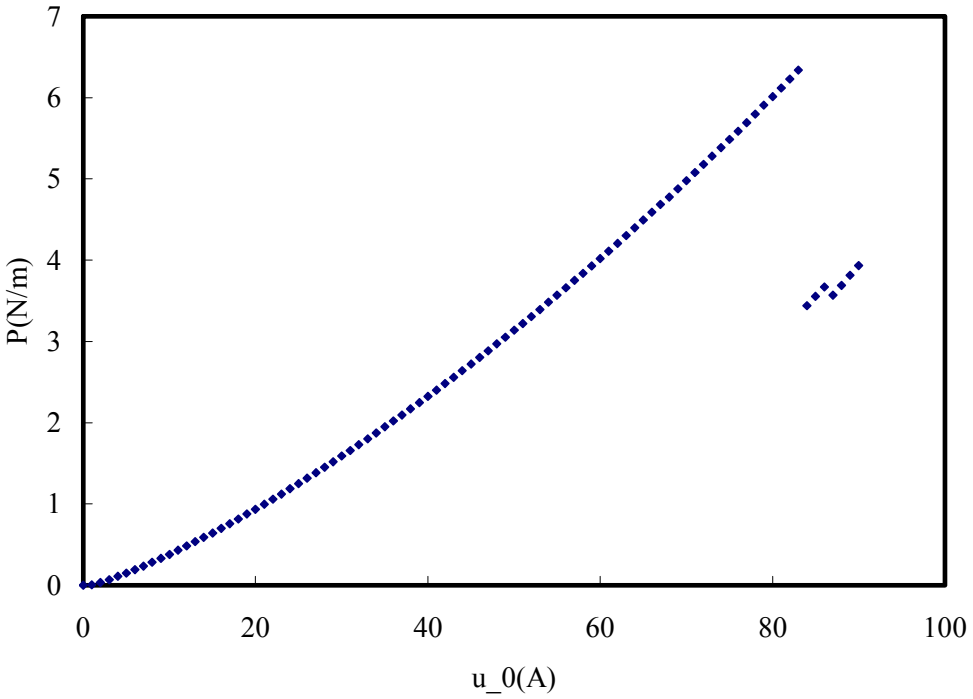

(a)

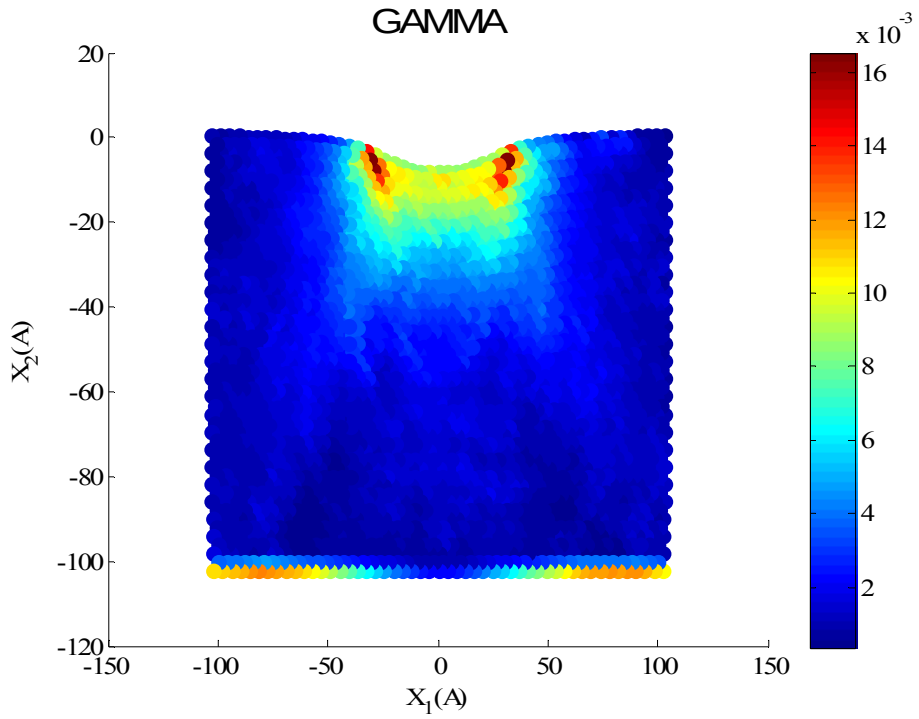
GAMMA
x 10^-3
16
14
12
10
8
6
4
2
20
0
-20
-40
-60
-80
-100
-120
-150
-100
-50
0
50
100
150
X2(A)
X1(A)

(b)

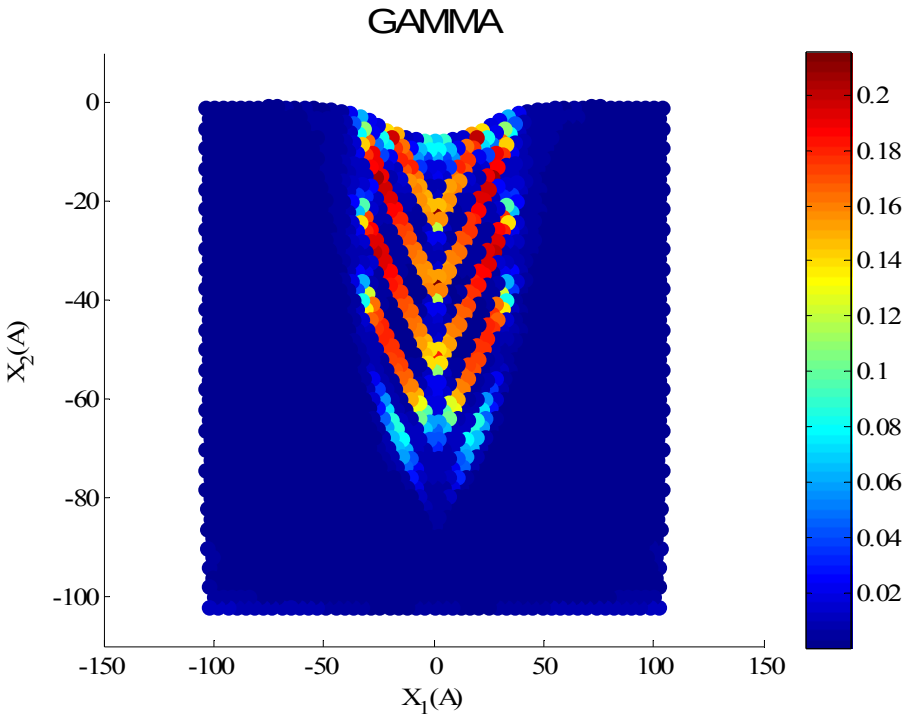
GAMMA
0.2
0.18
0.16
0.14
0.12
0.1
0.08
0.06
0.04
0.02
0
-20
-40
-60
-80
-100
-150
-100
-50
0
50
100
150
X2(A)
X1(A)

(c)

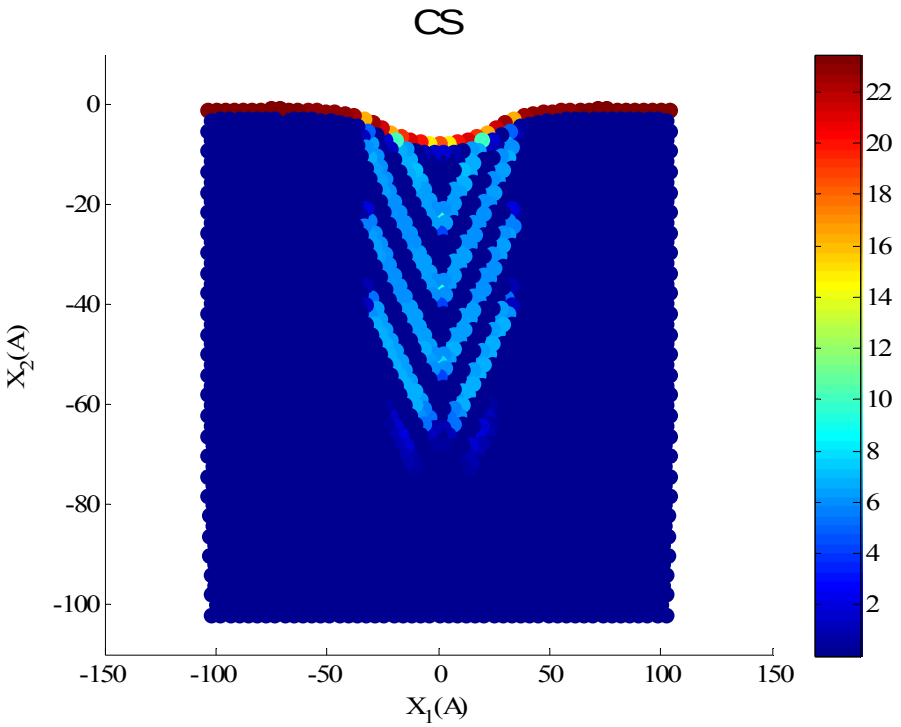

(d)

Figure 4.7 (a) Load-displacement curve of 2D MM simulations of indentation into the gold lattice; Variation in the region close to the contact surface of (b) the inhomogeneity parameter Γ before the initiation of dislocations; (c) the inhomogeneity parameter Γ just after the initiation of dislocations; and (d) centrosymmetry parameter just after the initiation of dislocations.

In Figure 4.7c,d, we have compared the variations of the inhomogeneity parameter Γ and the centrosymmetry parameter (Kelchner et al, 1998) often used in the literature to identify the onset of dislocations. It is clear that the two plots agree qualitatively in the sense that high values of the centrosymmetric and the inhomogeneity parameters occur at the same points except that the centrosymmetric parameter has high values at points on the free surface but the inhomogeneity parameter does not. The MM simulations of other tests are needed to confirm the validity of using Γ as an indicator for the initiation of dislocations. We note that whereas Γ can be easily computed for MM simulations of BCC and HCP crystals and even amorphous structures, the centrosymmetric parameter was developed for FCC lattice (Kelchner et al, 1998) and needs modifications to be applied to study the onset of dislocations in other lattices. Furthermore, the centrosymmetric parameter is hard to apply to amorphous structures.

Plane strain simple shear and simple compression tests

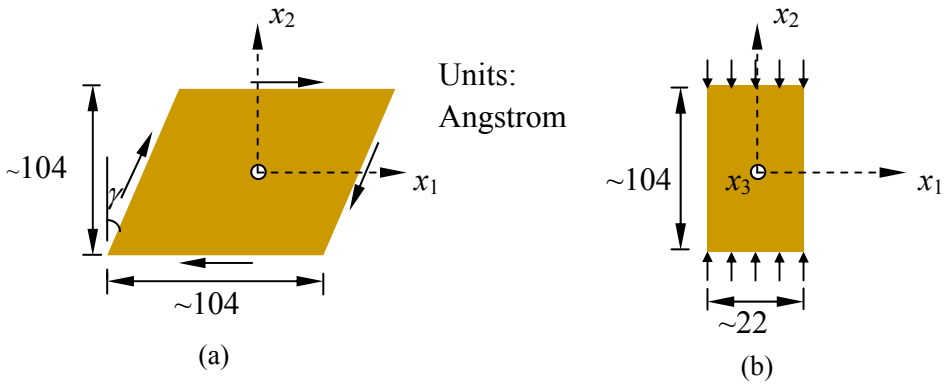

Figure 4.8 Schematics of 2D MM simulations of (a) simple shear, and (b) simple compression tests.

Figure 4.8 (a), (b) depicts schematics of configurations and boundary conditions used for MM simulations of the simple shear and the simple compressive deformations of a gold crystal. In MM simulations for simple shearing, displacements in both the x_1 - and the x_2 – directions of atoms in the outer three layers are prescribed. The positions (x_1', x_2') of atoms in the deformed configurations of the three bounding layers are related to their co-ordinates (x_1, x_2) in the undeformed configurations by

$$x_1^{\alpha'} = x_1^{\alpha} + x_2^{\alpha} \tan\gamma\,, \qquad x_2^{\alpha'} = x_2^{\alpha}\,. \tag{4.44}$$

Here γ is the shear angle. During MM simulations, the shear angle is increased in increments of 0.002, and the potential energy of the system is minimized.

For the simple compression test, atoms in the bottom three layers are fixed, those in the top three layers are displaced downward as a rigid body in increments of 0.1Å, and then the potential energy of the system is minimized.

According to Hooke's law applicable for infinitesimal deformations of an elastic body, the shear stress σ_{12} is related to the shear strain γ_{12} by

$$\sigma_{12} = G_{12}\gamma_{12}\,, \tag{4.46}$$

where $G_{12} = 45\text{GPa}$ is the shear modulus in the x_1x_2 - plane. In MM simulations, we calculate the shear stress by using the total shear force acting on the interface between

the top three layers and the inner layers, and the area A of the cross-section in the x_1x_3-plane. The shear strain is given by $\gamma_{12} = \tan\gamma$. From results of the MM simulations plotted in Figure 4.4 (b) we get G_{12} (the slope of the shear stress versus the shear strain curve) equal to 44.9GPa which differs from the ideal value of 45 GPa by 0.2%.

For plane strain deformations in the x_1x_2- plane due to an axial stress σ_{22}, Hooke's law gives the following relation between σ_{22} and the axial compressive strain ε_{22}:

$$\sigma_{22} = E\varepsilon_{22}, \tag{4.47}$$

where

$$E = C_{11} - \frac{C_{12}^2}{C_{11}} = 44.9\text{GPa}. \tag{4.48}$$

In MM simulations, the axial stress σ_{22} is calculated by first finding the total axial force at the interface between the top three layers and the remaining adjacent layers, and then dividing it by the area of cross-section. The average axial strain ε_{22} is found from

$$\varepsilon_{22} = \frac{l - l_0}{l_0}, \tag{4.49}$$

where l and l_0 equal, respectively, effective lengths in the x_2- direction of the specimen in the undeformed and the deformed configurations. We conclude from results plotted in Figure 4.4(c) that $E = 44.0\text{GPa}$ which deviates from the ideal value of 44.9GPa by 2%.

4.5 Conclusions

We have reviewed the commonly used technique to derive a relation between the Cauchy stress tensor defined at the continuum level and the interatomic forces derived from a molecular mechanics potential. By adopting the classical approach of using the Cauchy-Born rule and the method of least squares, we have derived an expression for the deformation gradient at points in the continuous body that correspond to

positions of atoms in the discrete system. An inhomogeneity parameter has been introduced to characterize points where one or more components of the deformation gradients are unusually large, and indicate the initiation of dislocations.

We have used the publicly available MM software, LAMMPS, to study indentation of a gold crystal. For plane strain deformations, we have shown that the slope of the load versus indentation curve obtained from results of the MM simulations equals that of the curve derived from results of deformations at the continuum level.

Chapter 5

Contributions

Contributions of the work reported in this dissertation are summarized below.

We have derived an analytical solution for generalized plane strain indentation of a linear elastic anisotropic layer bonded to a rigid substrate and indented by a rigid cylindrical indenter. Values of geometric parameters for which the solution for the half space can be used to approximate that for the layer of finite thickness have been delineated.

By using Green's function for a linear elastic anisotropic half space and the pressure distribution on the contact surface of a cylinder indenting it, we have derived a closed-form relation between the axial load and the indentation depth. It has been demonstrated that one can determine values of three elastic constants of a cubic material by finding slopes of load versus indentation curves for three different orientations of a face centered cubic (FCC) material. Up to 6% deviations in the orientations of the FCC cubic crystal are shown to result in nearly 10% errors in the values of elastic constants determined by the proposed method. The technique can be easily generalized to materials of other symmetries.

In an attempt to study the equivalence between deformations of an atomic system and the equivalent continuum structure, we have reviewed the derivation of the Cauchy stress tensor in terms of interatomic forces and interatomic distances. Deformations during the indentation of a gold crystal by a rigid indenter have been analyzed by

using the software LAMMPS. From the axial load versus the depth of indentation curve and an expression for it derived from simulations at the continuum level, the elasticity parameter appearing in the slope of this curve has been found. Plane strain simple shearing and simple compressive deformations of a gold crystal have been simulated with LAMMPS. Results from the averaged stresses and strains agree with those from the analysis of the corresponding continuum problems, but the evaluations of local stresses and strains need further investigation.

References

Aboussaleh, M., Boukhili, R., 1998. The contact behavior between laminated composites and rigid impactors. Composite Structures 43, 165-178.

Angker, L., Swain, M. V., Kilpatrick, N., 2003. Micro-mechanical characterization of the properties of primary tooth dentine. Journal of Dentistry 31, 261-267.

Barnett, D. M., Lothe, J., 1975. Line force loadings on anisotropic half-spaces and wedges. Physica Norvegica 8, 13-22.

Batra, R. C., 2005. Elements of continuum mechanics. American Institute of Aeronautics and Astronautics, Inc. 115-143.

Bhattacharya, A. K., Nix, W. D, 1998a. Finite element simulation of indentation experiments. Int. J. Solids Struct. 24, 881-891.

Bhattacharya, A. K., Nix, W. D., 1998b. Analysis of elastic and plastic deformation associated with indentation testing of the thin films on substrates. Int. J. Solids Struct. 24, 1287-1298.

Bhushan, B., Israelachvili J. N., Landman, U., 1995. Nanotribology- friction, wear and lubrication at the atomic-scale. Nature 374, 607-616.

Briscoe, B. J., Sebastian, K. S., 1996. The elastoplastic response of poly(methyl methacrylate) to indentation. Proceedings of the Royal Society of London Series A-Mathematical Physical and Engineering Sciences 452, 439-457.

Briscoe, B. J., Sebastian, K. S., Sinha, S. K., 1996. Application of the compliance method to microhardness measurements of organic polymers. Philosophical Magazine A-Physics of Condensed Matter Structure Defects and Mechanical Properties 74 (5), 1159-1169.

Cheung, K. S., Yip, S., 1991. Atomic-level stress in an inhomogeneous system. J. Appl. Phys. 70, 5688-5690.

Clarke, D. R., Kroll, M. C., Kirchner, P. D., Cook, R. F., Hockey, B. J., 1988. Amorphization and Conductivity of Silicon and Germanium Induced by Indentation. Physical Review Letters 60, 2156-2159.

Clausius, R., 1870. On a mechanical theory applicable to heat. Philosophical Magazine 40, 122-127.

Doerner, M. F., Nix, W. D., 1986. A method for interpreting the data from depth-sensing indentation instruments. Journal of Material Research 1, 601.

Eshelby, J. D., Read, W. T., Schockley, W., 1953. Anisotropic elasticity with applications to dislocation theory. Acta Metallurgica 1, 251-259.

Fan, C. W., Hwu, C., 1996. Punch problems for anisotropic elastic half-plane. Journal of Applied Mechanics 63, 69–76.

Feichtinger D., Derlet P. M., Van Swygenhoven H., 2003. Atomistic simulations of spherical indentations in nanocrystalline gold. Physical Review B 67 (2), Art. No. 024113.

de la Fuente, O. R., Zimmerman, J. A., Gonzalez, M. A., de la Figuera, J., Hamilton, J. C., Pai, W. W., Rojo, J. M, 2002. Dislocation emission around nanoindentations on a (001) fcc metal surface studied by scanning tunneling microscopy and atomistic simulations. Physical Review Letters 88 (3), Article Number: 036101.

Gannepalli, A., Mallapragada S. K., 2001. Molecular dynamics studies of plastic deformation during silicon nanoindentation. Nanotechnology 12 (3), 250-257.

Gannepalli, A., Mallapragada, S. K., 2002. Atomistic studies of defect nucleation during nanoindentation of Au(001). Physical Review B 66 (10), Art. No. 104103.

Ghoniem, N. M., Busso, E. P., Kioussis, N., Huang, H. C., 2003. Multiscale modelling of nanomechanics and micromechanics: an overview. Philosophical Magazine 83 (31-34), 3475-3528.

Gladwell, G. M. L., 1980. Contact problems in the classical theory of elasticity. Alphen aan den Rjjn: Sijthoff and Noordhoff.

Green, A. E., Zerna, W., 1954. Theoretical Elasticity. Oxford University Press, Oxford.

Haider, M. A., Holmes, M. H., 1995. Indentation of a thin compressible elastic layer: Approximate analytic and numerical solutions for rigid flat indenters. Journal of the Mechanics and Physics of Solids 43, 1199-1219.

Habelitz, S., Marshall, S.J., Marshall, G.W., Jr., Balooch, M., 2001. Mechanical properties of human dental enamel on the nanometer scale. Archives of Oral Biology 46, 173-183.

Hardy, R. J., 1982. Formulas for determining local properties in molecular dynamics simulations: shock waves. Journal of Chemical Physics 76, 622-628.

Ho, S. P., Goodis, H., Balooch, M., Nonomura, G., Marshall, S.J., Marshall, G., 2004. The effect of sample preparation technique on determination of structure and nanomechanical properties of human cementum hard tissue. Biomaterials 25, 4847-4857.

Hoffler, C. E., Guo, X. E., Zysset, P. K., Goldstein, S. A., 2005. An application of nanoindentation technique to measure bonde tissue lamellae properties. Transactions of the ASME, 127, 1046-1053.

http://lammps.sandia.gov/index.html.

Huber, N., Tsakmakis, C., 2001. A neural network tool for identifying the material parameters of a finite deformation viscoplasticity model with static recovery. Computer Methods in Applied Mechanics and Engineering 191 (3-5), 353 -384.

Huber, N., Nix, W. D., Gao, H. 2002. Identification of elastic-plastic material parameters from pyramidal indentation of thin films. Proceedings of the Royal Society of London Series A-Mathematical, Physical and Engineering Sciences 458 (2023), 1593-1620.

Hwu, C., 1993. Fracture parameters for the orthotropic bimaterial interface cracks. Engineering Fracture Mechanics 45, No. 1, 89-97.

Hwu, C., Fan, C W., 1998. Sliding punches with or without friction along the surface of an anisotropic elastic half-plane. Quarterly Journal of Mechanics and Applied Mathematics 51, 159-177.

Irving, J. H., Kirkwood, J. G., 1950. The statistical mechanical theory of transport processes, IV. The equations of hydrodynamics. Journal of Chemical Physics 18, 817-829.

Johnson, K. L., 1985. Contact mechanics. Cambridge University Press, Cambridge, U.K..

Kallman, J. S., Hoover, W. G., Hoover, C. G., De Groot, A. J., Lee, S. M., Wooten, F., 1993. Molecular dynamics of silicon indentation. Physical Review B 47, 7705-7709.

Kelchner, C. L., Plimpton, S. J., Hamilton, J. C., 1998. Dislocation nucleation and defect structure during surface indentation. Physical Review B 58, No. 17, 11085-11088.

Landman, U., Luedtke, W. D., Burnham, N. A., Colton, R. J., 1990. Atomistic mechanisms and dynamics of adhesion, nanoindentation, and fracture. Science 248, 454-461.

Landman, U., Luedtke, W. D., Ringer, E. M., 1992. Atomistic mechanisms of adhesive contact formation and interfacial processes. Wear 153, 3-30.

Li, J., Van Vliet, K. J., Zhu, T., Yip, S., Suresh, S., 2002. Atomistic mechanisms governing elastic limit and incipient plasticity in crystals. Nature 418 (6895), 307-310.

Lilleodden, E. T., Zimmerman, S. M., Foiles, S. M., Nix, W. D., 2003. Atomistic simulations of elastic deformation and dislocation nucleation during nanoindentation. Journal of the Mechanics and Physics of Solids 51, 901-920.

Lin, Y., Ovaert, T. C., 2004. A rough surface contact model for general anisotropic materials. Journal of Tribology 126, 41-49.

Loubet, J. L., Georges, J. M., Marchesini, O, Meille, G., 1984. Vickers indentation curves of Magnesium-oxide (MGO). Journal of Tribology-Transactions of the ASME 106, 43-48.

Lovel, M., 1998. Analysis of contact between transversely isotropic coated surfaces: development of stress and displacement relationships using FEM. Wear 214, 165-174.

Lucas, B. N., Oliver, W. C., Ramamurthy, A. C., 1997. ANTEC Conference Proceedings 3, Society of Plastics Engineers, Brookfield, CT, 3445.

Lutsko, J. F., 1988. Stress and elastic constants in anisotropic solids: molecular dynamics techniques. Journal of Applied Physics 64, 1152-1154.

Marszalek, P. E., Greenleaf, W. J., Li, H. B., Oberhauser A. F., Fernandez, J. M., 2000. Atomic force microscopy captures quantized plastic deformation in gold nanowires. Proceedings of the National Academy Sciences USA 97(12), 6282-6286.

Meijers, P., 1968. The contact problem of a rigid cylinder on an elastic layer. Applied Science Resources 18, 353-383.

Minowa, K., Sumino, K., 1992. Stress-induced amorphization of a silicon crystal by mechanical scratching. Physical Review Letters 69, 320-322.

Murdoch, I. A., 2007. A critique of atomistic definitions of the stress tensor. Journal of Elasticity 88, 113-140.

Muskhelishvili, N. I., 1954. Some basic problems of the mathematical theory of elasticity, Noordhoff, Groningen, The Netherlands.

Ning, X., Lovell, M. R., Slaughter, W. S., 2003. Two-Dimensional anisotropic contact behavior of unidirectional continuous FRP Composites. Journal of Tribology 125, No. 2, 457-461.

Oliver, W. C., Pharr, G. M.,1992. An improved technique for determining hardness and elastic modulus using load and displacement during indentation experiments. Journal of Material Research 7, 1564-1583.

Park, H. S., Patrick, K. A., Wagner, G. J., 2006. A surface Cauchy-Born model for nanoscale materials. International Journal for Numerical Methods in Engineering 68, 1072-1095.

Pethica, J. B., Oliver, W. C., 1989. Mechanical properties of nanometer volumes of material: use of the elastic response of small area indentation. Materials Research Society Symposia Proceedings 130, 13-23.

Plimpton, S. J., 1995. Fast Parallel Algorithms for Short-Range Molecular Dynamics, Journal of Computational Physics 117, 1-19.

Plimpton, S. J., Pollock, R., Stevens, M., 1997. Particle-Mesh Ewald and rRESPA for Parallel Molecular Dynamics Simulations, in Proc of the Eighth SIAM Conference on Parallel Processing for Scientific Computing, Minneapolis, MN.

Raffi-Tabar, H., Pethica, J. B., Sutton, A. P., 1992. Influence of adsorbate monolayer on the nano-mechanics of tip-substrate interactions, Materials Research Society Symposia Proceedings 239, 313-318.

Sasaki, T., Yang, M., Fukushima, S., Tsukano, R., 2004. Development of the CAE-assisted nano-indentation method for the evaluation of the anisotropic mechanical-properties of thin films. Journal of Material Processing and Technology 151, 263-267.

Shen S., Atluri, S. N., 2004. Atomic-level stress calculation and continuum-molecular system equivalence. Computer Modeling in Engineering and Sciences 6, No.1, 91-104.

Smith, R., Christopher, D., Kenny, S. D., Richter, A., Wolf, B., 2003. Defect generation and pileup of atoms during nanoindentation of Fe single crystals. Physical Review B 67 (24), Art. No. 245405.

Sneddon, I. N., 1965. The relation between load and penetration in the axisymmetric Boussinesq problem for a punch of arbitrary profile. International Journal of Engineering Science 3, 47-57.

Srinivas, S., Rao, A. K., 1970. Bending, vibration and buckling of simply supported thick orthotropic rectangular plates and laminates. International Journal of Solids and Structures 6, 1463-1481.

Stroh, A. N., 1958, Dislocations and cracks in anisotropic elasticity, Philosophical Magazine 7, 625-646.

Stroh, A. N., 1962, Steady state problems in anisotropic elasticity, Journal of Mathematics and Physics 41, 77-103.

Sun, J., Tong, J., 2005. Application of Nanoindenter in Investigating Properties of the Cuticle of Dung Beetle. Proceedings of the 2005 IEEE: Engineering in Medicine and Biology 27th Annual International conference.

Swadener, J.G., Pharr, G.M., 2001. Indentation of elastically anisotropic half-spaces by cones and parabolae of revolution. Philosophical Magazine A 81, No. 2, 447-466.

Swanson, S.R., 2004. Hertzian contact of orthotropic materials. International Journal of Solids and Structures 41, 1945-1959.

Szlufarska, l., Kalia, R. K., Nakano, A., 2004. Nanoindentation-induced amorphization in silicon carbide. Applied Physics Letters 85, 378-380.

Tan, E. P. S., Goh, C. N., Sow, C. H., Lim, C. T., 2005. Tensile test of a single nanofiber using an atomic force microscope tip. Applied Physics Letters 86(7), Article Number: 073115.

Tan, T. M., Sun, C. T., 1985. Use of statical indentation laws in the impact analysis of laminated composite plates. Journal of Applied Mechanics 5, 6-12.

Ting, T. C. T., 1982. Effects of change of reference coordinates on the stress analyses of anisotropic elastic materials. International Journal of Solids and Structures 18, 139-152.

Ting, T. C. T., 1996. Anisotropic elasticity: Theory and applications. Oxford university press, 139.

Töyräs, T. L., Niinimäki, M., Lindgren, R., Nieminen, M. T., Kiviranta I., Jurvelin, J. S., 2001. Estimation of the Young's modulus of articular cartilage using an arthroscopic indentation instrument and ultrasonic measurement of tissue thickness. Journal of Biomechanics 34, 251–256.

Tsai, D. H. 1979 The virial theorem and stress calculation in molecular dynamics. Journal of Chemical Physics 70, 1375-1382.

Turner, J. R., 1966. Contact on a transversely isotropic half-space, or between two transversely isotropic bodies. International Journal of Solids and Structures 16, 409-419.

Van Vliet, K. J., Tsikata, S., Suresh, S., 2003. Model experiments for direct visualization of grain boundary deformation in nanocrystalline metals. Applied Physics Letters 83 (7), 1441-1443.

Vel, S. S., Batra, R. C., 2000. The generalized plane strain deformations of thick anisotropic composite laminated plates. International Journal of Solids and Structures 37, 715-733.

Vlassak, J. J., Nix, W. D., 1994. Measuring the elastic properties of anisotropic materials by means of indentation experiments, Journal of the Mechanics and Physics of Solids 42, 1223–1245.

Vlassak, J. J., Ciavarellab, M., Barberc, J. R., Wanga, X. 2003. The indentation modulus of elastically anisotropic materials for indenters of arbitrary shape. Journal of the Mechanics and Physics of Solids 51, 1701–1721.

Willis, J. R., 1966. Hertzian contact of anisotropic bodies. Journal of the Mechanics and Physics of Solids 14, 163-176.

Wong, E. W., Sheehan, P. E., Lieber, C. M., 1997. Nanobeam mechanics: Elasticity, strength, and toughness of nanorods and nanotubes. Science 277 (5334), 1971-1975.

Wu, E., Yen, C., 1994. The contact behavior between laminated composite plates and rigid spheres. Journal of Applied Mechanics 61, 60-66.

Yang, S. H., Sun, C. T., 1982. Indentation law for composite laminates. In: Daniel, I.M. (Ed.), Composite Materials: Testing and Design, 6th Conference. In: ASTM STP 787, 425–449.

Zhou, M., 2003. A new look at the atomic level virial stress: on continuum-molecular system equivalence. Proceedings of the Royal Society of London A 459, 2347-2392.

Zimmerman, J. A., Webb, E. B., Hoyt, J. J., Jones, R. E., Klein, P. A., Bammann, D. J., 2004. Calculation of stress in atomistic simulation. Modelling and Simulation in Materials Science and Engineering 12(4), S319-S332.